

# **Microwave Heating of Multiphase Materials: Modelling and Measurement**

Willem J. Louw

This thesis presented in partial fulfilment of the requirements for  
the degree of Master of Engineering at the University of  
Stellenbosch.

Supervisors: Prof. H.C. Reader and Prof. S.M. Bradshaw

December 2005

## **Declaration**

I, the undersigned, hereby declare that the work contained in this thesis is my own original work, unless stated otherwise, and that it has not previously in its entirety or in part been submitted at any university for a degree.

W.J. Louw:.....

Date:.....

## Abstract

Both coaxial probe and waveguide (*WG*) measurement systems for electric and magnetic material property extraction were investigated. These measurement techniques were used to determine electrical properties of an inhomogeneous rock sample in its solid and crushed states. A lumped element model of the probe was used and permittivity was determined by the inversion algorithm developed by Stuchly and Stuchly. To support this technique it was compared to a full wave inversion algorithm and referenced to properties of the same samples but determined by a resonant cavity technique. The Nicholson, Ross and Weir inversion algorithm was used to determine material properties from *WG* measurements. As a reference, the same techniques were applied to a well defined material. It was found that neither of the measurement techniques could measure low loss factors or conductive materials and literature values were used in these cases. Various simulation models of the multiphase ore in both its solid and crushed states are presented.

These models were utilised in finite-difference time-domain (*FDTD*) simulations of different microwave (*MW*) cavities. Simulation and experimental S-parameter comparisons are presented. The level of accuracy achieved varies as a function of the geometrical representation and material properties. After an S-parameter comparison with simulation results it was concluded that the electrical properties of both the solid and crushed rocks have been well determined for *MW* cavity design. Predicted and measured field distributions in cavities were also compared and it is shown that accurate models of multiphase materials become especially important in the determination of field distributions in and around different rock phases. Recommendations for the suggested material property determination and verification processes are presented. A specific application of this work is in the field of microwave assisted comminution.

## Opsomming

'n Koaksiale probe en golfgeleier (WG) stelsels vir die bepaling van materiaal eienskappe (elektries en magneties) word gebruik met die doel om 'n nie-homogene rotsmonster te karakteriseer. Die ekstraksie algoritme van Stuchly en Stuchly word gebruik om die materiaal eienskappe te bepaal vanaf die gemete  $S_{11}$ -parameter. Hierdie ekstraksie metode word vergelyk met 'n vol golf ekstraksie van permitiwiteit vanaf dieselfde gemete data. Beide die ekstraksie metodes word dan vergelyk met resonante holte meetings van dieselfde materiale. Die Nicholson, Ross en Weir ekstraksie algoritme word toegepas op meetings wat gedoen is deur die golfgeleier stelsel. As 'n verwysing word dieselfde tegnieke toegepas op 'n bekende materiaal en daar is gevind dit stem goed ooreen behalwe dat nie een van die twee meet tegnieke lae verlies faktore kan meet nie. Verder kan nie een van die twee sisteme geleidende materiale meet nie. Vir sulke gevalle is waardes nageslaan. Verskeie simulasiemodelle van die rots word voorgestel vir beide soliede en vergruisde monsters.

Hierdie modelle word gebruik in *FDTD* simulasies van verskeie mikrogolftoevoegers met die oog om 'n vergelyking te tref tussen gesimuleerde en gemete S-parameters. Verskillende vlakke van akkuraatheid is bereik en is 'n funksie van die geometrie en die materiaaleienskappe van die model. Nadat gemete en gesimuleerde S-parameters vergelyk is, is gevind dat die materiaal eienskappe van beide die soliede en vergruisde rots monsters goed bepaal is vir mikrogolf toevoeger ontwerp. Voorspelde en gemete veldverspreidings word ook vergelyk en dit is veral hierso van belang om 'n realistiese model van die nie-homogene monster te gebruik. Sekere voorstelle word gemaak om die verskillende aspekte van die meet van materiaaleienskappe en simulasiemodelle te kan verfyn. 'n Spesifieke toepassing van hierdie werk is in mikrogolf ondersteunde skeiding van minerale en erts.

## Acknowledgements

During the course of this work many people's help and support were received in abundance and this thesis will not be complete without the following acknowledgements

Prof. Howard Reader: Thank you for your guidance, advice, moral support, enthusiasm and patience shown towards me. Your application of knowledge is inspirational.

Prof. Steven Bradshaw who is the driving force behind the University of Stellenbosch's involvement in the AMIRA project. Thank you for allowing me to do this thesis in conjunction with my work. Your patience and the financial support are much appreciated. Thank you for your academic support, advice and guidance which are always done in a very humble manner.

Wessel Croukamp and Ulrich Buttner from SED who were always willing to help. Even with the mundane tasks.

Grant Scott for polishing of mineral samples.

The SMD workshop for the careful way in which they have constructed waveguide components and the tunnel applicator.

Martin Siebers who helped with probe and WG measurements.

Rodney Urban for proof reading of the abstract and general suggestions.

Carien Fouché for the use of her computer in order to do resource intensive simulations.

Nottingham University and Dr. Sam Kingman for providing mineral samples and financial support.

Michael Janezic from NIST for providing various material samples and processing of data to enable comparison of their full wave inversion technique with the inversion algorithm presented in this thesis.

Marie-Louisé Louw: Thank you for proof reading parts of this thesis and for your moral support.

Vivien Marsden: Thank you for bringing out the best in me. Also thank you for your patience and valuable ideas regarding the thesis.

Aan Ma en Pa: Baie dankie vir julle belangstelling en ondersteuning reg deur my akademiese loopbaan. Dankie vir al jul opofferings wat dit vir my moontlik gemaak het om geleenthede soos hierdie en vele ander te bekom.

Finally I want to thank and praise my Lord Jesus Christ for the ability and the opportunity to do this work.

## List of Abbreviations

<i>ANA</i>	Automatic Network Analyser
<i>AVNA</i>	Automatic Vector Network Analyser
<i>CEM</i>	Computational Electromagnetics
<i>E-Field</i>	Electric-Field
<i>EM</i>	Electromagnetic
<i>FDTD</i>	Finite-Difference Time-Domain
<i>FEM</i>	Finite Element Method
<i>HP</i>	Hewlett Packard
<i>I/O</i>	Input/Output
<i>MoM</i>	Method of Moments
<i>MUT</i>	Material Under Test
<i>MW</i>	Microwave
<i>NIST</i>	National Institute of Standards and Technology
<i>NRW</i>	Nicholson Ross Weir
<i>NU</i>	Nottingham University
<i>RF</i>	Radio Frequency
<i>SH</i>	Sample Holder
<i>SMA</i>	Standard Military Adapter
<i>SN</i>	Signal to Noise Ratio
<i>S-Parameter</i>	Scattering Parameter
<i>TE</i>	Transverse Electric
<i>TEM</i>	Transverse Electromagnetic
<i>TM</i>	Transverse Magnetic
<i>US</i>	University of Stellenbosch
<i>WG</i>	Waveguide

Please note that some figures in this thesis show their titles written with subscripts. This is a result of an underscore appearing in the Matlab<sup>®</sup> processed filename (i.e. material\_properties will read material<sub>p</sub>roperties).

## Table of Contents

Declaration .....	i
Abstract .....	ii
Opsomming .....	iii
Acknowledgements .....	iv
List of Abbreviations .....	vi
Table of Contents .....	vii
List of Figures .....	<a href="#">xii</a>
List of Tables .....	xv
 Chapter 1 .....	 1
Introduction .....	1
1.1 Microwave Heating Review .....	1
1.2 Thesis Overview .....	2
 Chapter 2 .....	 4
Material Properties .....	4
2.1 Introduction .....	4
2.2 Complex Permittivity .....	4
2.3 Complex Permeability .....	6
2.4 Ohmic and Dielectric Conductivity .....	7
2.5 Conclusion .....	9
 Chapter 3 .....	 10
Measurement Systems .....	10
3.1 Introduction .....	10
3.2 Material Properties Measurement Systems .....	10
3.3 Coaxial Probe Measurement System .....	12
3.3.1 Lumped Element Model of the Flanged Coaxial Probe .....	14
3.3.1.1 Probe Calibration and $C_f$ .....	15
3.3.2 Analytical Solution for Permittivity .....	16
3.3.3 Simplified Circuit vs. Full Wave Inversion .....	17
3.3.4 Measurement Error .....	20
3.3.5 Remarks on the Flanged Coaxial Probe Measurement System .....	20
3.4 Waveguide Measurement System .....	21
3.4.1 WG Theory: An Overview .....	21
3.4.2 Measurement Setup .....	23
3.4.3 WG Matched Load Calibration Standard .....	24
3.4.3.1 WG Sliding Load Offset Error .....	27
3.4.4 Materials in WG: S-Parameter Point of View .....	29



3.4.5 Inversion algorithm.....	30
3.4.6 WG Measurement and Higher Order Modes .....	33
3.4.7 Remarks on the Waveguide Measurement System .....	33
3.5 Conclusion .....	34
 Chapter 4.....	 35
Material Property Measurement .....	35
4.1 Introduction.....	35
4.2 ANA Setup for Material Properties .....	36
4.3 Materials of Interest and Sample Preparation .....	37
4.3.1 Homogeneous Materials .....	37
4.3.2 Copper Carbonatite Ore .....	37
4.3.3 Sample Preparation.....	39
4.4 Summary of Proposed Measurements .....	40
4.5 Measurement of Homogeneous Materials .....	41
4.5.1 Coaxial Probe Measurements.....	41
4.5.2 WG Measurements .....	45
4.6 Measurement of Inhomogeneous Materials.....	51
4.7 Summary of Results.....	57
4.8 Conclusion .....	57
 Chapter 5.....	 60
Verification of Material Properties by FDTD Simulation.....	60
5.1 Introduction.....	60
5.2 S-Parameter Comparison .....	61
5.3 Simulation Models .....	61
5.4 Introduction to Computational Electromagnetics (CEM) .....	63
5.4.1 FDTD Concerto <sup>®</sup> from Vector Fields <sup>®</sup> .....	64
5.4.1.1 Define Material Properties .....	65
5.4.1.2 Creating the Simulation Model.....	67
5.4.1.3 Defining the Mesh .....	67
5.4.1.4 Port Definition .....	68
5.4.1.5 Post-Processing Data, Run Simulation and View Results .....	69
5.5 Comparison of WG SH Measurement and Simulation .....	70
5.5.1 Carbon Foam: Homogeneous Sample vs. Homogeneous Model .....	73
5.5.2 Carbonatite Ore .....	75
(I) Two Phase Solid Sample vs. Homogeneous Model .....	75
(II) Two Phase Solid Sample vs. Two Phase Model.....	77
5.5.3 Crushed Carbonatite Ore.....	79
(I) Three Phase Sample vs. Homogeneous Model .....	79
(II) Three Phase Sample vs. Two Phase Model.....	81
(II.I) Clustered Simple Geometry .....	81

(II.II) Rock Particles Spread and Rotated Alternately .....	83
(III) Three Phase Sample vs. Three Phase Geometry .....	85
5.6 Comparison of Single Mode (SM) Cavity Measurement and Simulation....	88
5.6.1 Description of Single Mode Cavity Experiment .....	88
5.6.2 Two Phase Load vs. Homogeneous Model .....	91
5.6.3 Three Phase Load vs. Homogeneous Model .....	93
5.6.3.1 Sensitivity Analysis of Material Properties.....	94
5.6.4 Three Phase Load vs. Two Phase Model .....	95
5.6.4.1 Less Dense Load Model .....	97
5.6.5 Three Phase Load vs. Three Phase Model.....	98
5.6.5.1 Simple Load Model .....	99
5.6.5.2 More Realistic Load Model.....	100
5.6.5.3 Sensitivity Analysis of $s_c$ .....	102
5.7 Conclusion .....	103
Chapter 6.....	104
Cavity Probing and Simulation Field Plots: An Application of Material Properties	
.....	104
6.1 Introduction.....	104
6.2 Experimental Determination of E-Field Distribution.....	104
6.2.1 Field-Probing of a Cylindrical MW Cavity .....	105
6.3 Simulation Models .....	109
6.4 Field Plots: Experimental vs. Simulation.....	110
6.4.1 Carbonatite at Top of Cavity .....	110
6.5 Field Probing Applied to an Industrial Cavity .....	113
6.6 Conclusion .....	117
Chapter 7 .....	119
Conclusion and Recommendations .....	119
7.1 Conclusion .....	119
7.2 Recommendations .....	120
Bibliography:.....	123
Appendix A .....	127
Material Properties and Measured S-Parameters.....	127
A.1 Coaxial Probe Measurements .....	127
A.2 WG Measurements and S-Parameters.....	132
Appendix B.....	137
Field Probing .....	137

Appendix C.....	139
Dimensions of Tunnel Applicator .....	139
Appendix D .....	140
Matlab <sup>®</sup> Routines.....	140

## List of Figures

Figure 1.1 - Overview and application of thesis .....	2
Figure 2.1 - Macroscopic and microscopic model of conductivity, (After Cloete [14]) .....	7
Figure 3.1 - Different combinations of dielectric constant and loss factor values .	11
Figure 3.3 – Flanged Coaxial-probe with calibration standards, (after Rimbi [10]) .....	14
Figure 3.4 - Flanged coaxial probe and equivalent lumped element representation .....	14
Figure 3.5 - Full wave and simplified circuit inversion techniques comparison for Rexolite .....	18
Figure 3.6 - Full wave and simplified circuit inversion techniques comparison for Fused Silica .....	18
Figure 3.7 - Geometry of rectangular waveguide, (after Pozar [12]) .....	21
Figure 3.8 - Magnitude of Electric and Magnetic field distribution of $TE_{10}$ mode in rectangular WG, (after Pozar [12]) .....	22
Figure 3.9 - Physical representation of WG measurement setup; Transverse Section.....	23
Figure 3.10 - Five different reflection coefficients for five different positions of the sliding load .....	25
Figure 3.11 - WG sliding load standard.....	25
Figure 3.12 - Schematic of the positioning of the sliding load. Positions 1 to 5 moves the error vector from 0 to 270 degrees on the Smith chart .....	26
Figure 3.13 - The residual energy not dissipated by the load and not reflected distorts the circle around the origin.....	27
Figure 3.14 - Typical measured $S_{11}$ data of a MUT after calibration .....	28
Figure 3.15 - $S_{11}$ and $S_{22}$ parameters for both an isotropic and anisotropic material respectively.....	30
Figure 4.1 - Rectangular slab of carbonatite used by the waveguide measurement system.....	38
Figure 4.2 - Rectangular slabs of calcite and magnetite used in the probe and WG measurements.....	39
Figure 4.3 - Crushed carbonatite rocks used during measurements made by the waveguide system.....	40
Figure 4.4 - Dielectric constant and loss factor of PTFE as measured with the coaxial probe .....	42
Figure 4.5 - Dielectric constant and loss factor of calcite as measured with the coaxial probe .....	44

Figure 4.6 - Dielectric and magnetic properties of PTFE as measured with the WG system.....	46
Figure 4.7 - Magnitude and phase of the transmission coefficient .....	47
Figure 4.8 - Reflection Coefficient of PTFE vs. frequency .....	48
Figure 4.9 - Dielectric and magnetic properties of calcite as measured with the WG system .....	49
Figure 4.10 - $S_{11}$ of calcite.....	50
Figure 4.11 - Dielectric and magnetic properties of carbonatite as measured with the WG system.....	52
Figure 4.12 - $S_{11}$ of the carbonatite sample .....	53
Figure 4.13 - Artificial diamagnetic material, (after Haus and Melcher [36]) .....	54
Figure 4.14 - Dielectric and magnetic properties of crushed ore as measured with the WG system.....	55
Figure 4.15 - $S_{11}$ -Parameter of rocks packed inside SH2 .....	56
Figure 5.1 – Diagrammatic representation of the experimental/simulation comparison technique .....	60
Figure 5.2 - “Black box” approach and flow of waves in a general 2 port system .....	61
Figure 5.4 - Seven steps when setting up a simulation in Concerto® .....	65
Figure 5.5 - The definition of materials dialog in the Concerto® environment .....	66
Figure 5.6 - A special plane in Concerto (black line) forces different cell sizes above and below itself .....	68
Figure 5.7 - I/O Ports parameter dialogue box in Concerto® .....	69
Figure 5.8 - WG simulation model with reference planes at both sides of the sample .....	70
Figure 5.9 - $S_{11}$ and $S_{21}$ comparison of carbon foam using the WG system .....	74
Figure 5.10 - Homogeneous $S_{11}$ and $S_{21}$ comparison between measurement and simulation of carbonatite .....	76
Figure 5.11 - Two phase model of carbonatite reconstructed in Concerto .....	77
Figure 5.12 - Two-phase $S_{11}$ and $S_{21}$ comparison between measurement and simulation of carbonatite .....	78
Figure 5.13 - $S_{11}$ and $S_{21}$ boundary comparison between measurement and simulation of crushed ore .....	80
Figure 5.14 - 3D view of an unlikely rock distribution in the WG SH .....	82
Figure 5.15 - $S_{11}$ and $S_{21}$ comparison between measurement and simulation of crushed ore.....	82
Figure 5.16 - 3D view of a more representative model of the physical load of crushed rocks .....	83
Figure 5.17 - $S_{11}$ and $S_{21}$ boundary comparison between measurement and simulation of crushed ore .....	84
Figure 5.18 - Three phase model of the crushed ore inside the WG SH .....	86
Figure 5.19 - $S_{11}$ and $S_{21}$ comparison between measurement and simulation of crushed ore.....	87

Figure 5.20 - Transverse and plan view of the NU single mode cavity; dimensions in mm .....	89
Figure 5.21 - Load of crushed ore (approximated as a 3 phase load) .....	90
Figure 5.22 - Isometric view of homogeneous load inside the single mode cavity .....	91
Figure 5.23 - $S_{11}$ Magnitude comparison of a solid carbonatite cylinder .....	92
Figure 5.24 - Experimental upper and lower bounds compared to the homogeneous simulation model .....	94
Figure 5.25 - $S_{11}$ Magnitude comparisons with changed material properties .....	95
Figure 5.26 - Isometric and plan view of 2 phase simulation model of the load ..	96
Figure 5.27 - $S_{11}$ Magnitude of 2 phase load compared to measured bounds .....	97
Figure 5.28 - $S_{11}$ Magnitude comparison of a less dense 2 phase model .....	98
Figure 5.29 - Transverse and plan view of an unrealistic three phase model .....	99
Figure 5.30 - $S_{11}$ Magnitude comparison of an unrealistic load model with experimental bounds .....	100
Figure 5.31 - Isometric and Plan View of 3 phase simulation model for rock and air mixture .....	101
Figure 5.32 - $S_{11}$ Magnitude comparison of complex 3 phase model and experimental bounds .....	101
Figure 5.33 - $S_{11}$ Magnitude comparisons for different values of conductivity ..	102
 Figure 6.1 - General setup for field probing .....	 105
Figure 6.2 - Measurement setup for cylindrical cavity probing .....	106
Figure 6.3 - Cylindrical cavity and probe .....	107
Figure 6.4 - Ideal setup for field-probing .....	108
Figure 6.5 - Simulation model of carbonatite slab at the top of the cylindrical cavity .....	109
Figure 6.10 – Simulation model of mineral processing applicator .....	114
Figure 6.12 – Measurement setup for field probing of tunnel applicator .....	115
Figure 6.11 – Experimental and simulation $S_{11}$ comparison of loaded tunnel applicator .....	115
Figure 6.13 – Experiment and simulation comparative $E_x$ -field distributions; step end of applicator .....	116
Figure 6.14 – Loaded and empty cavity $E_x$ -field distribution at the face of the tunnel; step end of applicator .....	117
 Figure A.1 - Dielectric constant and loss factor of Air as measured with the coaxial probe .....	 127
Figure A.2 - Dielectric constant and loss factor of Perspex as measured with the coaxial probe .....	128
Figure A.3 - Dielectric constant and loss factor of carbon foam as measured with the coaxial probe .....	129
Figure A.4 - Dielectric constant and loss factor of magnetite as measured with the coaxial probe .....	130

Figure A.5 – A probe measurement of a material with a high quality phase stable cable .....	131
Figure A.6 - Dielectric and magnetic properties of Air as measured with the WG system.....	132
Figure A.7 - Dielectric and magnetic properties of Perspex as measured with the WG system .....	133
Figure A.8 - Transmission coefficient of Perspex as measured with the WG system .....	133
Figure A.9 - Dielectric and magnetic properties of carbon foam as measured with the WG system.....	134
Figure A.10 - Dielectric and magnetic properties of magnetite as measured with the WG system.....	135
Figure B.1 - Experimental and simulation resonant frequencies of empty cavity	137
Figure B.2 - Experimental and simulation $TM_{010}$ field distribution .....	138
Figure C.1 – Dimensions of the tunnel applicator in mm .....	139

## List of Tables

Table 3.1 – Comparison of inversion techniques for rexolite with a resonant cavity system.....	18
Table 3.2 – Comparison of inversion techniques for fused silica with a resonant cavity system.....	19
Table 4.1 - Permittivity and permeability values of PTFE and Perspex as quoted in literature [20], [4] .....	37
Table 4.2 - Summary of materials measured using both measurement techniques	40
Table 4.3 - Comparison of material properties measured with the probe, WG and literature.....	57
Table 5.1 - Table showing the different materials' simulation models and their properties .....	72
Table 5.2 - Quantitative results comparison; Carbon Foam-Homogeneous Model .....	75
Table 5.3 - Quantitative results comparison; Carbonatite-Homogeneous Model ..	76
Table 5.4 - Quantitative results comparison; Carbonatite-2 Phase model .....	79
Table 5.5 - Quantitative results comparison; Crushed Ore-Homogeneous model.	81
Table 5.6 - Quantitative results comparison; Crushed Ore-Simple 2 Phase model	83
Table 5.7 - Quantitative results comparison; Crushed Ore-Improved 2 Phase model .....	85
Table 5.8 - Quantitative results comparison; Crushed Ore-3 Phase model .....	87
Table 5.9 - Table showing the material properties of Styrofoam and Pyrex <sup>®</sup> , (after von Hippel [20]) .....	90
Table A.1 – Extracted material properties of three different experiments for crushed ore .....	136



# Chapter 1

## Introduction

---

### ***1.1 Microwave Heating Review***

Microwave (*MW*) heating is still a relatively novel technology, discovered (supposedly by accident) in 1945 whilst developing radar systems. Osepchuk [1] gives a thorough account of microwave heating history and it will not be repeated here.

In general, the advantages of microwave heating are numerous and include rapid energy transfer, volumetric and selective heating, uniformity of heating, faster through-puts, superior moisture levelling compared with conventional heating, fast switch on and off, cleaner environments (free from products of combustion), compact equipment, very high power densities developed in the processed zone, low maintenance and service costs and energy absorption enhancement by catalysts [2].

The various advantages appeal to different areas in the industry. Commercially, microwave heating finds its main application in microwave ovens, i.e. heating and cooking of food. Industrial microwave heating applications are highlighted by Metaxas [3] and are pasteurisation and sterilisation, heating and cooking, food tempering, pre-heating for rubber vulcanisation and drying. A thorough investigation into all the different aspects of microwave heating was conducted by Metaxas and Meredith [4]. Other applicable sources include Meredith [5], Puschner [6] and Chan and Reader [7].

In the past few years, microwave mineral processing, or microwave assisted comminution, has received an increasing amount of attention. Kingman et al. [8] recorded a 30% reduction in comminution energy after microwave treatment of the mineral ore. Other advantages may include reduced plant size, reduced wear costs per tonne, less

water consumption and liberation at higher sizes. Central to mineral microwave processing is simulation and determination of material properties.

## 1.2 Thesis Overview

The aim of this thesis is to determine material properties of a mineral ore by measurement and finite-difference time-domain (*FDTD*) simulation comparison, in both its solid and crushed states with the view on *MW* cavity design. The techniques described in this thesis can be applied to any multiphase material. Figure 1.1 gives a graphical representation of the work done in this thesis and the application thereof.

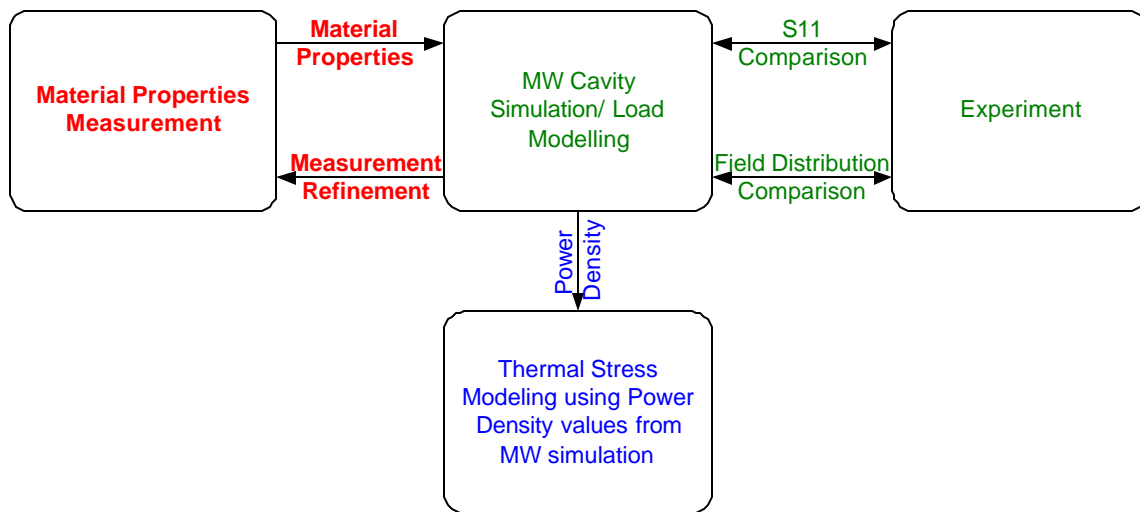


**Figure 1.1 - Overview and application of thesis**

This thesis forms part of a project in conjunction with Nottingham University (*NU*). Thermal stress modelling, which is done at *NU*, uses power density values obtained from *FDTD* simulations and helps in predicting stress fractures between different mineral phases. This knowledge can then be used as a design parameter for *MW* cavities.

Chapter 2 introduces material properties relevant to the thesis. Chapter 3 describes two material property measurement systems. These are the coaxial probe and waveguide (*WG*) measurement systems. Subtleties regarding probe calibration and the internal probe

fringing capacitance are addressed. The inversion algorithm developed by Stuchly and Stuchly [9] was implemented to determine material properties from probe measurements. A comparison is made to a full wave inversion technique. The *WG* matched load calibration standard and inversion technique are also investigated.

Material properties of a copper ore are determined in Chapter 4. This was done in both its solid and crushed states. In attempting this, the two dominant phases of the ore are investigated individually. Higher order mode excitation and the sensitivity of the *WG* measurement system are also discussed.

The *FDTD* simulation software used is overviewed in Chapter 5. Simulations of both the *WG* measurements for material properties and a single mode applicator are compared to measured S-parameters. This served as a ‘*black box*’ comparison between simulation model and measured cavities. Together with material properties, the geometrical representation of the model is investigated.

Cavity field probing is presented in Chapter 6 to illustrate the importance of accurate modelling of multiphase loads for the determination of electromagnetic power density in and between different phases.

Finally, in Chapter 7 main conclusions are drawn. Also, after a critical evaluation of the work done, recommendations are made for future research.

# Chapter 2

## Material Properties

---

### 2.1 Introduction

The material properties important in electromagnetic (*EM*) simulation and cavity design are permittivity (commonly known as the dielectric property), permeability and conductivity. Conventions and notations of each of these properties are discussed and introduced in this Chapter.

Sections 2.2, 2.3 and 2.4 discuss permittivity, permeability and conductive properties respectively. The Chapter ends with a conclusion on the principal findings in Section 2.5.

### 2.2 Complex Permittivity

Complex permittivity and permittivity have been defined in various ways in the literature. Rimbi [10] gave a good account of the various definitions and exposed possible points of confusion in a comprehensive but expedient manner. A similar approach will be followed here.

Zhang et al. [11] defined the complex permittivity ( $\epsilon^*$ ) as:

$$\epsilon^* = \epsilon' - j \left( \epsilon'' + \frac{\sigma}{\omega \epsilon_0} \right) \quad (2.1)$$

Where  $\epsilon'$  is known as the dielectric constant and is a measure of the material's ability to store electric energy (e.g. parallel plate capacitor with dielectric slab between plates). The complex term is known as the effective dielectric loss factor and is a measure of the material's ability to transform microwaves into heat. The symbols are as follows:

$\epsilon''$  is the loss factor

$\sigma$  is the electrical conductivity in  $S/m$

$\omega$  is the angular frequency in *radians/s*

$\epsilon_0$  is the permittivity in free space, which is a universal constant ( $8.854 \times 10^{-12} \text{ Fm}^{-1}$ )

When working with dielectric materials, the electrical conductivity approaches zero and the permittivity ( $\epsilon$ ) is often defined as:

$$\epsilon_{\sigma=0}^* = \epsilon = \epsilon' - j\epsilon'' \quad (2.2)$$

Based on this assumption the terms complex permittivity and permittivity are used interchangeably in dielectric literature.

The permittivity is frequently expressed in terms of a relative permittivity ( $\epsilon_r$ ), which is defined as:

$$\epsilon_r = \frac{\epsilon}{\epsilon_0} \quad (2.3)$$

Taking (2.3) into account (2.2) can be written as:

$$\epsilon_r = \epsilon_r' - j\epsilon_r'' \quad (2.4)$$

In this thesis (2.2) will be used throughout and the terms “dielectric constant” will be used to describe  $\epsilon'$  and “loss factor” to describe  $\epsilon''$ .

The ratio of the loss factor to the dielectric constant:

$$\tan(\delta) = \frac{\epsilon''}{\epsilon'} \quad (2.5)$$

is known as the loss tangent and will also be used in this thesis.

Dielectric losses are primarily a result of various polarisation phenomena and for a comprehensive account thereof refer to [4]. However, it is worth noting here that dipolar or reorientation polarisation is the most significant dielectric loss mechanism at microwave frequencies [4] and is described by the famous Debye equations [15]. Complex permittivity is usually a function of frequency, and also of temperature. A thorough investigation has been conducted of these factors by Metaxas and Meredith [4].

## 2.3 Complex Permeability

To account for magnetic losses in a medium the permeability also attains a complex form [12] and can be written as:

$$\mathbf{m} = \mathbf{m}' - j\mathbf{m}'' \quad (2.6)$$

Again, the permeability is frequently expressed in terms of a relative permeability ( $\mu_r$ ), and is defined as:

$$\mathbf{m}_r = \frac{\mathbf{m}}{\mathbf{m}_0} \quad (2.7)$$

$\mathbf{m}_0$  is a universal constant for the permeability of free space and is equal to  $4\pi \times 10^{-7} \text{ Hm}^{-1}$

Taking (2.7) into account (2.6) can be written as:

$$\mathbf{m}_r = \mathbf{m}'_r - j\mathbf{m}''_r \quad (2.8)$$

The real part  $\mathbf{m}'_r$  is a measure of the material's ability to store magnetic energy. The imaginary part  $\mathbf{m}''_r$  is the magnetic loss factor and describes the magnetic power

absorption ability of the material. The magnetic loss factor is due to relaxation and resonance processes under the influence of an alternating magnetic field [4].

In this thesis the notation of (2.6) will be used throughout and the terms “real part of permeability” will be used to describe  $\mathbf{m}'$  and “magnetic loss factor” will be used to describe  $\mathbf{m}''$ .

## 2.4 Ohmic and Dielectric Conductivity

Ohmic conductivity is a quantitative measure of how easily electric current (flow of charged particles) can be established in a material. Braithwaite and Weaver [13] follow both a *macroscopic* and a *microscopic* approach to quantify ohmic conductivity. The approach is represented in Figure 2.1. The geometrical setup consists of a d.c. voltage source  $V$ , connected to a metal rod of finite resistance  $R$ , length  $l$  and cross sectional area  $A$ . The connecting wires between the voltage source and the rod are assumed to be superconductors at room temperature (i.e. zero resistance).

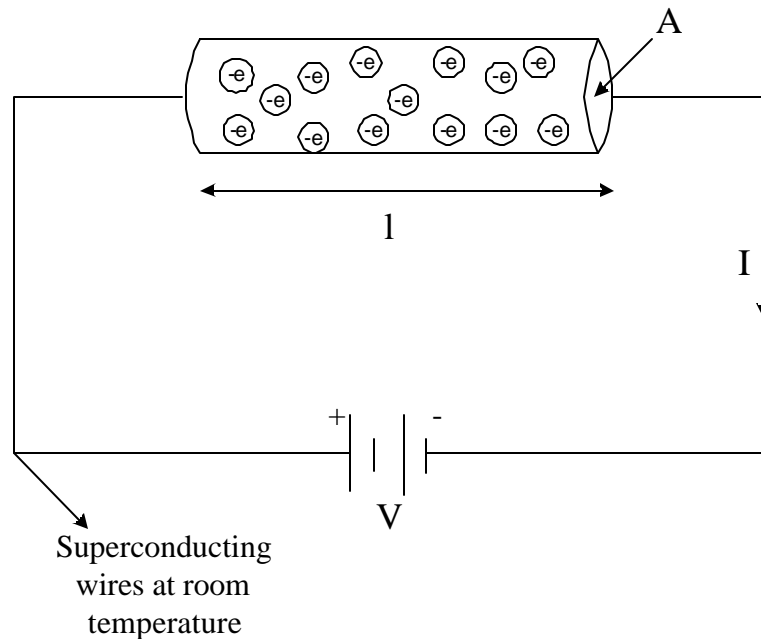


Figure 2.1 - Macroscopic and microscopic model of conductivity, (After Cloete [14])

From Ohm's law the current ( $I$ ) that will flow in the circuit is:

$$I = \frac{V}{R} \quad (2.9)$$

The resistance of the rod is a combination of its geometry and its conductivity and can be defined as:

$$R = \frac{l}{sA} \quad (2.10)$$

Where the dimensions are as indicated in Figure 2.1 and  $s$  is the conductivity in  $S/m$ . If the current in the system can be measured we can calculate the conductivity of the rod as:

$$s = \frac{Il}{VA} \quad (2.11)$$

It should be noted that if the d.c source in Figure 2.1, is replaced by an a.c. source, skin depth should be taken in account. This will decrease the effective cross-sectional area through which current flows and thus increase resistance (2.10). It is therefore important to notice that ohmic conductivity ( $s$ ) is a property of a material and is independent of frequency.

Braithwaite and Weaver [13] define ohmic conductivity on a microscopic level as:

$$s = nqu \quad (2.12)$$

$s$  is the ohmic conductivity in  $S/m$

$n$  is the number of free charges in  $m^3$

$q$  is the charge of the particle in coulomb,  $C$

$u$  is the mobility of the charged particles in  $m/s$



According to Pozar [12] and von Hippel [15] dielectric conductivity is defined as:

$$\mathbf{S} = \mathbf{we}^{\prime \prime} \quad (2.13)$$

From (2.12) and (2.13) it is clear that the physics of ohmic and dielectric conductivity is different. Ohmic conductivity is a function of the number of charged particles and their ability to move under a force (potential difference). Dielectric conductivity is a function of frequency and the dielectric loss factor. Recall from Section 2.2 that dielectric loss is the result of various polarisation phenomena and is also a function of frequency. To differentiate between ohmic and dielectric conductivity the notation throughout the rest of the thesis will be  $\mathbf{S}_e$  and  $\mathbf{S}_d$  respectively.

## 2.5 Conclusion

This chapter introduced the material properties important in electromagnetic simulation and cavity design ( $\epsilon$ ,  $\mu$ ,  $s_d$ ,  $s_e$ ). The notations that are used throughout this thesis were chosen. The physics supporting the respective material properties was mentioned but not discussed in detail. Reference was made to the relevant sources for further detail on materials physics. The principal sources were Rimbi [10], Pozar [12], Metaxas and Meredith [4] and Braithwaite and Weaver [13].

# Chapter 3

## Measurement Systems

---

### **3.1 Introduction**

Chapter 2 introduced the material properties important in electromagnetic simulation and cavity design. Many industrial processes utilise microwave (*MW*) heating techniques on materials that are dominated by permittivity [3]. A wealth of literature is available on dielectric property measurements e.g. Stuchly and Stuchly [9], Weir [16], Athey et al. [17], Jiang et al. [18], Arai et al. [19], von Hippel [15], [20] and Metaxas and Meredith [4].

However, to characterise a multiphase mineral ore sample electromagnetically, dielectric properties alone are not sufficient. Mineral ore is bound to have some metal component and the need arises to characterise magnetic (permeability) and conductive properties.

This Chapter will review various material properties measurement systems in use today (Section 3.2) and will then move on to focus on the coaxial probe (Section 3.3) and waveguide (Section 3.4) measurement systems. Conclusions and principal findings are presented in Section 3.5.

Throughout, a certain familiarity with the Automatic Vector Network Analyser (*AVNA* or just *ANA*) is assumed [21], [22].

### **3.2 Material Properties Measurement Systems**

At microwave frequencies the two basic material properties measurement techniques are resonant techniques and reflection-transmission techniques [23]. At radio frequencies (*RF*, up to *100 MHz* according to [5]) capacitive techniques are also employed. Both of

the microwave frequency techniques comprise various measurement systems. Resonant techniques can vary from open cavity resonators to parallel plate resonators [23]. These can measure either permittivity or permeability but not both simultaneously [23] and only at a single frequency. Some reflection-transmission techniques widely used are coaxial line, waveguide, stripline and free space measurement systems. Each of the four reflection-transmission systems stated here has been studied at the University of Stellenbosch (*US*) [10], [24], [25]. Reflection-transmission systems have the advantage of measuring both permittivity and permeability simultaneously over a wide frequency range.

Before proceeding to the measurement systems used in this work a review of parameter ranges and measurement systems is in order. This will be in terms of permittivity values, but is also applicable to permeability measurements.

Figure 3.1 presents nine possible combinations of dielectric constant and loss factor. The terms low, middle and high are not defined quantitatively and will be used loosely here.

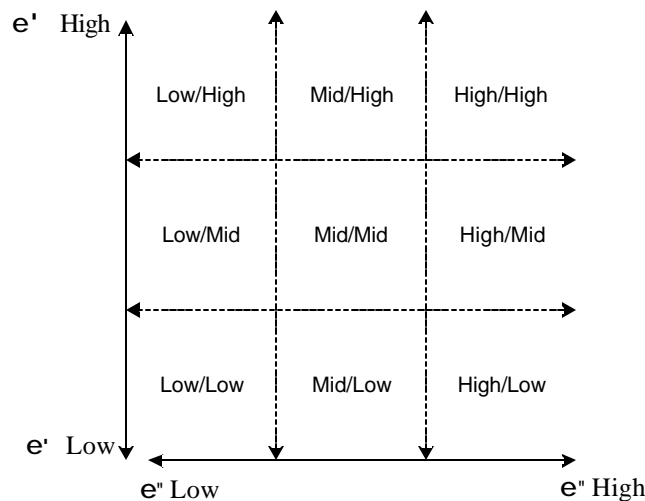


**Figure 3.1 - Different combinations of dielectric constant and loss factor values**

It is known that resonant techniques are especially accurate and can measure a low to high dielectric constant and low to medium loss factors [4], [22]. A disadvantage, as stated already, is that they are single frequency measurements. The reflection-transmission measurements can measure low to high dielectric constants and medium to high loss [22]. They have the advantage, as stated already, of being wideband measurement techniques.

The two techniques used in this work are both reflection-transmission techniques and are the one port open ended coaxial probe system (determines only permittivity) and the two port waveguide system (determines permittivity and permeability).

### ***3.3 Coaxial Probe Measurement System***

Marcuvitz [26] analysed a coaxial line terminated by a capacitive gap. Westphal [27] suggested using this capacitive gap termination to measure the permittivity of a sample material using the configuration in Figure 3.2(a). The two most common techniques by which the system in Figure 3.2(a), looking into section A-A, can be solved are full wave analysis [28] and an equivalent lumped element model. Stuchly and Stuchly [9] suggested an equivalent lumped element representation (Figure 3.2(b)) to determine the permittivity.

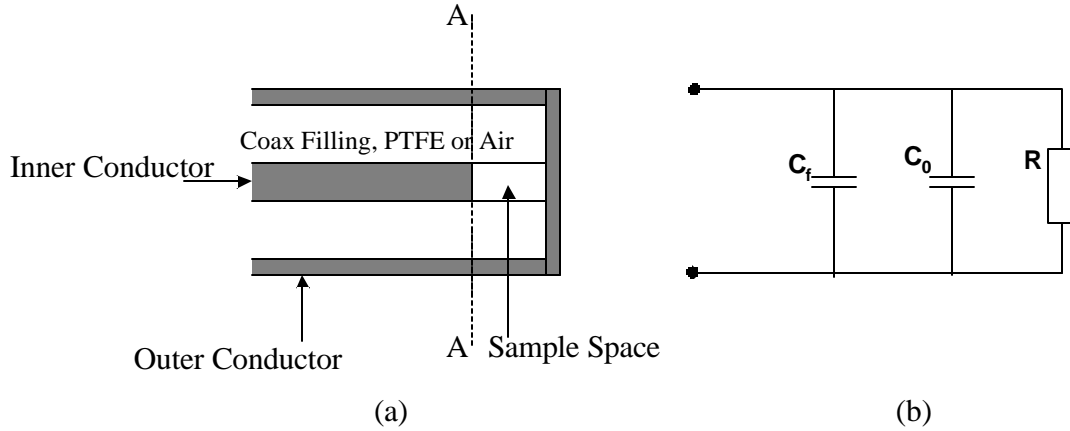


**Figure 3.2 - (a) Coaxial line terminated by a capacitive gap (sample space) (b) Equivalent lumped element model looking into A-A**

The total capacitance of the model is described by:

$$C_T = C_0 + C_f \quad (3.1)$$

Referring to Figure 3.2(b),  $C_f$  is the capacitive fringing field in the coaxial line dielectric (PTFE (Teflon) or air),  $C_0$  is the fringing capacitance inside the air or material under test (*MUT*) and  $R$  is radiation loss. The capacitive fringing field  $C_0$  interrogates the sample material during measurement and is the term which provides the basis for permittivity extraction. The radiation resistance,  $R$ , can be ignored if the ratio of the radius of the probe centre conductor to the wavelength is less than one [9]. From analysis of Figure 3.2(b) and the measurement of input reflection coefficient in time or frequency domain, the permittivity of the *MUT* can be quantified [9].

A flanged coaxial probe system with novel calibration standards has been developed at the *US* by Rimbi [10] (Figure 3.3). Flange dimensions are  $20 \times 20 \text{ mm}$ . The principle of operation is the same as the system in Figure 3.2(a) with the advantage that calibration is done at the plane of measurement [10]. A full one port calibration is done using an open circuit, short circuit and matched load calibration standards. Calibration of the flanged probe and standard definitions has been investigated and can be found in Louw [29].

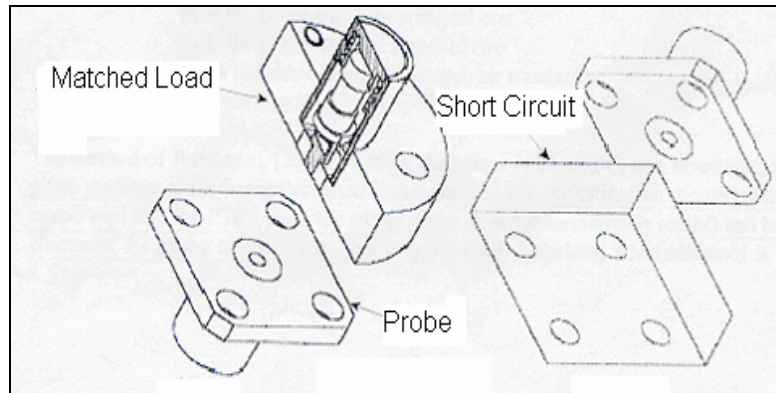


Figure 3.3 – Flanged Coaxial-probe with calibration standards, (after Rimbi [10])

The measurement comprises the probe being connected to an ANA via a 50Ω coaxial cable. The system is then calibrated (flush with the plane of measurement) to eliminate systematic errors regarding the ANA and pushed flush against the material of interest. A calibrated  $S_{11}$  parameter (reflection coefficient) is extracted over a wide frequency range. The data are then utilised in an inversion algorithm implementing mathematics from Stuchly and Stuchly [9] and yield material permittivity as a function of frequency.

### 3.3.1 Lumped Element Model of the Flanged Coaxial Probe

When electromagnetic waves reach the end of the probe a capacitive fringing field is established between the inner and outer conductor. The same lumped element model as in Figure 3.2(b) can be applied to the flanged probe and is shown below.

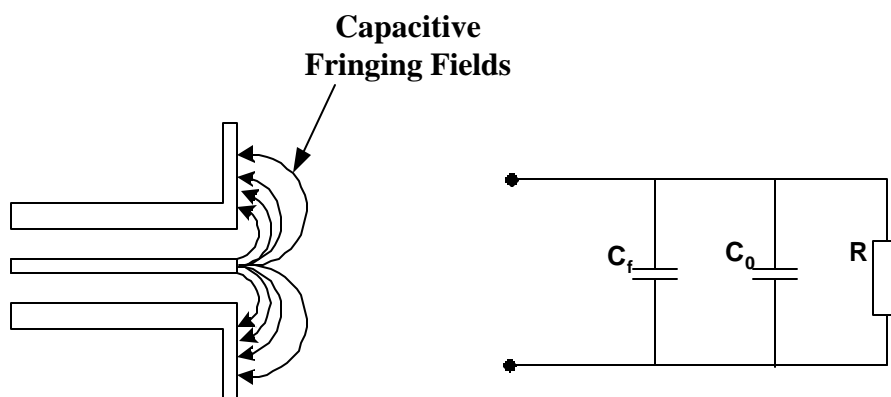


Figure 3.4 - Flanged coaxial probe and equivalent lumped element representation

$C_f$  is the capacitive fringing field in the coaxial line (PTFE or air dielectric),  $C_o$  is the fringing capacitance outside the probe (inside air or *MUT*) and  $R$  is radiation loss. The capacitive fringing field outside the probe ( $C_o$ ) interrogates the sample material during measurement. The radiation resistance,  $R$ , can be ignored as stated previously. The fringing capacitance inside the coaxial line ( $C_f$ ) can create confusion, since unlike the model in Figure 3.2; the probe is now flush against the *MUT*. It was shown by Fouché [30] using the method of curvilinear squares that  $C_f$  in the flanged probe does exist, but is small compared to  $C_o$ , for the probe radiating into free space. Therefore, *prior to calibration*, (3.1) is also applicable to the flanged coaxial probe and after calibration it is a function of the sample being interrogated. This will be discussed next.

### 3.3.1.1 Probe Calibration and $C_f$

The open circuit calibration standard is represented by the probe radiating into air. With the help of the National Institute of Standards and Technology (*NIST*) in the United States of America (*USA*), the phase shift introduced by the *total fringing capacitance* of the probe ( $C_T$ ), was determined by full wave analysis. The total capacitance of the open circuit can then be quantified according to [21] by the following equation:

$$C_{eff} = C_T = \frac{\tan\left(\frac{f}{2}\right)}{2p f Z_0} \quad (3.2)$$

$f$  = phase shift introduced as a results of the total fringing capacitance of the probe

Hewlett Packard (*HP*) [21] then uses a 3<sup>rd</sup> order polynomial fit to model the open standard's capacitance as a function of frequency:

$$C_{eff}(f) = C_T(f) = C_3 f^3 + C_2 f^2 + C_1 f + C_0 \quad (3.3)$$

The coefficients have been determined by Louw [29] and are  $C_0 = 29,709$  [fF],  $C_1 = -3.3797$  [ $10^{-27}$ F/Hz],  $C_2 = 10.221$  [ $10^{-36}$ F/Hz<sup>2</sup>] and  $C_3 = -4.555$  [ $10^{-45}$ F/Hz<sup>3</sup>]. These numbers then form part of the open circuit calibration standard's definition as used by the ANA.

Since the open circuit standard definition includes the effect of  $C_f$ , only  $C_0$  can exist after calibration (i.e.  $C_T = C_0$ ). However,  $C_f$  is a function of the material that is being measured and calibration is unique to the reference material, in this instance air. If another material, e.g. *PTFE*, is measured, the effect of  $C_f$  is reintroduced and  $C_T = C_0 + C_f$ . A new calibration could be done for different materials, but this would require another full wave solution, unique to the specific material, and an *a priori* knowledge of the materials properties to perform the full wave analysis.

Stated differently; the probe will always measure  $C_T$ , unless air is measured after calibration in which case  $C_0$  is determined.

### 3.3.2 Analytical Solution for Permittivity

Rimbi [10] suggested an analytical solution that assumes an *air filled* coaxial line, radiating into free space, where both  $C_f$  and  $C_0$  are quantified. This assumption is not applicable to our *PTFE filled* coaxial probe, and as already discussed,  $C_f$  is unique to the *MUT*.

Instead, no attempt was made here to separate  $C_T$  into  $C_0$  and  $C_f$ . Soon after calibration air was measured as a reference material and  $C_0$ , for the probe radiating into air, could be determined (3.2). The probe is then pushed flushed against the *MUT*, and the measured  $S_{11}$  is used in equations developed by Stuchly and Stuchly [9] to determine the permittivity:



$$\mathbf{e}_{unknown}' = \frac{2|S_{11}|\sin(-\mathbf{f})}{\mathbf{w}Z_0C_0\left(1+2|S_{11}|\cos(\mathbf{f})+|S_{11}|^2\right)} - \frac{C_f}{C_0} \quad (3.4)$$

$$\mathbf{e}_{unknown}'' = \frac{1-|S_{11}|^2}{\mathbf{w}Z_0C_0\left(1+2|S_{11}|\cos(\mathbf{f})+|S_{11}|^2\right)} \quad (3.5)$$

According to Stuchly and Stuchly [9] both  $C_0$  and  $C_f$  in (3.4) are determined from measurement of a reference material. Stuchly and Stuchly [9] makes the assumption that  $C_f$  changes minutely when measuring a *MUT*. For the flanged probe, using air as the reference material,  $C_f$  will be ignored. The second term in (3.4) is included to show the general form of the equation. However, when pushed against the *MUT*, the probe measures  $C_T$ . The magnitude ( $|S_{11}|$ ) and phase ( $\mathbf{f}$ ) of  $S_{11}$  of the *MUT* is affected by the reintroduction of  $C_f$  (will cause a phase shift), and a small error is introduced in the measurement.

This analytical solution has been implemented in Matlab<sup>®</sup> and will be used throughout this thesis unless stated otherwise. The code can be found in Appendix D.

### 3.3.3 Simplified Circuit vs. Full Wave Inversion

The permittivity of rexolite (cross linked polystyrene) and fused silica was determined in a resonant cavity by *NIST*. These same samples were then sent to the University of Stellenbosch (*US*) where probe measurements were conducted on them. The permittivity was extracted from the measured  $S_{11}$  by the simplified inversion technique (described above) and a full wave inversion technique [28] with the help of *NIST*. The full wave inversion technique is expected to be more accurate as it takes evanescent modes (excited at the end of the probe) into account. Both of these inversion algorithms were then compared to the independent resonant cavity technique. Simplified and full wave comparative figures and tables are presented next.

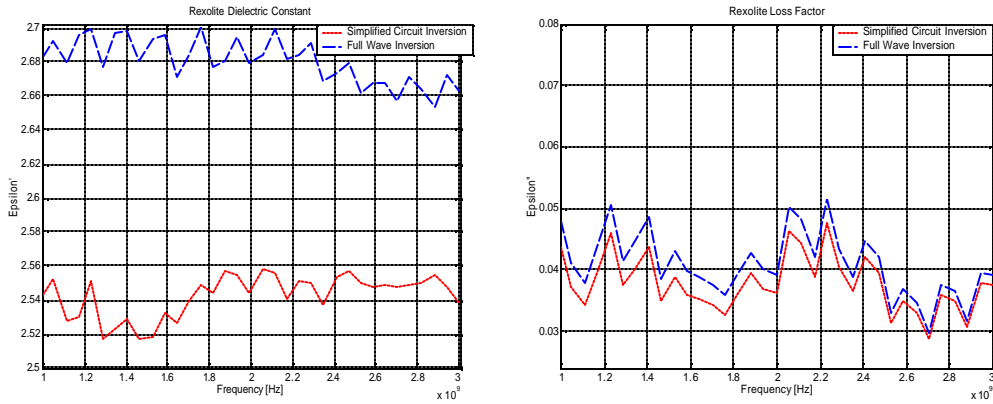


**Figure 3.5 - Full wave and simplified circuit inversion techniques comparison for Rexolite**

The following table shows a comparison for rexolite between the different techniques compared to an independent cavity resonant technique as reference.

**Table 3.1 – Comparison of inversion techniques for rexolite with a resonant cavity system**

Technique	$\epsilon_r'$	$\epsilon_r''$	% Error on resonator $\epsilon_r'$	% Error on resonator $\epsilon_r''$
Simplified (Median Values)	2.55	0.037	0	3754 (Order of magnitude)
Full Wave (Median Values)	2.66	0.04	4.3	4067 (Order of magnitude)
Cavity Resonator (2 GHz)	2.55	0.00096	0	0

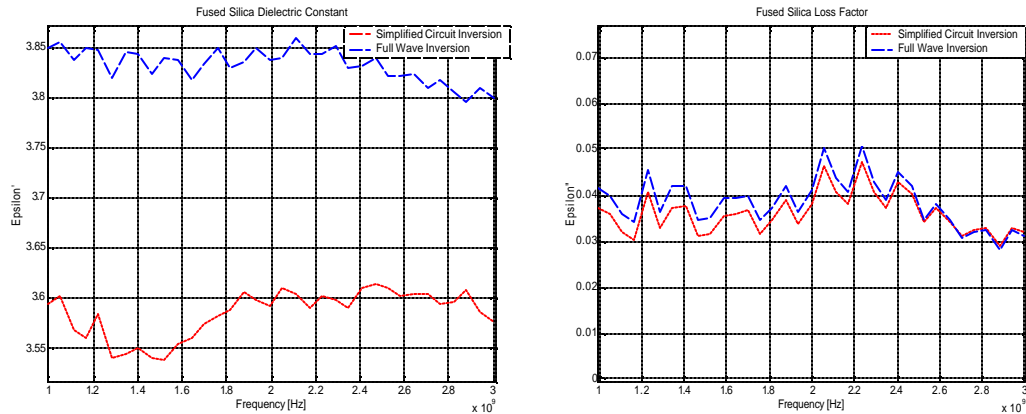


**Figure 3.6 - Full wave and simplified circuit inversion techniques comparison for Fused Silica**

The following table shows a comparison for fused silica between the different techniques compared to an independent cavity resonant technique as reference.

**Table 3.2 – Comparison of inversion techniques for fused silica with a resonant cavity system.**  
Median values (to ignore extreme data) are taken in the frequency range between 2 – 3 GHz

Technique	$\epsilon_r'$	$\epsilon_r''$	% Error on resonator $\epsilon_r'$	% Error on resonator $\epsilon_r''$
Simplified (Median Values)	3.6	0.037	5.8	19271 (2 orders of magnitude)
Full Wave (Median Values)	3.81	0.04	0.26	20842 (2 orders of magnitude)
Cavity Resonator (3.3 GHz)	3.82	0.000191	0	0

It is expected that the level of accuracy using the simplified inversion technique will differ depending on the variation in  $C_f$  for different materials under test. Also, a qualitative analysis of (3.4) and (3.5) reveals that the dielectric constant is more sensitive to the measured phase and the loss factor is more sensitive to the magnitude of the measured  $S_{11}$ . Since the simplified analysis ignores  $C_f$  (i.e. phase shift), a larger difference shows in the dielectric constant between the simplified and full wave comparison than for the loss factor. Note that as the simplified inversion ignores the effect of  $C_f$  the full wave analysis (which takes higher order modes into account) must give a more accurate result.

Compared to an external reference, the dielectric constant of the simplified inversion technique shows a better result for rexolite than the full wave inversion technique. Conversely, the dielectric constant of the full wave inversion technique shows a better result for fused silica than the simplified inversion. It is expected that measurement of materials with higher dielectric constants will be less accurate using the simplified inversion technique due to the effect of  $C_f$ . However, the accuracy achieved by the simplified inversion technique for the rexolite dielectric constant is anomalous (refer to

paragraph above). It is clear that the probe, which is a reflection measurement system, cannot determine the loss factor of low loss materials. The inability to describe the probe matched load standard accurately in the *ANA* standards' definition is thought to contribute to this. The probe did measure the dielectric constant accurately for both of these materials.

### 3.3.4 Measurement Error

Connectors are not perfect and reflections occur between transitions. Calibration of the system is an attempt to get rid of these reflections (directivity) through the measurement of a matched load standard. The matched load is not perfect and reflections from the matched load during calibration will affect subsequent measurements. These reflections, together with probe lift off (air gap between probe and material), are the main sources of error that is part of the measurement. Other factors include temperature drift and bending of cables.

### 3.3.5 Remarks on the Flanged Coaxial Probe Measurement System

In point form the following remarks can be made about the probe system:

1. The probe can measure permittivity over a wide frequency range (1 – 3 GHz).
2. A well defined flat and smooth area of at least  $20 \times 20 \text{ mm}$  is needed to make measurements.
3. It is expected that the probe cannot measure conductive materials since this will create a short circuit between the inner and outer conductors of the coaxial system, i.e. no capacitive interrogation is possible.
4. Special care must be taken to prevent lift off.
5. The probe will not be able to measure magnetic materials since the measurement technique is based on capacitive interrogation.
6. The probe measures location specific permittivity on the surface of a material.
7. The probe will be more accurate for materials with lower dielectric constants. This is because  $C_f$  is more affected by measurement of materials with higher dielectric constants.

### 3.4 Waveguide Measurement System

#### 3.4.1 WG Theory: An Overview

Waveguide (Figure 3.7) only allows electromagnetic waves above a critical frequency (cutoff frequency) to propagate.

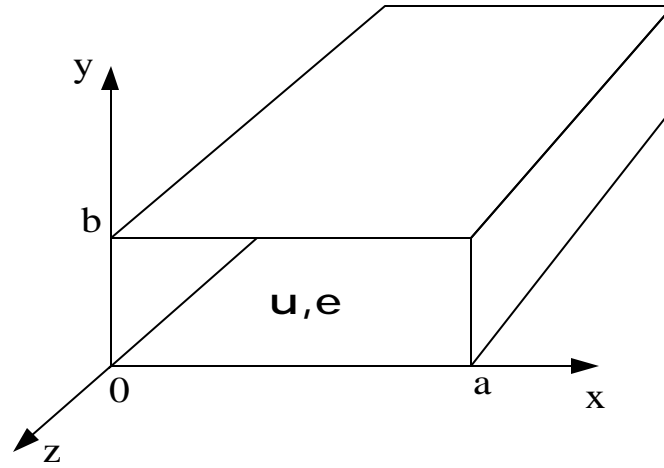
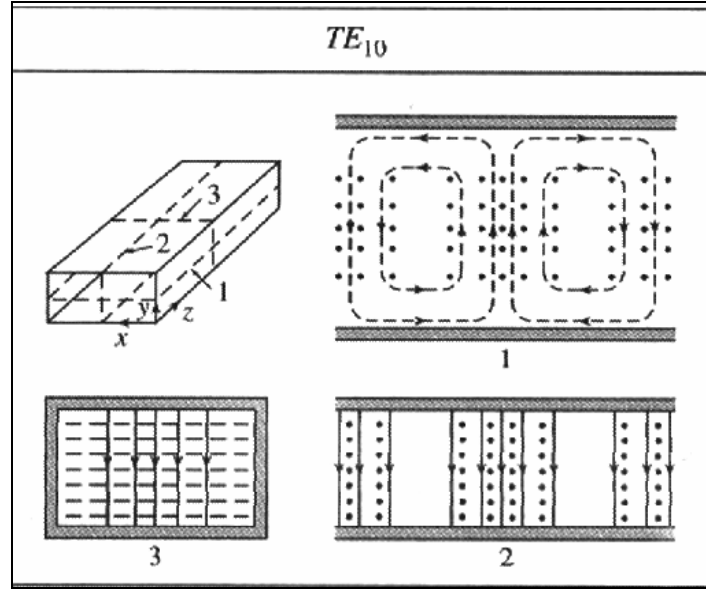


Figure 3.7 - Geometry of rectangular waveguide, (after Pozar [12])

Different modes can propagate at different frequencies and according to Pozar [12] the cutoff frequency for a specific mode in rectangular WG is calculated by the following equation:

$$f_{c_{mn}} = \frac{1}{2p\sqrt{\mu e}} \sqrt{\left(\frac{mp}{a}\right)^2 + \left(\frac{np}{b}\right)^2} \quad (3.6)$$

The variables are indicated in Figure 3.7. The mode with lowest cutoff frequency is called the dominant mode and in rectangular waveguide corresponds to the  $TE_{10}$  mode. The magnitude of the electric and magnetic field distributions of the  $TE_{10}$  mode in rectangular WG are presented in Figure 3.8.



**Figure 3.8 - Magnitude of Electric and Magnetic field distribution of  $TE_{10}$  mode in rectangular WG, (after Pozar [12])**

The solid lines indicate electric field lines and the dotted lines magnetic field lines. The electric field has only a  $y$ -component whereas the magnetic field has both an  $x$  and  $z$  component. For a complete analytical analysis of different modes in  $WG$  refer to Pozar [12].

In a general medium, the wavelength of a  $TE_{10}$  mode in rectangular  $WG$  is longer than a transverse electromagnetic ( $TEM$ ) wave of the same frequency and is quantified by Kraus et al. [31] as:

$$\lambda_g = \frac{\lambda_0}{\sqrt{\epsilon_r \mu_r - \left(\frac{\lambda_0}{\lambda_c}\right)^2}} \quad (3.7)$$

Where:  $\lambda_g$  is the wavelength in the waveguide

$\lambda_0$  is the free space wavelength

$\lambda_c$  is the mode cutoff frequency

(3.7) is true for all  $TE$  modes in rectangular waveguide filled with a general medium.

### 3.4.2 Measurement Setup

In the measurements to follow a two port rectangular *WG* measurement system is employed and setup as in Figure 3.9.

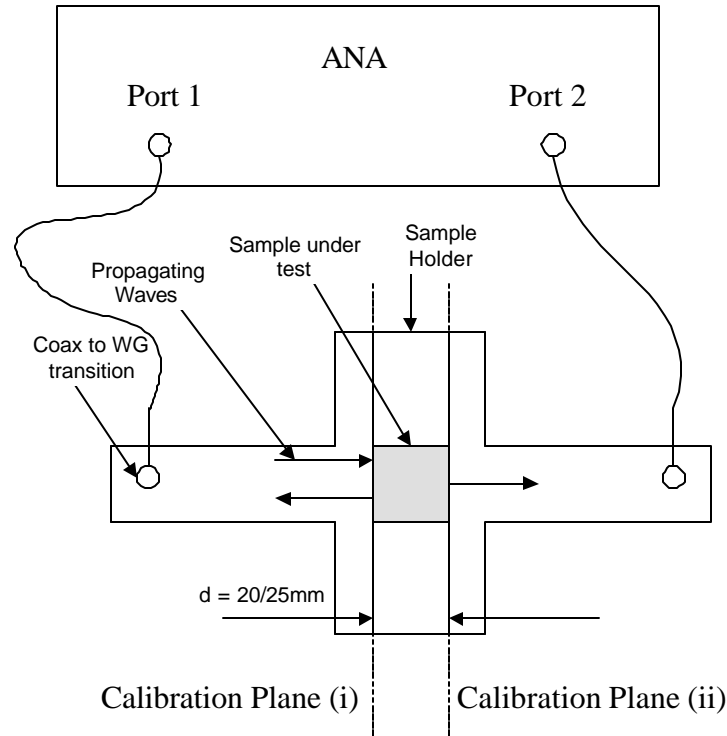


**Figure 3.9 - Physical representation of WG measurement setup; Transverse Section**

The dimensions of the *WG* are  $72 \times 34 \text{ mm}$  (WR-284). Although the cutoff frequency of the  $TE_{10}$  mode is  $2.078 \text{ GHz}$ , the recommended operating frequency range is  $2.60\text{-}3.95 \text{ GHz}$  (*S-band*) [12]. Note that *above*  $3.95 \text{ GHz}$  the next higher order mode ( $TE_{20}$ ) will start to propagate. The  $TE_{10}$  mode is excited in the system via the coax to *WG* transitions positioned in the middle of the *WG* (x-dimension). A full two port calibration is done using the following calibration standards:

- 2 Offset short circuits
- Sliding matched load
- Fixed matched load
- Thru standard (Two flanges at reference planes are bolted together)

The reference planes at either port are as indicated in Figure 3.9.

For a comprehensive description of the full two-port *WG* calibration technique refer to [21]. After calibration, a sample is placed inside a sample holder that is sandwiched between the two waveguide sections flush with the calibration planes. During measurement the  $TE_{10}$  mode interrogates the *MUT* and all four S-parameters ( $S_{11}$ ,  $S_{21}$ ,  $S_{22}$  and  $S_{12}$ ) are extracted via a computer connected to the *ANA*.

Two sample holders were used during measurements, with the length  $d$  (from Figure 3.9) as variable. Dimensions are  $(72 \times 34 \times 20/25)$  mm and Figure 4.1 shows a picture of one of them. The 25 mm sample holder will be referred to as sample holder 1 (*SH1*) and the 20 mm sample holder will be referred to as sample holder 2 (*SH2*). The two sides of *SH1* were covered with thin films of plastic, taped onto the metal. This helped to contain mixtures (rock particles, powder or liquid) in the sample space. Both *SH1* and *SH2* were used for measurements of solid samples (rectangular slabs), cut (as best as possible) to the dimensions of the cavity.

Some findings, not seen in any of the accessed literature, on the sliding matched load standard are of importance and discussed in the following section.

### 3.4.3 WG Matched Load Calibration Standard

An ideal matched load standard absorbs all incident energy and is used to calculate the directivity error (unwanted reflections in the measurement system) and port isolation (for a two port calibration; this requires two matched load standards). A common design for a *WG* matched load is to insert a wedge of a material with high loss at microwave frequency into a length of *WG*. Depending on the level of accuracy required, a longer or shorter wedge can be used. It is however not possible to manufacture a perfect matched load and some of the incident power will be reflected from the end of the load. This reflected power introduces a small error vector into the calibration. A sliding load can be used to change the phase of this error vector (moving in a circle around the origin of the



Smith chart) and approximate a zero reflection coefficient (middle of the smith chart). This idea is shown in Figure 3.10.

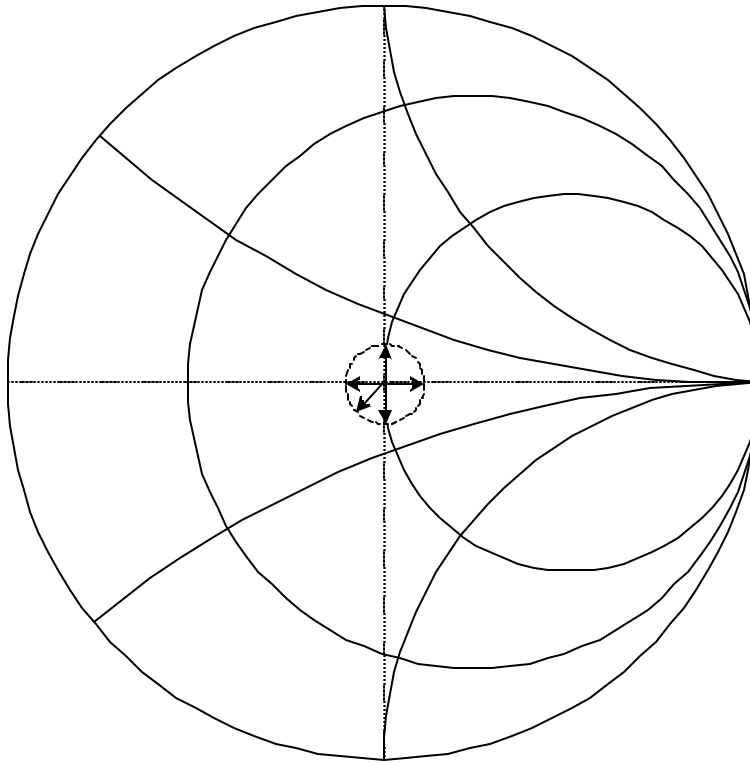


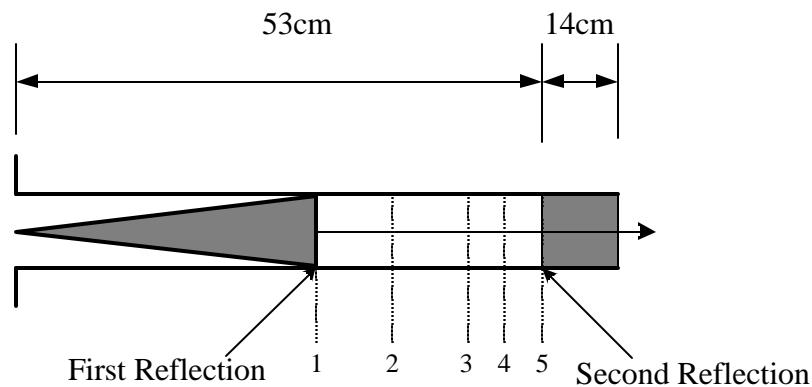
**Figure 3.10 - Five different reflection coefficients for five different positions of the sliding load**

A sliding load for the S-band WG system using a carbon-doped foam wedge was designed and built at the US (Figures 3.11 and 3.12). A block of carbon foam was also inserted at the open end of the WG to help absorb energy not dissipated by the wedge (Figure 3.12).



**Figure 3.11 - WG sliding load standard**

The positioning of the carbon foam wedge was designed to move the error vector from  $0$  to  $270$  degrees on the Smith chart at  $3.25\text{ GHz}$  (centre frequency between  $2.6$  and  $3.95\text{ GHz}$ ). Using (3.7) the wavelength in the guide at  $3.25\text{ GHz}$  was calculated to be  $118.43\text{ mm}$ . On the Smith chart half a wavelength moves the phase angle of the error vector once around the chart. Relating half a guide wavelength ( $59.22\text{ mm}$ ) to  $360$  degrees on the chart the offset distances were calculated as shown in Figure 3.12.



Position	Phase Offset [Degrees]	Physical Offset [mm]
1	0	0
2	90	14.81
3	180	29.61
4	225	37.01
5	270	44.42

**Figure 3.12 - Schematic of the positioning of the sliding load. Positions 1 to 5 moves the error vector from  $0$  to  $270$  degrees on the Smith chart**

Note that not all the energy is reflected back at the end of the wedge (first reflection in Figure 3.12). The error vector from Figure 3.10 does not account for a second reflection (Figure 3.12) that will occur when the remnant energy reaches the end of the WG (usually terminated with a metal wall or open ended, or carbon foam in this instance). This second reflection is constant throughout calibration and introduces an offset error during calibration. This offset error spoils the circle shown in Figure 3.10 and the origin of the Smith chart cannot be approximated accurately (Figure 3.13).

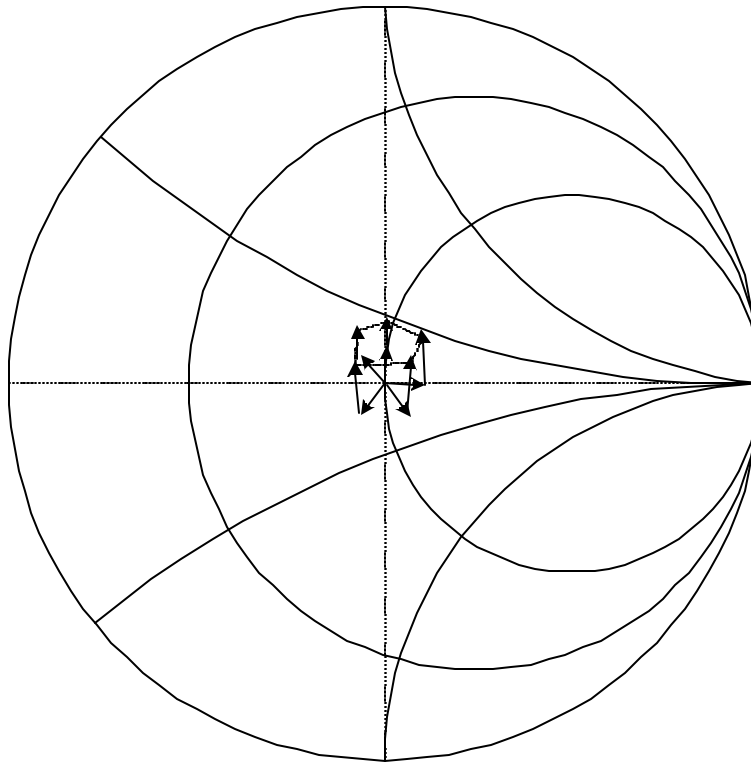


**Figure 3.13 - The residual energy not dissipated by the load and not reflected distorts the circle around the origin**

This unwanted reflection from the sliding matched load standard results in the *ANA* overcompensating for the directivity error coefficients. This error in calibration will affect all subsequent measurements.

### 3.4.3.1 WG Sliding Load Offset Error

To illustrate the effect of the offset error vector, Figure 3.14 presents a typical  $S_{11}$ -parameter of an arbitrary sample after calibration.

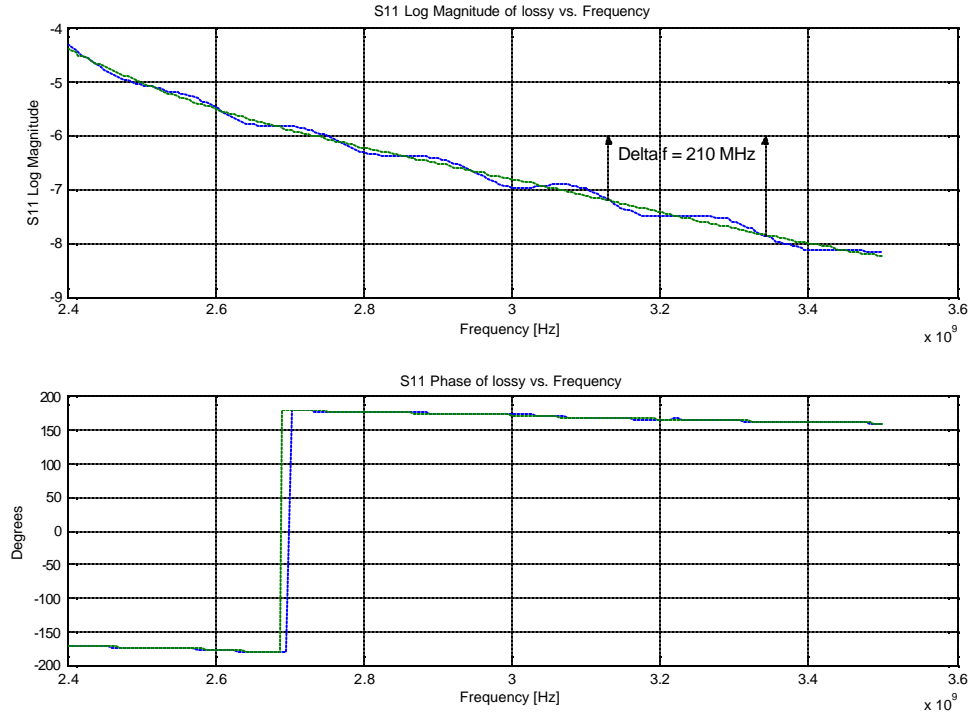


**Figure 3.14 - Typical measured  $S_{11}$  data of a MUT after calibration**

The oscillation in the magnitude and angle (seen on finer scale) of  $S_{11}$  is a result of the directivity overcompensation because of the constructive and destructive interference between incident and reflected waves in the sliding matched load standard.

The oscillation varies from  $170 \text{ MHz}$  at the low frequencies to  $220 \text{ MHz}$  at the higher frequencies. The period around  $3.25 \text{ GHz}$  corresponds to  $210 \text{ MHz}$  (Figure 3.14). This period in frequency is converted to distance inside the *WG* as follows. Let  $\Delta f = 210 \text{ MHz}$ ; this corresponds to  $t = 1/\Delta f = 4.7619 \text{ ps}$ . The velocity at which energy propagates in *WG* is known as group velocity ( $v_g$ ) and can be calculated from Kraus et al. [31] as:

$$v_g = \frac{c^2}{v_p} \quad (3.8)$$

Where  $c$  is the speed of light in a vacuum ( $3 \times 10^8 \text{ m/s}$ );  $v_p$  is the phase velocity in the waveguide and can be calculated from Kraus et al. [31] as:

$$v_p = \frac{c}{\sqrt{1 - \left(\frac{f_c}{f_{centre}}\right)^2}} \quad (3.9)$$

Where  $f_c$  is the mode cutoff frequency (2.078 GHz for  $TE_{10}$  in S-band) and  $f_{centre}$  is 3.25 GHz. The phase velocity is then calculated from (3.9) as  $389.904 \times 10^6$  m/s and the group velocity from (3.8) as  $230.507 \times 10^6$  m/s. Using group velocity and the period of 4.7619 ns, the distance in the WG was determined to be approximately 1.09 m. Half of this length will represent the distance travelled in one direction and corresponds to 54.5 cm. This is approximately the same distance to the face of the carbon foam block at the back of the load (53 cm, Figure 3.12). The small error in calculation might be because  $f$  was approximated from the graph and can vary marginally. Also the group velocity is calculated for free space and will decrease a little as the energy interacts with the carbon foam wedge.

This calibration anomaly was eliminated by “smoothing” the measured S-parameters with Matlab®, using its *polyfit* function. The *polyfit* function does a least squares polynomial fit of the data. The “smoothed” data is also presented in Figure 3.14. The smoothing of measured WG data will be done throughout the thesis unless stated otherwise.

A better option would be to use time-domain gating to remove the ripple from the data. This must be done during calibration when measuring the matched load standard. Measured frequency domain data can be extracted from the ANA. It can then be converted to its time domain equivalent and the unwanted reflection removed. The gated data is then converted back to the frequency domain and used for calibration.

#### 3.4.4 Materials in WG: S-Parameter Point of View

Figure 3.9 showed a representation of the two port WG measurement setup. The  $S_{11}$  and  $S_{21}$  parameters are referenced to port 1 of the ANA and  $S_{22}$  and  $S_{12}$  are referenced to port 2 of the ANA. After calibration, if a homogeneous material is under test, the  $S_{11}$  and  $S_{21}$

parameters will be the same as the  $S_{22}$  and  $S_{12}$  parameters (i.e. interrogating the material from two opposite sides gives the same results). This is not true when measuring an anisotropic material as opposite sides of the material interact differently with incident waves.

Figure 3.15 presents comparative graphs of  $S_{11}$  and  $S_{22}$  of isotropic and anisotropic materials respectively.

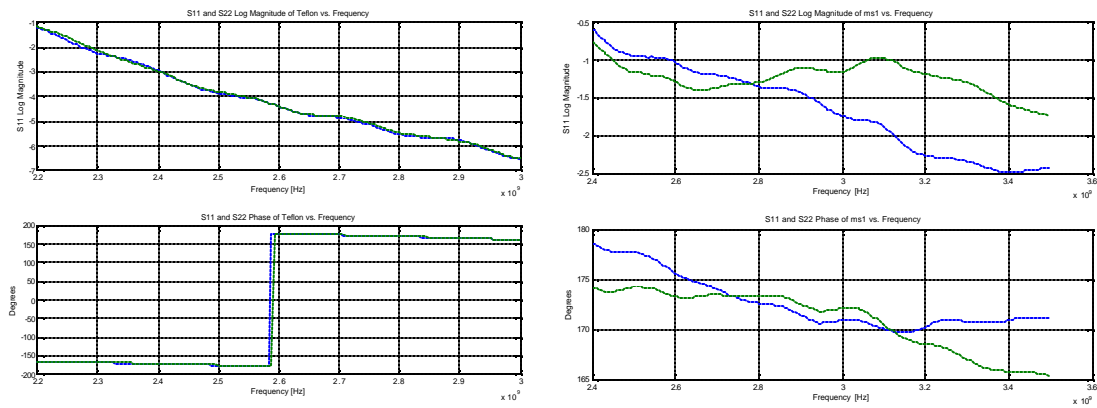


**Figure 3.15 -  $S_{11}$  and  $S_{22}$  parameters for both an isotropic and anisotropic material respectively**

From Figure 3.15 it is clear that the orientation of anisotropic materials is important when using the *WG* measurement system to quantify samples.

### 3.4.5 Inversion algorithm

Nicolson and Ross [32] and Weir [16] (*NRW*) developed an analytical solution for the permittivity and permeability by using the measured S-parameters (either  $S_{11}$  and  $S_{21}$  or  $S_{22}$  and  $S_{12}$ ). These equations are important in this thesis and are presented below:

$$\Gamma = K \pm \sqrt{K^2 - 1} ; \quad |\Gamma| \leq 1 \quad (3.10)$$

The correct sign is chosen such that  $|\Gamma| \leq 1$

$$K = \frac{\{S_{11}^2(\mathbf{w}) - S_{21}^2(\mathbf{w})\} + 1}{2S_{11}(\mathbf{w})} \quad (3.11)$$

$$T = \frac{\{S_{11}(\mathbf{w}) + S_{21}(\mathbf{w})\} - \Gamma}{1 - \Gamma\{S_{11}(\mathbf{w}) + S_{21}(\mathbf{w})\}}; \quad |T| \leq 1 \quad (3.12)$$

$$\frac{1}{\Lambda^2} = -\left[\frac{1}{2pd} \ln\left(\frac{1}{T}\right)\right]^2 \quad (3.13)$$

$$\mathbf{m}_r = \frac{1 + \Gamma}{\Lambda(1 - \Gamma) \sqrt{\frac{1}{I_0^2} - \frac{1}{I_c^2}}} \quad (3.14)$$

$$\mathbf{e}_r = \frac{I_0^2 \left( \frac{1}{\Lambda^2} + \frac{1}{I_c^2} \right)}{\mathbf{m}_r} \quad (3.15)$$

Where:  $I_c$  is the cutoff wavelength of the  $TE_{10}$  mode

$\Gamma$  is the reflection coefficient

$T$  is the transmission coefficient

In the determination of the permittivity and permeability, various operations are applied on the measured S-parameters. The quadratic operations will accentuate S-parameter data significantly ((3.10), (3.11) and (3.13)). The material properties will therefore be sensitive to irregularities in the measured S-parameters. This point is raised again in Section 4.5.2.

Referring to the previous section and Figure 3.15, it is obvious that an anisotropic material will produce two sets of material properties depending on the use of either  $S_{11}$  and  $S_{21}$  or  $S_{22}$  and  $S_{12}$  (See Table A.1 in Appendix A). Conversely, isotropic materials

will generate the same material properties irrespective of which parameters were used. Unless stated otherwise the  $S_{11}$  and  $S_{21}$  parameters were used throughout this thesis.

Two restrictions in the inversion process should be pointed out :

- A mathematical ambiguity occurs in (3.13) when the sample is longer than the guide wavelength inside the sample itself.
- The *NRW* solution is least accurate [22] and may break down [33] when the sample length is an odd multiple of one-half wavelength in the material.

The mathematical ambiguity and a proposed solution to it will now be discussed:

The  $\ln(1/T)$  in (3.13) must add a  $j2pn$  term since  $T$  is a complex number. The omission thereof will result in the principal value of (3.13) to be the default. When the sample is longer than one guide wavelength in the sample, a phase ambiguity occurs and the correct value of  $n$  must be chosen. Cloete [34] suggested a refinement to the *NRW* method by implementing a group delay technique to resolve the mathematical ambiguity. Cloete [34] suggested  $n$  to be calculated as:

$$n = \text{floor} \left( ft_g - \frac{f_i}{2p} \right) \quad (3.16)$$

Where  $t_g$  is the measured group delay through the sample and  $f_i$  is the imaginary part of the principal value of  $\ln(1/T)$ . The *floor* ( ) function always rounds down and is used since  $n$  must be taken into account *only if* the sample is *longer* than a guide wavelength in the sample. The analytical solution (taking Cloete's refinement [34] and the half-wavelength anomaly into account) was implemented in Matlab<sup>®</sup> code and can be found in Appendix D.



### 3.4.6 WG Measurement and Higher Order Modes

The *NRW* inversion algorithm assumes a single mode of propagation inside the sample [33]. Equation 3.6 shows that the cutoff frequency in rectangular *WG* is a function of both geometry and the material filling the *WG*. It can be seen from (3.6) that inserting a material inside the *WG* will lower the cutoff frequency of a mode. It is therefore possible that materials under test can support higher order modes. However, these modes will be generated *only* if the  $TE_{10}$  mode is perturbed inside the sample. In-homogeneity in materials or an air gap between the sample and the *SH* can provide the necessary perturbation.

According to Jarvis et al. [33] higher order modes generally lead to a sudden dip in the magnitude of the measured  $S_{11}$ . This is because of a change in the wave impedance. The inversion algorithm (Appendix D) tests if a sample material has properties that can support higher order modes and indicates the frequency points where this is possible. The  $S_{11}$  magnitude should then be checked for any irregularities. This approach is followed during the presentation of *WG* results.

### 3.4.7 Remarks on the Waveguide Measurement System

In point form the following remarks can be made about the *WG* measurement system:

1. The Sample materials have to have well defined geometries.
2. The *WG* is band limited to  $2.6 - 3.95 \text{ GHz}$
3. Both magnetic and electric properties can be quantified.
4. It is suspected that the *WG* cannot measure conductive materials as very little or no energy will reach port two of the measurement system.
5. The sliding load standard introduces an unwanted ripple effect that will be smoothed out of all subsequent measurements.
6. Isotropic (Homogeneous) materials will yield the same results regardless of the orientation of interrogation of the sample.

7. Anisotropic materials will yield different results depending on the orientation of interrogation of the sample.
8. It is expected that measured material properties will be very sensitive to irregularities in measured S-parameters due to quadratic operations on them.

### **3.5 Conclusion**

Various measurement systems were discussed in Section 3.2 and it was found in the literature that transmission-reflection measurement systems cannot measure low loss factors accurately. A flanged coaxial probe with novel calibration standards, developed by Rimbi [10] was introduced in Section 3.3. Calibration is done at the plane of measurement. A simplified inversion algorithm used for probe measurements was found to compare well with a full wave solution of the same measurements. Fringing capacitance inside the probe hampers the level of accuracy achieved by probe measurements for materials with higher dielectric constants. Comparison of both of these techniques to an independent resonant cavity measurement of the same materials revealed the probe does measure the dielectric constant accurately, but cannot measure the loss factor of low loss materials. The limit on the low loss factor measurement is thought to be because of an inability to describe the matched load standard accurately in the *ANA* standard definition.

A two port *WG* measurement system was introduced and its matched load calibration standard was discussed. The sliding matched load introduces unwanted reflections that is built into all subsequent measurements, but will be removed by smoothing the measured data using Matlab<sup>®</sup>. The *WG* inversion algorithm (based on the *NRW* solution) will reveal different material properties for anisotropic materials depending on the orientation of interrogation. A mathematical ambiguity occurs in the *NRW* inversion technique and a suggested solution by Cloete [34] was implemented in the inversion code. Higher order modes might be induced in the measurement of inhomogeneous materials.

# Chapter 4

## Material Property Measurement

---

### ***4.1 Introduction***

Material properties, introduced in Chapter 2, as a function of frequency are quoted in literature for a wide range of materials. The literature is extensive and the best known applicable reviews are to be found in [15], [20] and [4]. Naturally occurring mineral ores are multiphase mixtures which show variation in both composition and mineral texture, making absolute determination of material properties not possible. This Chapter will investigate multiphase copper carbonatite ore with the available measurement techniques (introduced in Chapter 3).

The ANA and equipment setup for material properties measurement are introduced in Section 4.2. The various materials and their preparation are introduced in Section 4.3. While carbonatite ore is of primary interest, monolithic and particulate rocks are also examined. Section 4.4 gives a summary of all the measurements that will be presented in the next two sections. Characterisation of a homogeneous isotropic material will be the starting point (Section 4.5). Its material properties are compared to literature values as a verification of the measurement systems. In Section 4.6 carbonatite ore is considered both in its solid and crushed forms. Section 4.7 summarises results and some conclusions are drawn (Section 4.8). Measurements on known materials (S-parameters, permittivity and permeability for both probe and WG) made during the course of this work are included in Appendix A.

## 4.2 ANA Setup for Material Properties

Unless stated otherwise, the following applies to all measurements made with the probe and WG systems; for brevity this is given in point form:

- ANA on for longer than 45 minutes prior to calibration to reach thermal stability
- Frequency sweep in step mode. The source phase locks at each of the frequency points before a measurement is taken. Gives good repeatability
- Averaging<sup>1</sup> set to 128 or 256
- 51 frequency points measured in the desired frequency range
- Full one-port calibration done for the probe
- Full two-port calibration done for the WG (including isolation)

Cables and connectors were cleaned using *n-butyl acetate* and dried by blowing compressed air over them. The Standard Military Adapters (SMA) were tightened using a torque wrench to guarantee the same contact every time and to prevent over-tightening. An anti-static wrist band was worn to ensure a static-free environment. The same phase stable cables were used for every measurement. This minimises phase shift when cables are bent. Even so, movement of the cables must be limited to a minimum. Finally the cables were handled as little as possible. This prevents the cable dielectric from heating (thermal drift) which will result in a change of dielectric property inside the cable. All experiments were done at room temperature.

---

<sup>1</sup> Averaging in the Step Mode is accomplished by multiple readings of the data at each frequency point and taking the average, i.e. Displayed Point =  $n \text{ Readings} / n$ ; where  $n$  = Averaging Factor.

### 4.3 Materials of Interest and Sample Preparation

#### 4.3.1 Homogeneous Materials

Teflon (PTFE) is characterised as a reference material in this chapter, but results on Perspex and a carbon foam material can be found in Appendix A. Perspex and PTFE have been characterised at microwave frequencies [20], [4] and values are listed in Table 4.1.

**Table 4.1 - Permittivity and permeability values of PTFE and Perspex as quoted in literature [20], [4]**

PTFE (1.6 GHz, 22°C and 3 GHz, 22°C)				Perspex (1.6GHz, 22°C and 3 GHz, 27°C)			
$\epsilon_r'$	$\epsilon_r''$	$\mu_r'$	$\mu_r''$	$\epsilon_r'$	$\epsilon_r''$	$\mu_r'$	$\mu_r''$
2.08	0.00076	1	0	2.5	0.018	1	0
2.1	0.0003	1	0	2.6	0.015	1	0

The first row of results is as quoted by von Hippel [20] and the second row by Metaxas and Meredith [4]. The conditions specified at the top apply to [20] and [4] respectively.

The carbon foam (Appendix A) consists of individual polystyrene balls that are immersed in a carbon enriched liquid. After a pre-determined period of time the polystyrene balls are taken out of the solution and compressed. This material was developed for research on an effective earth medium [35] and has not been characterised before.

#### 4.3.2 Copper Carbonatite Ore

The multiphase (inhomogeneous, anisotropic) ore under investigation was a copper carbonatite and is mined at Palabora, South Africa. According to Kingman et al. [8], representative portions of the sample were analysed to determine its composition. The analysis revealed that the carbonatite consisted of various proportions of at least eight

different minerals (phases). Magnetite ( $Fe_3O_4$ ) was found to be abundant (approximately 20%) and carbonate minerals such as calcite ( $CaCO_3$ ) and dolomite ( $CaMg(CO_3)_2$ ) were found to be particularly copious [8]. The other minerals amount to less than 10% of the carbonatite ore. A simplified yet reasonable model of the carbonatite ore will be to ignore the scant minerals and approximate the carbonate materials (will be referred to as calcite) as occupying 80% of the ore. Therefore during the rest of this thesis, unless stated otherwise, carbonatite ore is approximated as a composition of 20% magnetite and 80% calcite. It is important to note that as carbonatite is a naturally occurring composition of rocks, differences between samples are expected. Figure 4.1 shows a photograph of the slab of carbonatite used during measurements.

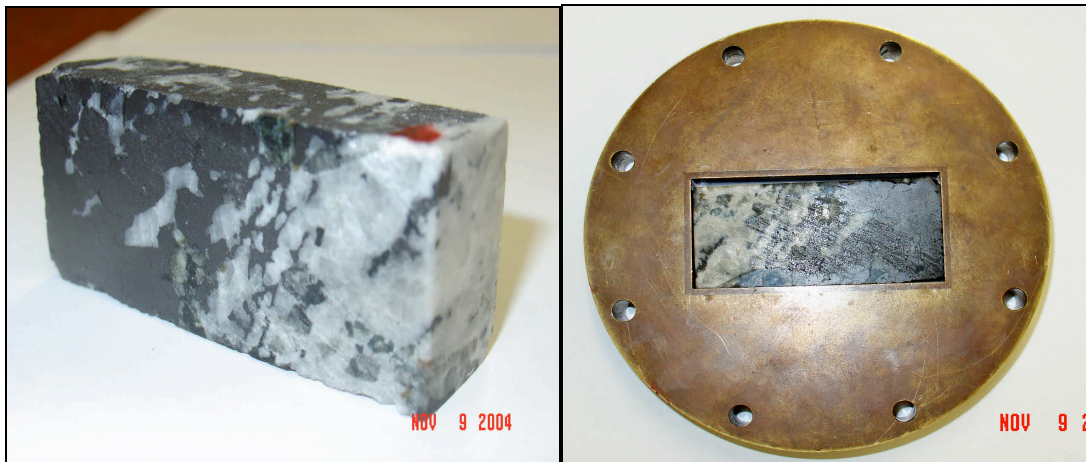


**Figure 4.1 - Rectangular slab of carbonatite used by the waveguide measurement system**

Individual slabs of calcite and magnetite (Figure 4.2) were also obtained and characterised individually. From Figure 4.2, a visual inspection of the calcite (white) sample reveals other phases are still present. The calcite sample will be *approximated* as homogeneous in the *WG* measurements.



**Figure 4.2 - Rectangular slabs of calcite and magnetite used in the probe and WG measurements**

### 4.3.3 Sample Preparation

The homogeneous materials (PTFE, Perspex and carbon foam) are malleable and were prepared to fit tightly into either one of the sample holders ( $72 \times 34 \times 20$  or  $25$ ) mm. The ore on the other hand is difficult to cut to the exact dimensions and the slabs does not fit perfectly in the *SH* (e.g. Figure 4.1). There is a gap at the top of approximately 2 mm along the length. However, the calcite sample fits better into the *SH* than the slab of carbonatite.

The magnetite sample is brittle, making it even more difficult to cut to the correct dimensions. Being brittle, some magnetite crumbled away during preparation leaving holes in the sample.

Crushed carbonatite ore was also put in *SHI* (Figure 4.3) and measured to obtain a bulk property of the rock/air mixture. The crushed ore consists of rocks of various shapes and sizes. In general though, a cross sectional area resembles elongated and angular shapes, with the longer side approximately 20mm long. Using a water-displacement technique the packing density of the *SH* cavity was found to be 44% rock to 56% air.

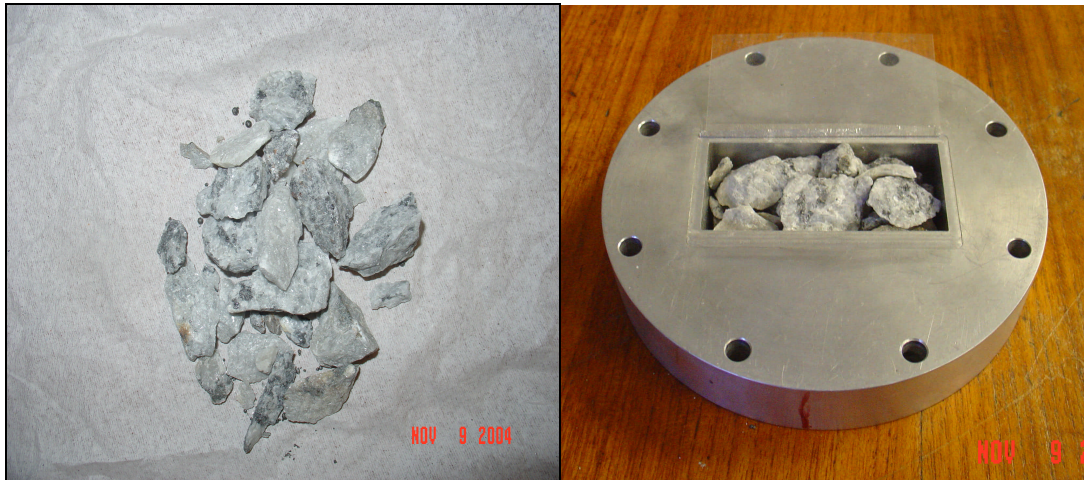


Figure 4.3 - Crushed carbonatite rocks used during measurements made by the waveguide system

## 4.4 Summary of Proposed Measurements

Table 4.2 gives a summary of the key measurements made (or were not possible) and whether literature values are available (or not).

Table 4.2 - Summary of materials measured using both measurement techniques

<u>Material</u>	<u>Probe</u>	<u>WG</u>	<u>Literature</u>
<u>Homogeneous</u>			
PTFE	v	v	v
Perspex (Appendix A)	v	v	v
Carbon Foam (Appendix A)	v	v	X
Calcite	v	v	v
Magnetite (Appendix A)	X	X	v X
<u>Inhomogeneous</u>			
Carbonatite	X	v	X
Crushed Ore	X	v	X

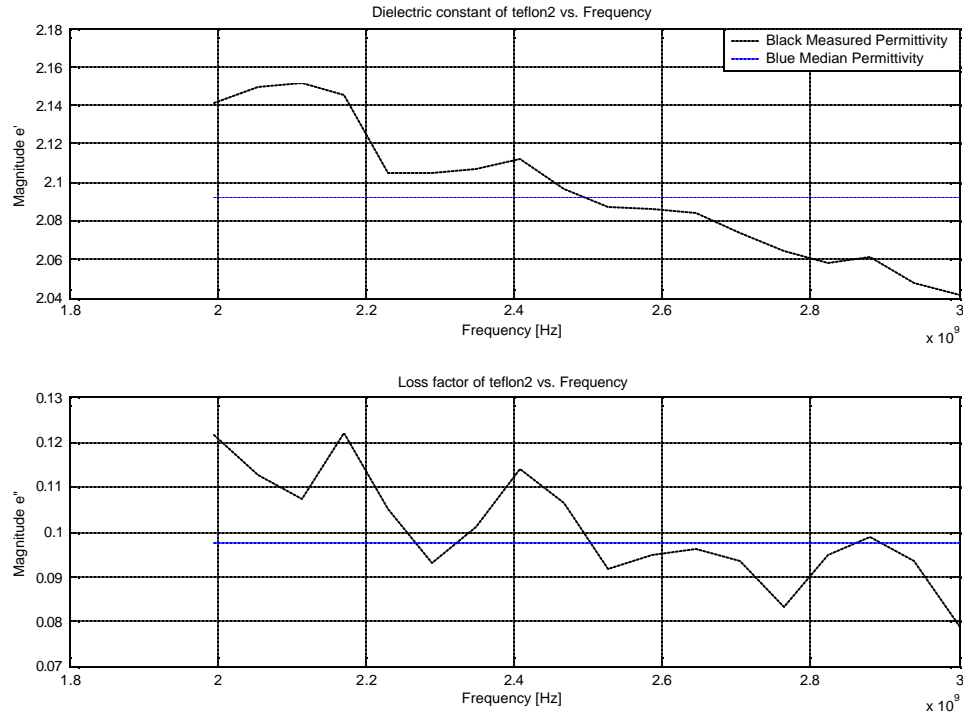


The X indicates that no measurement could be performed or no data was available in the accessed literature. The v indicates that measurement was possible or that literature data were available. The double marking for a literature definition of magnetite needs explanation. According to literature [13], [36], magnetite is a magnetic and conductive mineral. Shuey [37] recorded the conductivity of magnetite to vary from  $50 \text{ S/m}$  to  $3 \times 10^4 \text{ S/m}$  and did not provide a definite value for this specific case. A value for the permeability was found in [36], but this value was not related to a frequency. Table 4.2 is presented again at the end of this chapter and shows results from measurements and literature data.

## ***4.5 Measurement of Homogeneous Materials***

### **4.5.1 Coaxial Probe Measurements**

All materials of interest were polished to provide a flat and smooth surface of at least  $20 \times 20 \text{ mm}$  for probe measurements. The *median* values between  $2\text{-}3 \text{ GHz}$  are compared to literature values and quoted below every figure. This is followed by a discussion of results.

**PTFE (Teflon)**

Material	$\epsilon'_r$ (Probe)	$\epsilon''_r$ (Probe)	$\epsilon'_r$ (Literature)	$\epsilon''_r$ (Literature)
PTFE	2.09	0.097	2.08; 2.10	0.00076; 0.0003

**Figure 4.4 - Dielectric constant and loss factor of PTFE as measured with the coaxial probe**

Literature values are quoted from von Hippel [20] and Metaxas and Meredith [4] respectively under slightly different conditions (see Table 4.1 for detail of conditions).

Note that the scale on Figure 4.4 is fine. Measurements were made from  $45\text{ MHz} - 3\text{ GHz}$  but results are presented between  $2 - 3\text{ GHz}$ , because this is the range of primary interest in subsequent  $WG$  measurements and simulations. Also the median should be taken at higher frequencies, because  $C_0$  gets stronger with increasing frequency and an error phase shift would be a minimum. There is no quantification here of “higher frequencies”.

The decreasing trend in permittivity as a function of frequency is not a physical material property, but a result of phase shift during measurement. The coaxial cable was touched and bent during measurement in order to push the probe flush against the *MUT*. This and an air gap between the probe and the *MUT* will result in a measured phase shift. A phase shift of approximately *0.1 to 0.8 degrees* was measured over the frequency band for various measurements. This varied for each measurement because the cable and probe is not handled in exactly the same manner every time. To compensate for this, the error phase shift should be measured for every *MUT* and added to the phase of the extracted  $S_{11}$  parameter. This was not done here. However, it can be shown from (3.4) that the dielectric constant is sensitive to a phase-shift in the  $S_{11}$  of the *MUT* by implementing an artificial phase-shift, of *0.4 degrees* across the band. This straightens the dielectric constant over the frequency band. The *median* value is therefore taken in the frequency range of interest. Note that the *median* is taken rather than the *mean*, because it is not affected by extreme values.

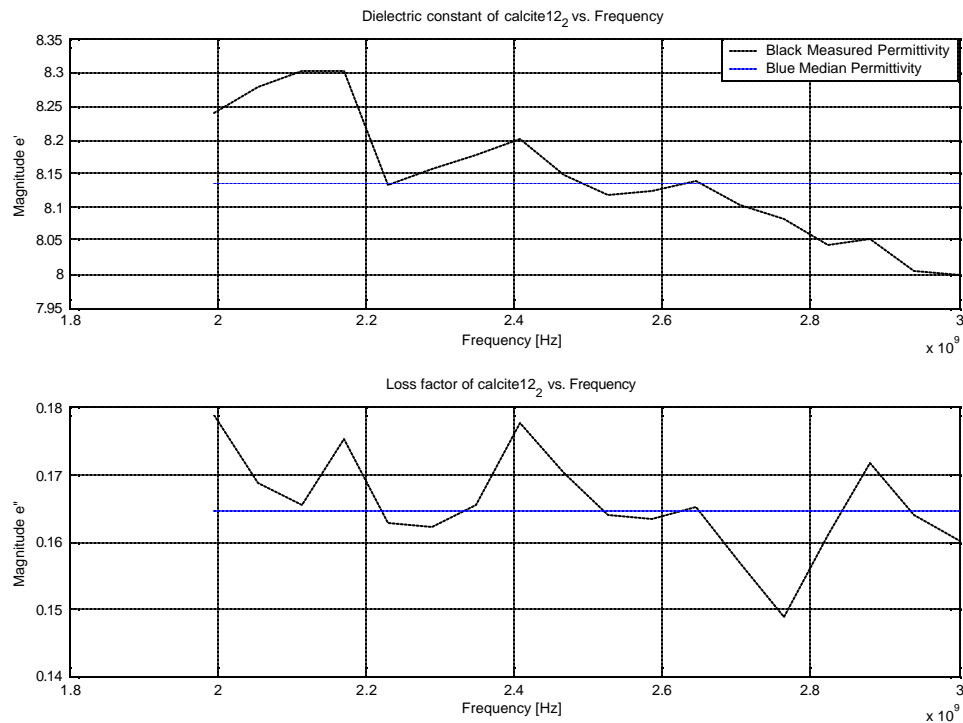
The above argument supports the fact that a *median* value of the data is taken. There is however no argument to support the *frequency ranges* for the *median*. It can be seen from Figure 4.4 that *median* values will vary greatly (from  $\epsilon'_r = 2.15$  to  $\epsilon'_r = 2.05$ ) between 2 to 3 GHz respectively, if a *median* range of 100 MHz was chosen. The good accuracy of the dielectric constant over the range of 2 to 3 GHz is therefore coincidence and permittivity values of unknown materials should in fact be read close to the frequency of interest instead of taking a *median*. To solve this problem, high quality phase stable cables should be used for materials measurement. To illustrate this, such a measurement is included in Appendix A, Figure A.5.

The boundary values of the dielectric constant are accurately determined compared to reference values (agree within 2.4%). The loss factor is out by more than two orders of magnitude. This is because of the non-perfect matched load calibration standard and our inability to model the matched load standard accurately. The results do show that PTFE and Perspex have low loss.

The small ripple present in the data is measurement noise (Section 3.3.4). The above arguments will apply to all probe results presented here and in Appendix A.

### Calcite

The calcite sample used during measurement was shown in Figure 4.2 (white sample). The fact that other phases are still present in the sample was mentioned in Section 4.3.2. Before the probe was pushed onto the sample an area was chosen that showed no visual signs of another phase. Also, a small magnet was dragged over the surface to detect any magnetic phases underneath the surface. These areas were avoided and results are presented in the figure below.



Material	$\epsilon'_r$ (Probe)	$\epsilon''_r$ (Probe)	$\epsilon'_r$ (Literature)	$\epsilon''_r$ (Literature)
Calcite	8.13	0.164	7.8 - 8.5	-

**Figure 4.5 - Dielectric constant and loss factor of calcite as measured with the coaxial probe**

Literature values are quoted from an internet source [38] for calcite at Radio frequency. Meredith [5] defines radio frequencies up to *100 MHz*.

The boundary values of the dielectric constant are accurately determined compared to reference values (are within the quoted range). No reference value for the loss factor of calcite was available but it is believed to be a relatively low loss material.

### **Magnetite**

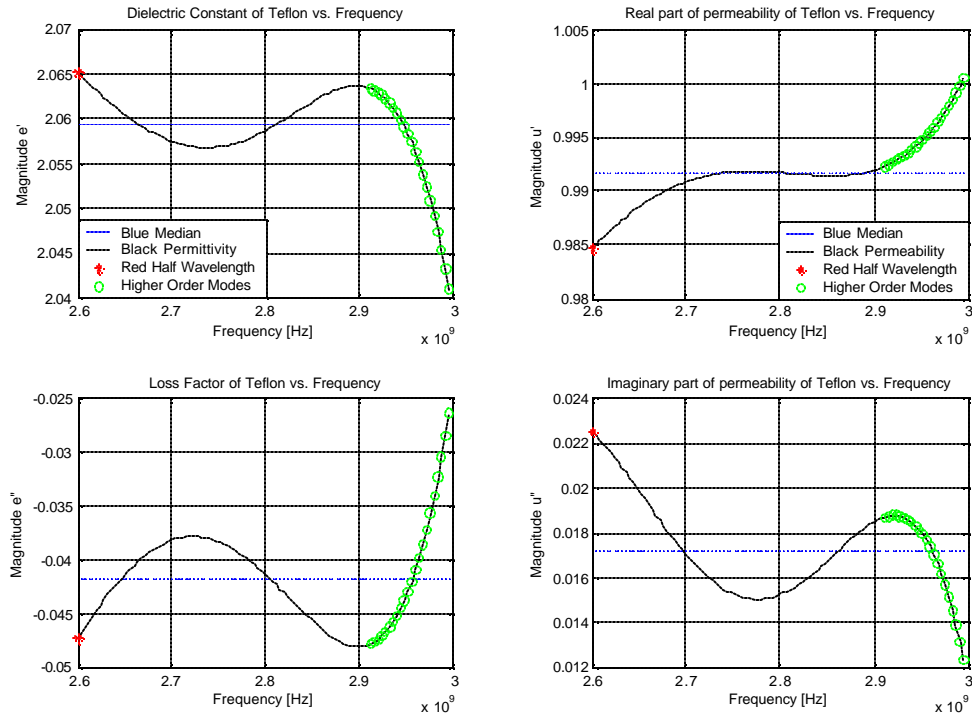
The probe was applied to the magnetite and an  $S_{11}$  similar to a short circuit was registered ( $|S_{11}| = 0dB$ ,  $\angle S_{11} = 180^\circ$ , see Appendix A). This behaviour was predicted in Section 3.3.5.

## **4.5.2 WG Measurements**

Every figure in this section presents results of both permittivity and permeability as measured with the *WG* measurement system. Again the median values over the frequency range of interest are quoted. The uncertainties discussed regarding *WG* measurements (half wavelength and higher order modes) are tested for by the inversion code. The legend on the graphs is indicative of this and is as follows:

- The solid black line represents the measured data (smoothed)
- The straight blue line is the median value taken over the desired frequency range
- The green circles (o) give a warning that the measured material properties could support higher order modes inside the sample
- The red stars (\*) are an indication that one half wavelength or an odd multiple thereof is approaching the same length as the sample material

Note that the median values (2nd bullet) are determined over the frequency range from *2.6 – 3 GHz* regardless of higher order modes or half wavelength uncertainty.

**PTFE (Teflon)**

Material	$\epsilon'_r$	$\epsilon''_r$	$\mu'_r$	$\mu''_r$	$\epsilon'_r$ (Lit)	$\epsilon''_r$ (Lit)	$\mu'_r$ (Lit)	$\mu''_r$ (Lit)
PTFE	2.06	-0.042	0.992	0.017	2.08; 2.1	0.00076; 0.0003	1; 1	0; 0

**Figure 4.6 - Dielectric and magnetic properties of PTFE as measured with the WG system**

The literature values are quoted from [20] and [4] under slightly different conditions (see Table 4.1 for detail on conditions).

The dielectric constant and the real part of permeability are in line with quoted literature values. The measured number for the real part of permeability is indicative of the level of accuracy possible with this system for this parameter. Also check results on Perspex in Appendix A. The loss factor and imaginary part of permeability were not determined accurately, but do show small values.

The negative value for the loss factor was not addressed in any of the accessed literature and will now be discussed. By definition  $\Gamma$  (3.10) and  $T$  (3.12) cannot be bigger than 1. After investigation it was found that all low loss materials (including Perspex and air) showed a small negative loss factor, and that in each case  $|T| > 1$  (figure below).

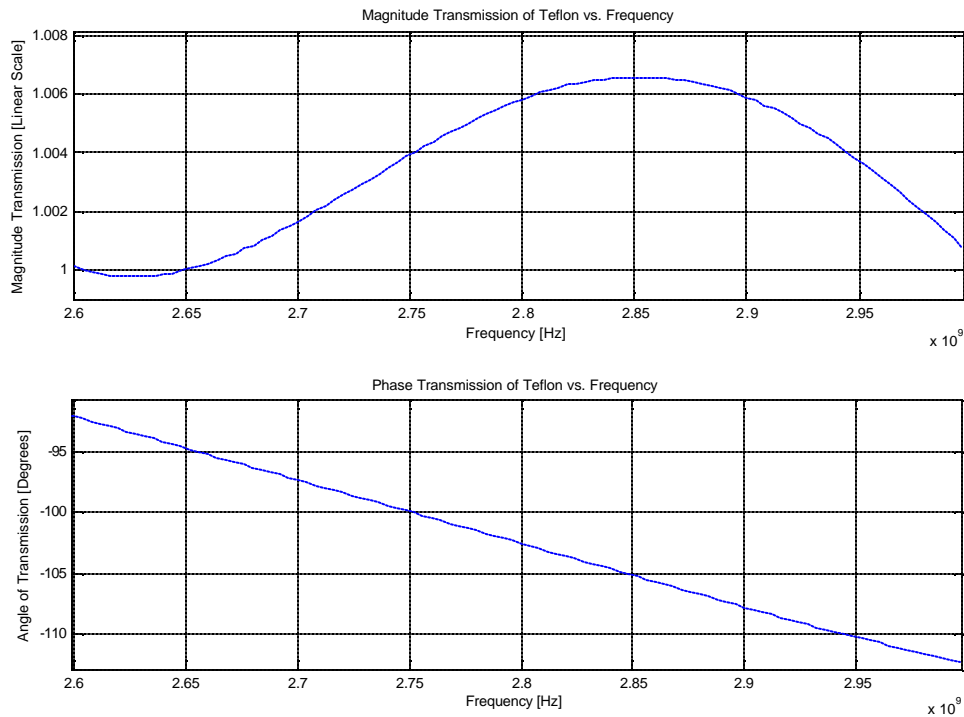


**Figure 4.7 - Magnitude and phase of the transmission coefficient**

$T$  is a function of the measured  $S$ -parameters alone (3.12). The matched load standard calibrates directivity errors but because the standard is non-ideal (i.e. induces reflections of its own), the ANA over-compensates for these errors. This results in an erroneous amplitude calibration of  $S$ -parameters and in a negative dielectric loss factor. However this does not corrupt the dielectric constant or real part of permeability as these parameters still compare well with the literature data.

The ripple present in the results should be noted is on a fine scale and is the result of the mathematical amplification of non-perfect calibration (see Section 3.4.5). Small variations in the  $S$ -parameters are accentuated by quadratic functions in (3.10), (3.11) and

(3.13). To support this, the reflection coefficient,  $\Gamma$  (which is a function of the measured S-parameters alone), for PTFE is presented in the following figure.

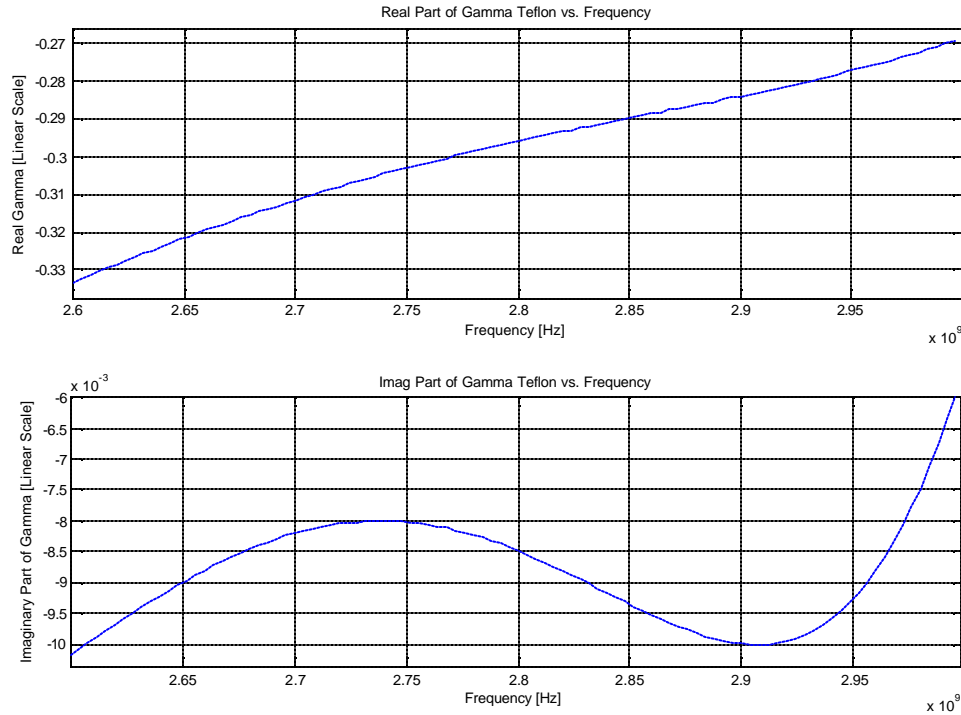


**Figure 4.8 - Reflection Coefficient of PTFE vs. frequency**

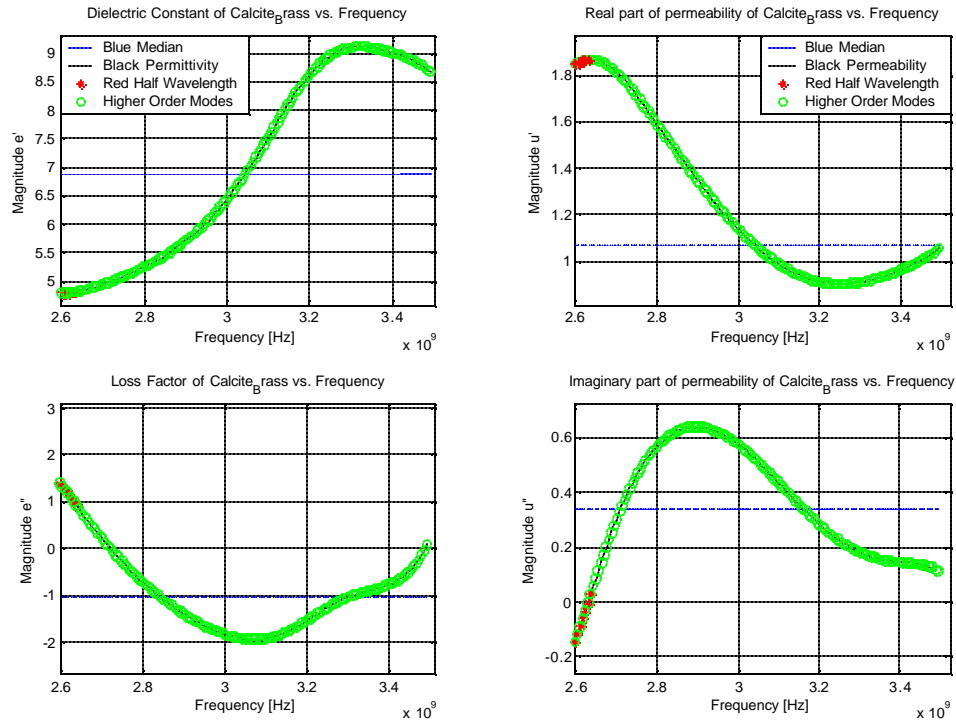
The imaginary part of the reflection coefficient, calculated from (3.10) and (3.11) clearly displays the ripple present in the material properties of PTFE (maximum and minimum at approximately  $2.74$  and  $2.91 \text{ GHz}$ ). This can be seen, using either the reflection or transmission coefficient, for all other results displaying a similar oscillatory behaviour on a fine scale. Based on the argument that imperfect calibration causes a ripple in the results due to mathematical amplification, (albeit on a small scale), the median values are taken over the desired frequency range.

The green circles indicate that higher order modes may exist at the identified frequencies. It is unlikely though, since PTFE is homogeneous, isotropic and fits tightly into the sample holder (i.e. no perturbation to induce the higher order modes).



The arguments stated above will apply to all subsequent measurements here and in Appendix A.

### Calcite



Material	$e'_r$	$e''_r$	$m'_r$	$m''_r$	$e'_r$ (Lit)	$e''_r$ (Lit)	$m'_r$ (Lit)	$m''_r$ (Lit)
Calcite	6.88	-1.052	1.06	0.34	7.8-8.5	-	1	0

**Figure 4.9 - Dielectric and magnetic properties of calcite as measured with the WG system**

Literature values quoted from an internet source [38] for calcite at Radio frequency (up to 100 MHz [5]).

The measured properties are not expected to agree perfectly with the literature values since the sample measured is not entirely homogeneous and measured over a higher frequency range.

The material properties of calcite show bigger variations than PTFE. Also the negative loss factor should be investigated in the same way as before (PTFE). After investigation of the reflection and transmission coefficient both were found to be between 0 and 1 indicating there are no calibration errors. The possibility of higher order mode excitation is investigated next.

It was shown in Section 4.3.2, Figure 4.2, that the calcite sample is not entirely homogeneous. The fact that higher order modes may exist is therefore possible. The magnitude of the  $S_{11}$ -parameter will be considered as suggested by [33] and is presented below.

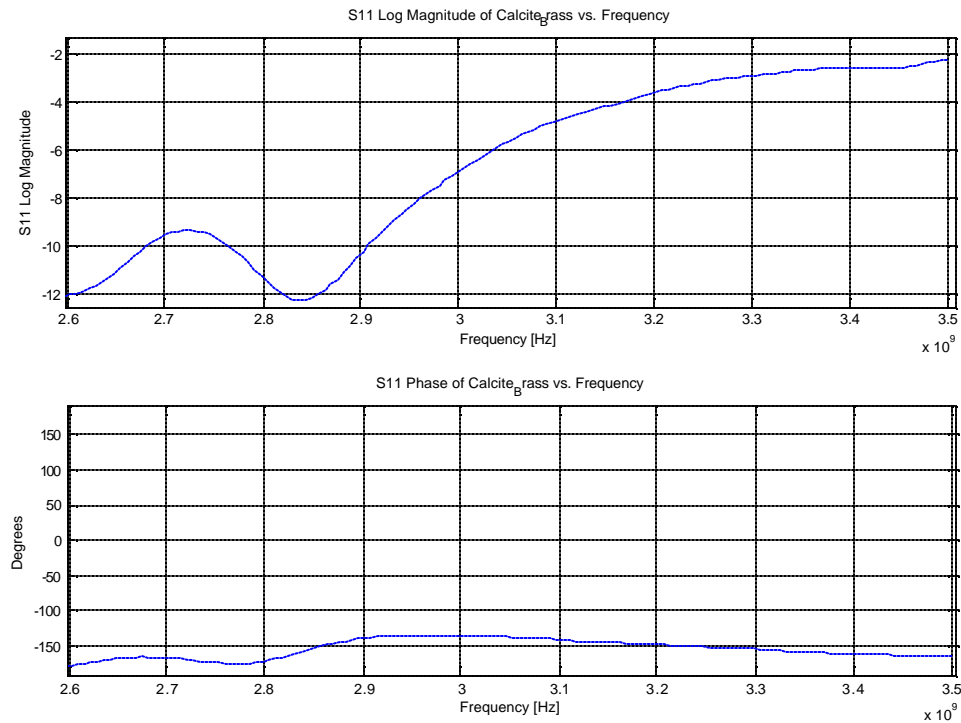


**Figure 4.10 -  $S_{11}$  of calcite**

The change in magnitude of at least 2 dB between 2.6 and 2.85 GHz and the change in the slope are an indication that higher order modes are induced [33]. This could be responsible for the erroneous loss factor (cannot be negative by definition) and the

unnaturally high imaginary part of permeability. However the median values do show realistic and comparable values for both the dielectric constant and the real part of permeability.

### **Magnetite**

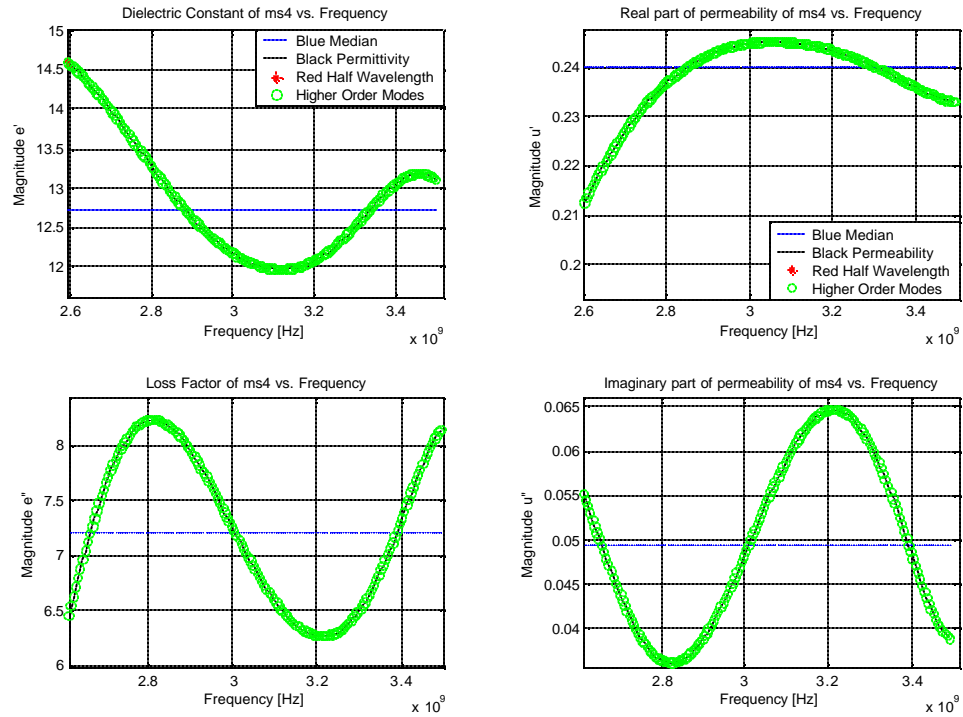
The slab of magnetite (Figure 4.2) was measured with the *WG* measurement system, but similar to the probe measurement, S-parameters characteristic of a short circuit were registered (Appendix A).

Magnetite could not be quantified with either the *WG* or the probe and literature was consulted. A value of  $\dot{m}_i = 100$  was found in [36]. After reviewing the wide range of conductivity values quoted by [37] and of semi-conductor materials [13] a value of  $s_e = 100$  was chosen for magnetite.

## ***4.6 Measurement of Inhomogeneous Materials***

A slab of carbonatite (Figure 4.1) and crushed carbonatite ore (Figure 4.3) were measured in the *WG* measurement system. Median values in the frequency range of interest are presented below every figure. The legend on graphs is as previously discussed in Section 4.5.2.

### Carbonatite



Material	$e'_r$	$e''_r$	$m'_r$	$m''_r$	$e'_r$ (Lit)	$e''_r$ (Lit)	$m'_r$ (Lit)	$m''_r$ (Lit)
Carbonatite	12.72	7.21	0.24	0.0493	-	-	-	-

Figure 4.11 - Dielectric and magnetic properties of carbonatite as measured with the WG system

There was no reference available for a bulk material property of carbonatite in the accessed literature.

The loss factor shows a positive number and both the reflection and transmission coefficients are between 0 and 1, indicating a credible S-parameter measurement. Higher order modes may have been induced because the carbonatite sample is an inhomogeneous anisotropic material. The  $S_{11}$ -parameter of the carbonatite sample is examined and presented in the following figure.

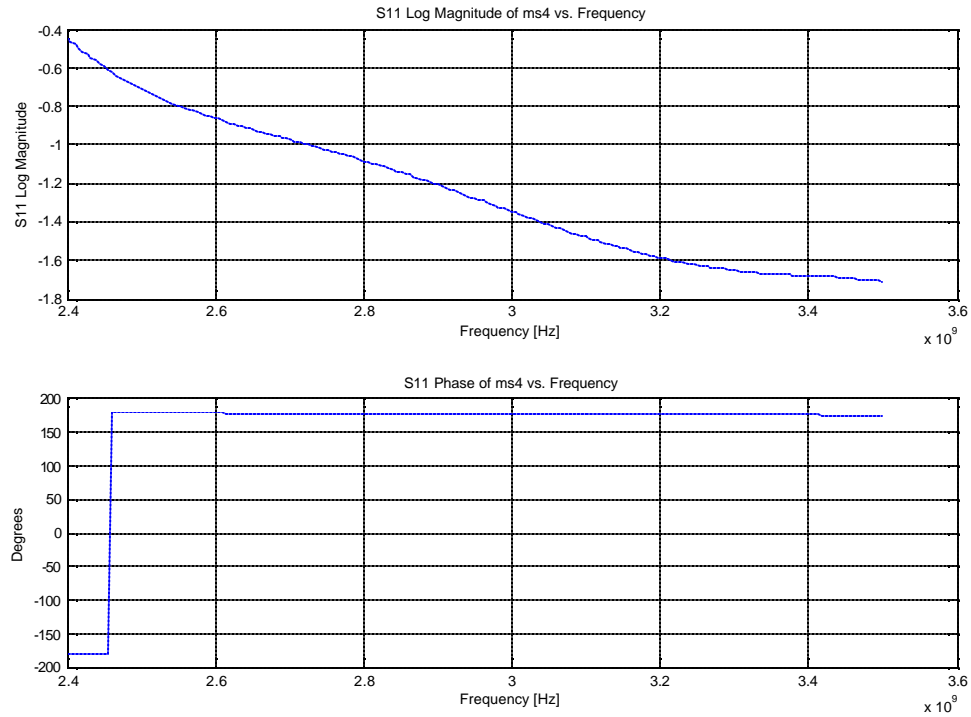


**Figure 4.12 -  $S_{11}$  of the carbonatite sample**

The  $S_{11}$  magnitude does not show significant irregularities indicating higher order mode excitation is improbable. The measured parameters therefore appear to be compelling quantities.

An interesting observation is the small number quoted for the real part of the permeability ( $\mu' = 0.24$ ). Materials with a  $\mu' < 1$  are known as diamagnetic materials and have the physical property of opposing magnetic field induction. Naturally occurring diamagnetic elements, (e.g. copper, mercury, [36]), however show a  $\mu'$  smaller than 1 in the order of  $10^{-5}$ . Haus and Melcher [36] showed in an experiment the design of an artificial diamagnetic material. This artificial material consisted of a solenoid filled with an array of metal spheres and is presented in the following figure.

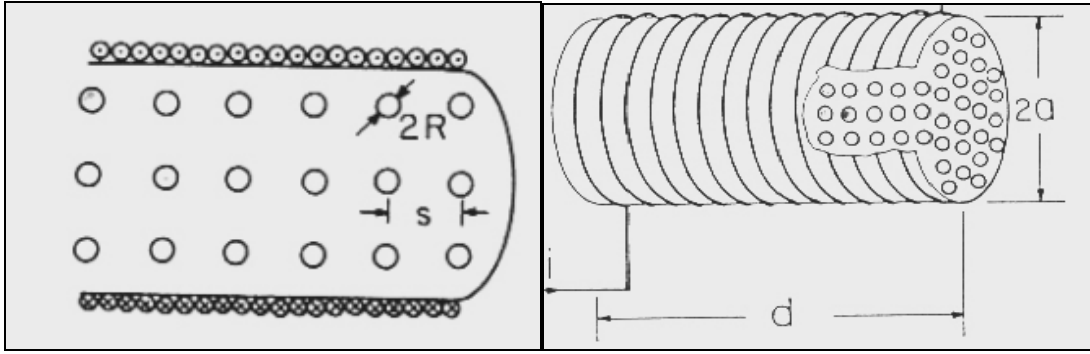


Figure 4.13 - Artificial diamagnetic material, (after Haus and Melcher [36])

Where:

- $R$  is the radius of the metal sphere
- $s$  is the distance between the centre of two spheres
- $d$  is the length of the solenoid
- $a$  is the radius of the solenoid

Haus and Melcher [36] then formulated an expression for  $\mathbf{m}_r'$  which is presented below:

$$\mathbf{m}_r' = (1 + \mathbf{c}_m) = 1 - 2p \left( \frac{R}{s} \right)^3 \quad (4.1)$$

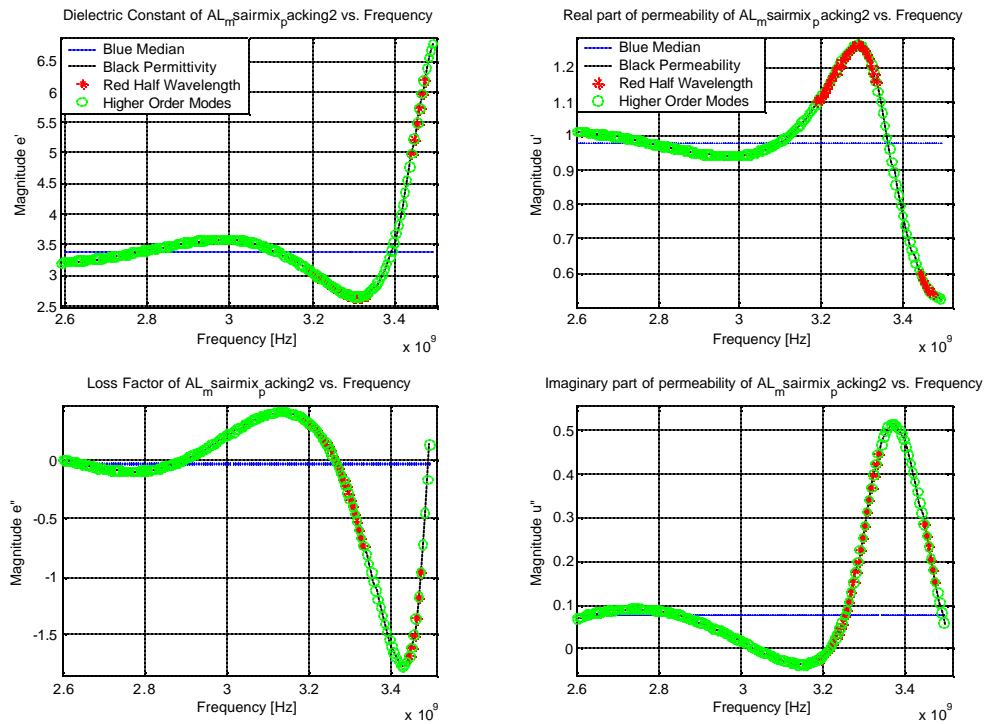
Where:

- $\mathbf{c}_m$  is the magnetic susceptibility

Relating a similar model to the carbonatite, but with the metal balls (or conductive phase-particles) touching one another, and using (4.1),  $\mathbf{m}_r'$  calculates to 0.215. This is close to the measured 0.24 of carbonatite. This suggestion of an artificial diamagnetic effect, created by the carbonatite ore, is entirely hypothetical. Further experiments should be conducted to support or discard this argument.

### Rock Air Mixture

The crushed ore is a variable, anisotropic load and the following figure shows one set of material property results. Refer to Table A.1 in Appendix A for more results.



Material	$\epsilon_r'$	$\epsilon_r''$	$\mu_r'$	$\mu_r''$	$\epsilon_r'$ (Lit)	$\epsilon_r''$ (Lit)	$\mu_r'$ (Lit)	$\mu_r''$ (Lit)
Rock/Air Mix	3.37	-0.025	0.98	0.077	-	-	-	-

**Figure 4.14 - Dielectric and magnetic properties of crushed ore as measured with the WG system**

Again there was no reference available for a bulk material property of crushed carbonatite in the accessed literature.

The dielectric constant and real part of permeability are reliable up to 3.2 GHz. The loss factor does show a small number but cannot be negative by definition. The imaginary part of permeability also shows a small number. See Table A.1 in Appendix A for more results on crushed ore.

Both the reflection and transmission coefficients are smaller than 1 and bigger than 0, indicating a credible S-parameter measurement.

At 3.2 GHz, the inversion code indicates that the wavelength approaches twice the sample length (half-wavelength error). This is an area of high uncertainty in the measured material properties [22].

Higher order mode excitation is investigated next. The following figure presents the  $S_{11}$  parameter of the rock/air mixture.

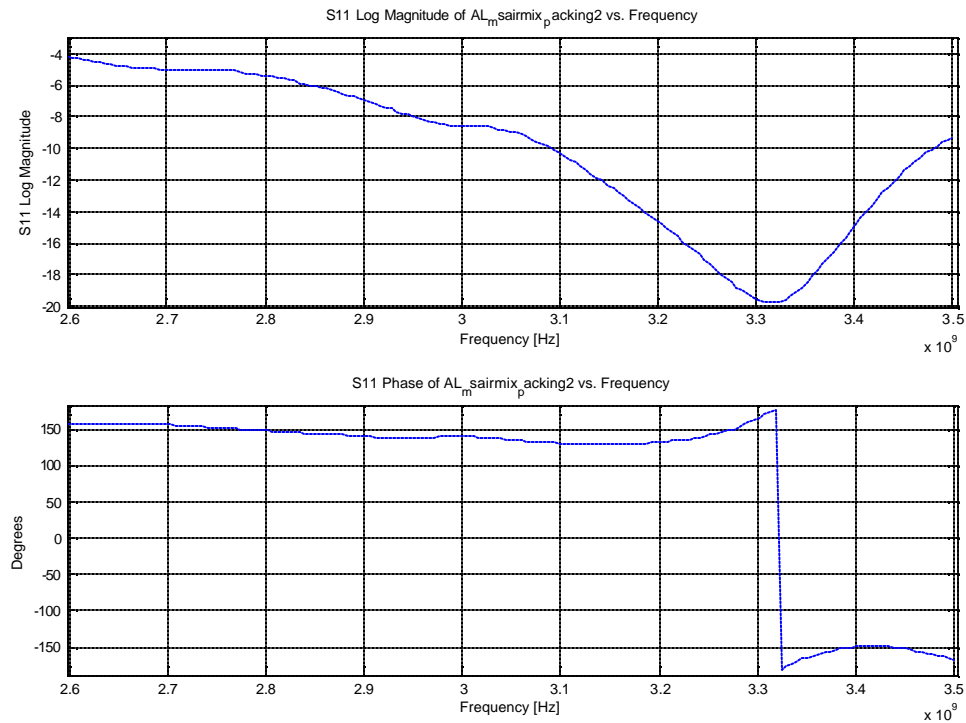


**Figure 4.15 -  $S_{11}$ -Parameter of rocks packed inside SH2**

From the figure above, the dip and subsequent change in gradient at 3.3 GHz in the magnitude of  $S_{11}$  is indicative that a higher order mode might have been induced.

The combination of the half-wavelength error and probable higher order mode excitation could be responsible for the negative loss factor.



## 4.7 Summary of Results

The following table shows all results from above and Appendix A for both literature and the probe and WG measurement systems.

**Table 4.3 - Comparison of material properties measured with the probe, WG and literature**

<u>Materials</u>	<u>Probe</u>				<u>WG</u>				<u>Literature</u>			
<u>Homogeneous</u>	$\epsilon_r'$	$\epsilon_r''$	$m_r'$	$m_r''$	$\epsilon_r'$	$\epsilon_r''$	$m_r'$	$m_r''$	$\epsilon_r'$	$\epsilon_r''$	$m_r'$	$m_r''$
PTFE (Teflon)	2.09	0.098	X	X	2.06	-0.04	0.99	0.017	2.1	0.0003	1	0
Perspex	2.57	0.025	X	X	2.62	-0.07	0.99	0.026	2.6	0.015	1	0
Carbon Foam	2.33	0.67	X	X	2.15	0.473	0.99	0.022	X	X	X	X
Calcite	8.13	0.165	X	X	6.88	-1.05	1.06	0.34	6.4-9.1	0	1	0
Magnetite	X	X	X	X	X	X	X	X	X	X	100	X
<u>Inhomogeneous</u>												
Carbonatite	X	X	X	X	12.72	7.21	0.24	0.0493	X	X	X	X
Crushed Ore	X	X	X	X	3.37	-0.03	0.98	0.077	X	X	X	X

The X indicates that no data is available.

## 4.8 Conclusion

Both homogeneous and inhomogeneous materials were introduced. A copper carbonatite sample was measured with the WG system as a solid and crushed ore. Its two dominant phases, calcite and magnetite, were measured with both the probe and WG systems. Teflon was used as a reference material and results for the dielectric constant are accurate. Next, conclusions will be made on measurements done by the individual measurement systems.

**Probe Measurement:**

In tandem with the remarks of Section 3.3.5 the following conclusions can be advanced *after* measurements were made:

- The probe matched load calibration standard is a weakness in determining the loss factor
- The measurements are sensitive to phase stability and temperature drift
- The accuracy is hampered due to lift off between the probe face and the *MUT*
- The probe cannot measure low loss factors
- It was confirmed that the probe cannot measure conductive materials
- Interrogation of location specific areas proved an advantage as individual phases within an ore could be interrogated

**WG Measurement of Homogeneous and Inhomogeneous Materials:**

The oscillatory behaviour in the measured material properties is not a real characteristic of the material (the probe does not show a similar behaviour), but rather a measurement anomaly. It should be investigated if this is due to higher order modes generated at the air/material interface (on the calibration plane, see Figure 3.9). This research could be done by inserting lengths of *WG* at both ends after calibration, electrically rotating the calibration planes to the face of the sample and measuring S-parameters. The loss of the *WG* inserted should also be measured and compensated for. This ensures that any higher order mode generation due to discontinuities at the calibration plane will not affect measured data.

In subsequent work it has been noted that mechanical alignment of the SH could be responsible for this behaviour as an empty sample holder (air measurement; refer to figure A.6) reveals the same response, albeit on a very small scale.

In tandem with the remarks of Section 3.4.7 the following conclusions can be advanced *after* measurements were made:

### **Homogeneous Materials**

- Both  $\epsilon_r'$  and  $\mu_r'$  can be measured accurately if the sample is well prepared and the median is taken
- Neither  $\epsilon_r''$  nor  $\mu_r''$  can be measured for low loss materials
- From Table 4.3 it must be noted that the probe differs from the *WG* results for carbon foam by approximately 9% for the dielectric constant and 42% for the loss factor. This might be because the probe was pushed onto the carbon foam, compressing its immediate surroundings, and resulting in the interrogation of a denser environment
- It is unlikely that higher order modes are induced in homogeneous samples. It might happen if there is a notable gap between the sample and *SH*
- It was confirmed that the *WG* cannot measure conductive materials
- The *WG* cannot measure low loss factors

### **Inhomogeneous Materials**

- Inhomogeneous materials might induce higher order modes. Whether this corrupts the measurement or not was not proven. Measured data should be checked against literature values if available or relevant simulations should be done to support or discard the properties. In general though, it appears that results for both  $\epsilon_r'$  and  $\mu_r'$  (arguably) can be trusted if the median value is taken

The next chapter will present electromagnetic simulations of two different loaded microwave cavities and compare results to experimental data as a verification of material properties.

## Chapter 5

# Verification of Material Properties by FDTD Simulation

---

### 5.1 Introduction

In this chapter the measured material properties will be employed by computational electromagnetic (*CEM*) software as a verification technique of quantified samples. The approach used will be to compare measured and simulated S-parameters of both the *WG* measurement system *and* a single mode applicator. Figure 5.1 gives a graphical representation of this idea.

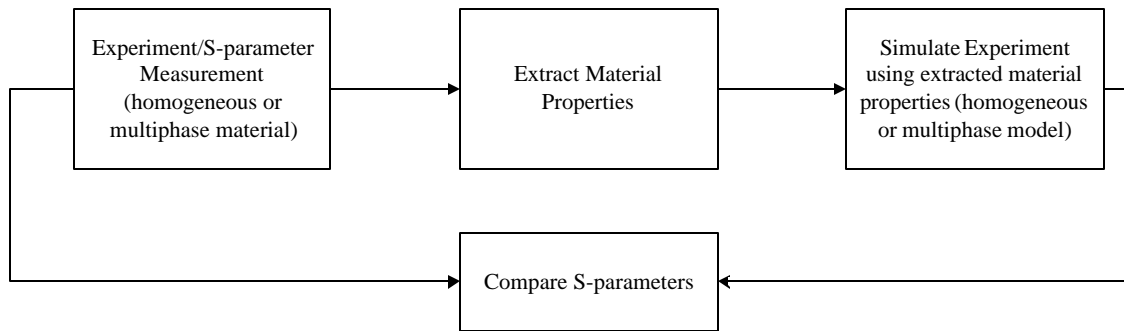


**Figure 5.1 – Diagrammatic representation of the experimental/simulation comparison technique**

The chapter starts with a discussion on the significance and limitations of comparison on the basis of S-parameters in Section 5.2. Simulated multiphase materials can be represented by different models and are introduced in Section 5.3. This is followed by a brief discussion of the computational software utilised (Section 5.4). Sections 5.5 and 5.6 present results of the measured S-parameters of the *WG* sample holder and a single mode cavity respectively, in comparison to simulated S-parameters. In Section 5.7 conclusions are made.

## 5.2 S-Parameter Comparison

For multiphase materials, an S-Parameter comparison of measured and simulated results can be seen as a ‘*black box*’ approach, where the *black box* is a combination of material geometry and composition. The block in Figure 5.2 represents any loaded microwave cavity (experimental or simulated) and its interaction with incident microwaves.

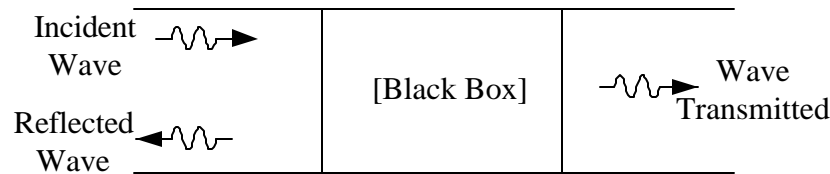
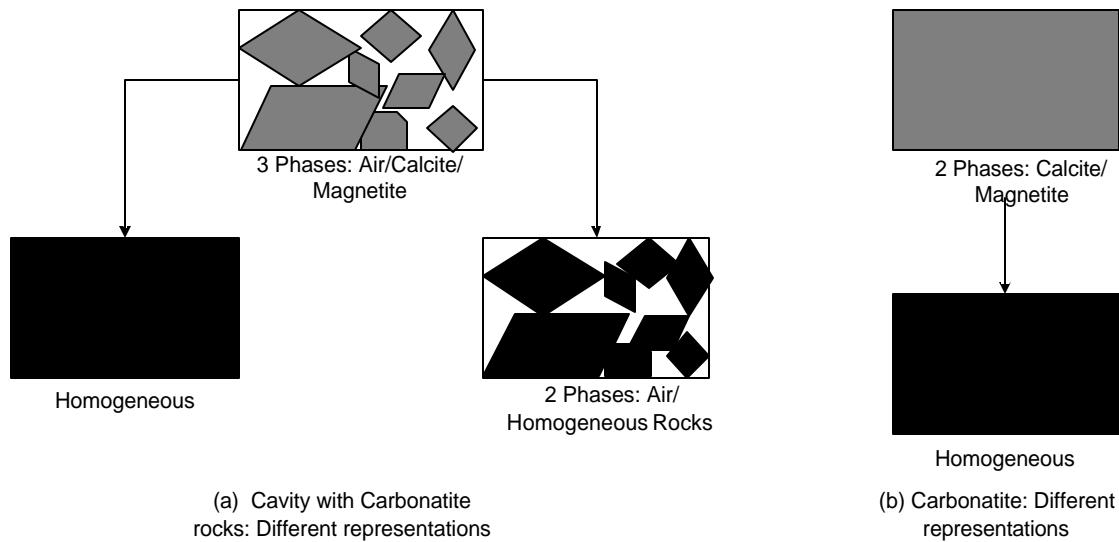


Figure 5.2 - “Black box” approach and flow of waves in a general 2 port system

The two port *WG* S-parameter measurement of a *MUT* is related to waves reflected, absorbed and transmitted. However, it contains no information about the material geometry and composition. The S-parameters of various geometries and compositions can therefore be the same. This is a limitation of S-parameter comparison. An accurate multiphase model must be verified by comparison of measured and simulated field distributions and not S-parameters alone. Refer to Pozar [12] for more detailed information of S-parameters if sought.

## 5.3 Simulation Models

In general, simulation models of loaded microwave cavities require a model of both the cavity and the load. The cavities used here are simple enough to model accurately and simplify the problem to one of creating an accurate representation of the load. The two variables when creating a load are the load geometry and its material properties. A homogeneous load with a regular geometrical shape (rectangular, cylindrical, etc.) is easy to model. However, a multiphase load can be modelled as a homogeneous material or as a multiphase material, each having its own advantages and disadvantages. Different load representations are presented in the following figure.



**Figure 5.3 - Different simulation models of a multiphase material**

### **Homogeneous Model**

In Figure 5.3(a) the homogeneous model gives a bulk effective representation combining geometrical effects and material properties of each phase. This model blends geometry into the material properties and eliminates the task of accurate representation of the geometry. The homogeneous model is easy to create and could simplify *MW* cavity design. However no information is available about electromagnetic field stress in and between different phases.

### **Two Phase Model**

The two phase model combines the carbonatite phases into a homogeneous material but keeps the carbonatite and air as separate entities. It blends geometrical effects of different rock phases within the carbonatite into the homogeneous rock properties. The model depends on bulk material properties *and* the geometry of the rocks inside the air filled cavity. The geometry is more difficult to model than the homogeneous representation. Again no information is available about electromagnetic field stress in and between different rock phases.

### **Three Phase Model**

The three phase model keeps geometry and material properties independent from one another. This model needs an accurate description of material properties and the load geometry. It will provide information about field stress in and between different phases. This information could be utilised in thermal stress modelling and is thus crucial in the detail design of a *MW* applicator.

In Figure 5.3(b) a similar approach is used for the solid carbonatite ore.

## **5.4 Introduction to Computational Electromagnetics (CEM)**

The heart of electromagnetic computation is Maxwell's equations. In differential form they are written according to Pozar [12] as:

$$\nabla \times \overline{H} = j\omega \epsilon' \overline{E} + (\omega \epsilon'' + \sigma) \overline{E} \quad (5.1)$$

$$\nabla \times \overline{E} = -j\omega \mu' \overline{H} - (\omega \mu'' + \overline{M}) \quad (5.2)$$

$$\nabla \cdot \overline{D} = \rho \quad (5.3)$$

$$\nabla \cdot \overline{B} = 0 \quad (5.4)$$

The simplified constitutive relations are:

$$\overline{D} = \epsilon \overline{E} \quad (5.5)$$

$$\overline{B} = \mu \overline{H} \quad (5.6)$$

The analytical solution to Maxwell's equations becomes complex for realistic problems and certain approximations can be made. The numerical approximation of Maxwell's

equations is known as computational electromagnetics (*CEM*) [39]. According to Davidson [39], the case where no initial physical approximations are made is known as full wave *CEM*. The three most widely used full wave solutions are the finite difference time domain (*FDTD*) method, the method of moments (*MoM*) and the finite element method (*FEM*).

The numerical code used in this thesis is called Concerto<sup>®</sup> and is marketed by Vector Fields<sup>®</sup>. This code implements the *FDTD* numerical method. There are several advantages and disadvantages to the *FDTD* method [39], but significant to this project are the following advantages: wideband data is available from one simulation and inhomogeneous materials can be treated relatively easily. A possible limitation is frequency independent parameters. For a comprehensive account of the *FDTD* method, refer to Taflove and Hagness [40].

#### 5.4.1 FDTD Concerto<sup>®</sup> from Vector Fields<sup>®</sup>

Figure 5.4 presents a flow diagram of the seven steps involved in running a simulation utilising Concerto<sup>®</sup>.



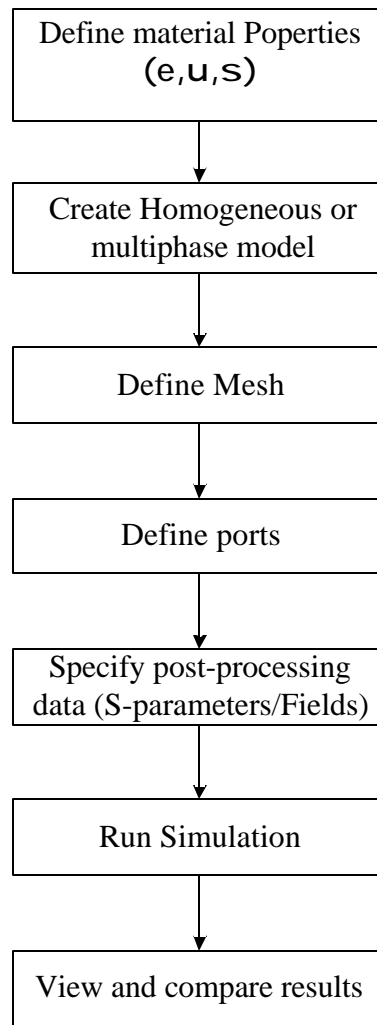


**Figure 5.4 - Seven steps when setting up a simulation in Concerto®**

Each step will now be discussed briefly.

#### **5.4.1.1 Define Material Properties**

Figure 5.5 presents the materials definition dialog box in Concerto®. The material properties required are permittivity, permeability and conductivity. Non-conductive materials are specified to have volumetric losses.

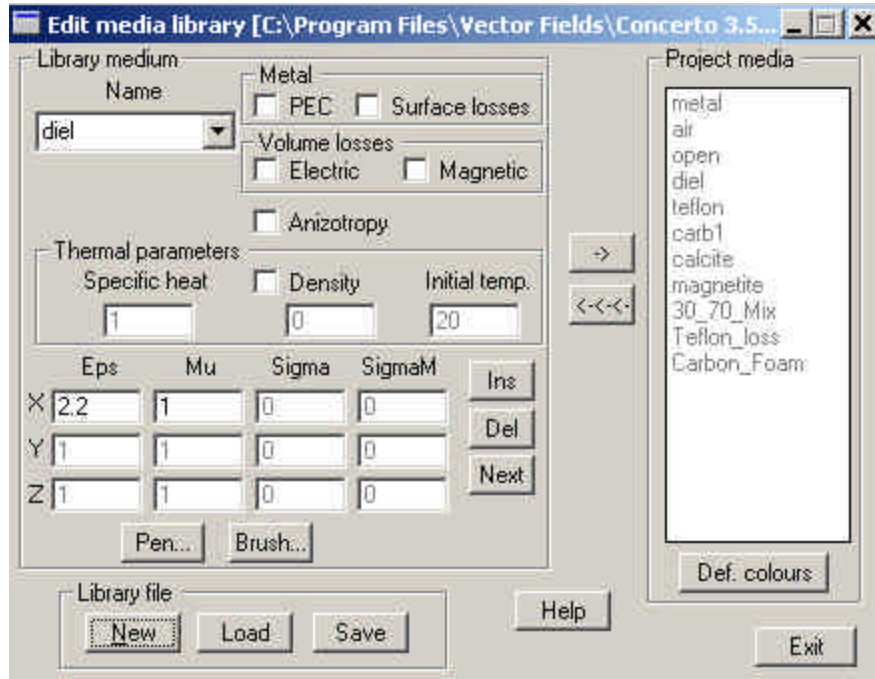


Figure 5.5 - The definition of materials dialog in the Concerto® environment

Concerto® accounts for the loss factor of permittivity as part of the dielectric conductivity,  $s_d$  (*Sigma* in Concerto®). Now (2.13) can be expanded and expressed as follows:

$$Sigma = s_d = 2p f_0 \mathbf{e}_0 \mathbf{e}_r'' \text{ [S/m]} \quad (5.7)$$

Concerto® defines a magnetic conductivity factor (*SigmaM*) to account for any magnetic losses in a material. The unit is *O/m* and *SigmaM* is defined as follows [41]:

$$SigmaM = \frac{2p f_0 \mathbf{m}_0 \mathbf{m}_r''}{(120p)^2} \text{ [O/m]} \quad (5.8)$$

In both (5.7) and (5.8)  $f_0$  is the centre frequency of the simulation. All the other parameters have been defined previously. It is important to note that Concerto® assumes  $s_d$  and *SigmaM* are constant parameters. This implies that,  $s$  and *SigmaM* are independent of change in frequency and permittivity and permeability respectively. This is a limitation

in the model and the user should be aware of this assumption. This assumption further justifies the median values taken for material properties measurement in Sections 4.5 and 4.6.

When working with a conductive material, surface losses are specified instead of volumetric losses. The user then needs to provide data for  $\underline{m}_r$  and  $s_e$ . For a comprehensive discussion of the materials parameter dialog box refer to [41].

### 5.4.1.2 Creating the Simulation Model

Creating the different simulation models (Figure 5.3) for both the *WG* sample holder and the single mode cavity are discussed in Sections 5.5 and 5.6 respectively.

### 5.4.1.3 Defining the Mesh

Meshing is also known as discretization and is defined as the sub-division of a structure into a number of unit cells. In Concerto<sup>®</sup> a Cartesian coordinate system was used and geometries were meshed into rectangular unit cells. In general, greater accuracy can be achieved by making the mesh finer.

As a rule of thumb, the size of the mesh must be *10 cells per wavelength per dimension*, i.e. *1000 cells per cubic wavelength* for a volumetric geometry [39]. It is worth noting here that, although not formally reported in this thesis, various mesh sizes were used to investigate “numerical noise” to the size of the mesh. In general, the cell size utilised throughout this thesis was smaller than a 20<sup>th</sup> of the free space wavelength.

To help refine the mesh around sensitive areas (e.g. around the load) Concerto<sup>®</sup> allows for the definition of special planes or boundaries. These special planes can enforce a certain cell size on both sides of the plane. This idea is illustrated in Figure 5.6.

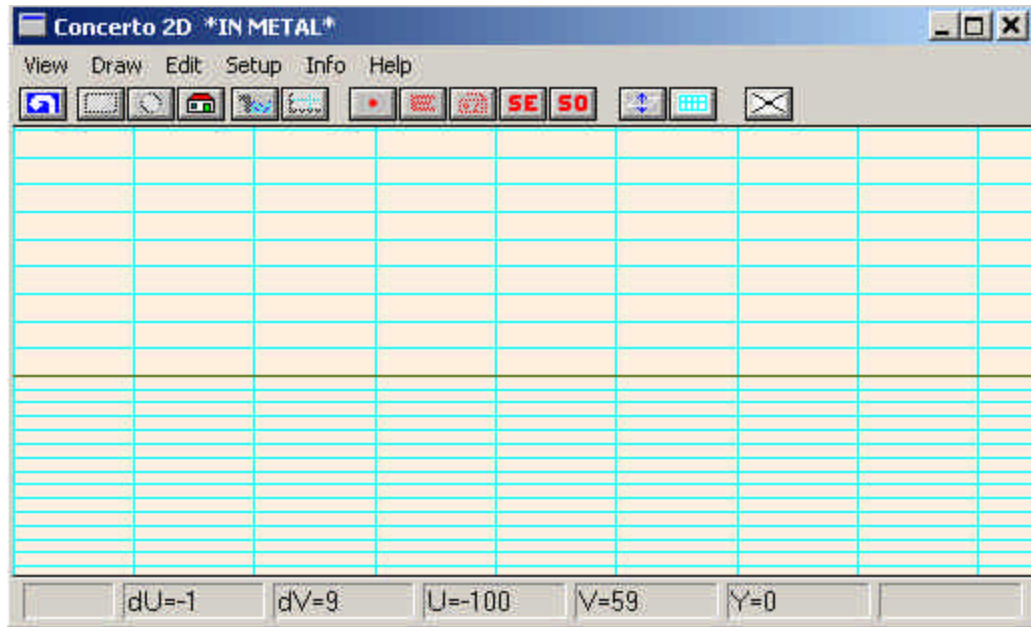


**Figure 5.6 - A special plane in Concerto (black line) forces different cell sizes above and below itself**

Meshing approximates a structure and can introduce an error known as a “discretization error”. This error is well known to produce a frequency shift of a few percent in the results [42].

#### 5.4.1.4 Port Definition

Each cavity simulated used a rectangular  $WG$  feed supporting the  $TE_{10}$  mode. The  $I/O$  port dimensions must correspond to the size of the  $WG$  feed. Each port has a reference plane associated with it. The reference plane must be spaced at least five cells away from the port itself to prevent higher order mode interference with S-parameter extraction [41]. Figure 5.7 shows the  $I/O$  ports parameter dialog box in Concerto<sup>®</sup>. The user specifies the exciting field ( $TE_{10}$  in this instance), frequency range (must be within the range supporting only  $TE_{10}$ ), a template matching frequency and search range. The template matching frequency is the centre frequency of the specified range. This is the same frequency ( $f_0$ ) that was used when specifying material properties in Section 5.4.1.1.

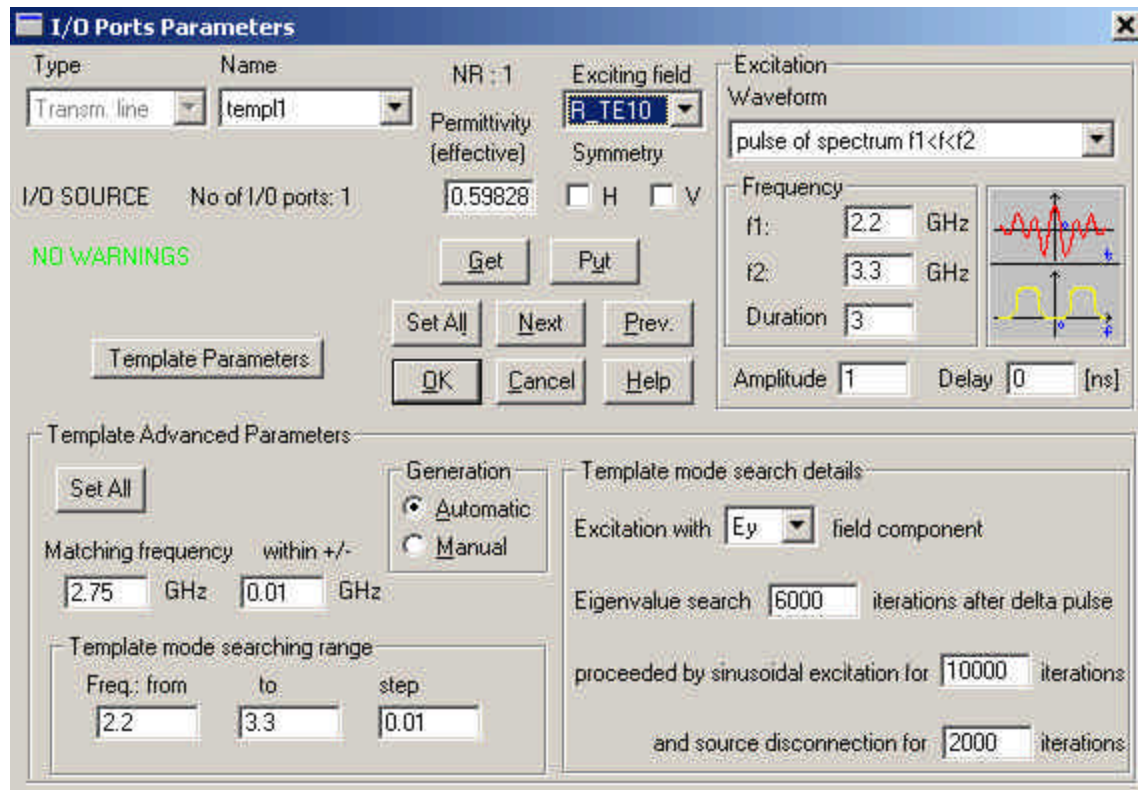


Figure 5.7 - I/O Ports parameter dialogue box in Concerto®

The effective permittivity (the permittivity inside the *WG*) is a function of the matching frequency. Again Concerto® assumes the effective permittivity to be frequency independent. Important to note is that effective permittivity is calculated for a previously set matching frequency. Thus if the matching frequency is subsequently changed, the effective permittivity is not automatically recalculated. The simplest way to recalculate it is to re-select the desired mode [41].

#### 5.4.1.5 Post-Processing Data, Run Simulation and View Results

S-parameter data was extracted by specifying the range of frequencies and the frequency step between start and stop frequencies (frequency resolution). The frequency range for S-parameter extraction must be within the excitation frequency range.

When field plots are of interest, a single frequency of excitation must be specified and the relevant plots can be viewed in the simulator. It is not necessary to specify any post-processing data to view fields during simulation. After the model was built and the parameters specified, the simulation was run and results viewed and compared to experimental data.

## 5.5 Comparison of WG SH Measurement and Simulation

The measurement setup of Section 3.4.2, Figure 3.9, was simulated utilising the extracted material properties obtained from the experiments. The simulation S-parameters were then compared to the measured S-parameters. The dimensions of both the sample holders are  $(72 \times 34 \times 20 \text{ and } 25) \text{ mm}$  and the simulation model is presented in Figure 5.8.

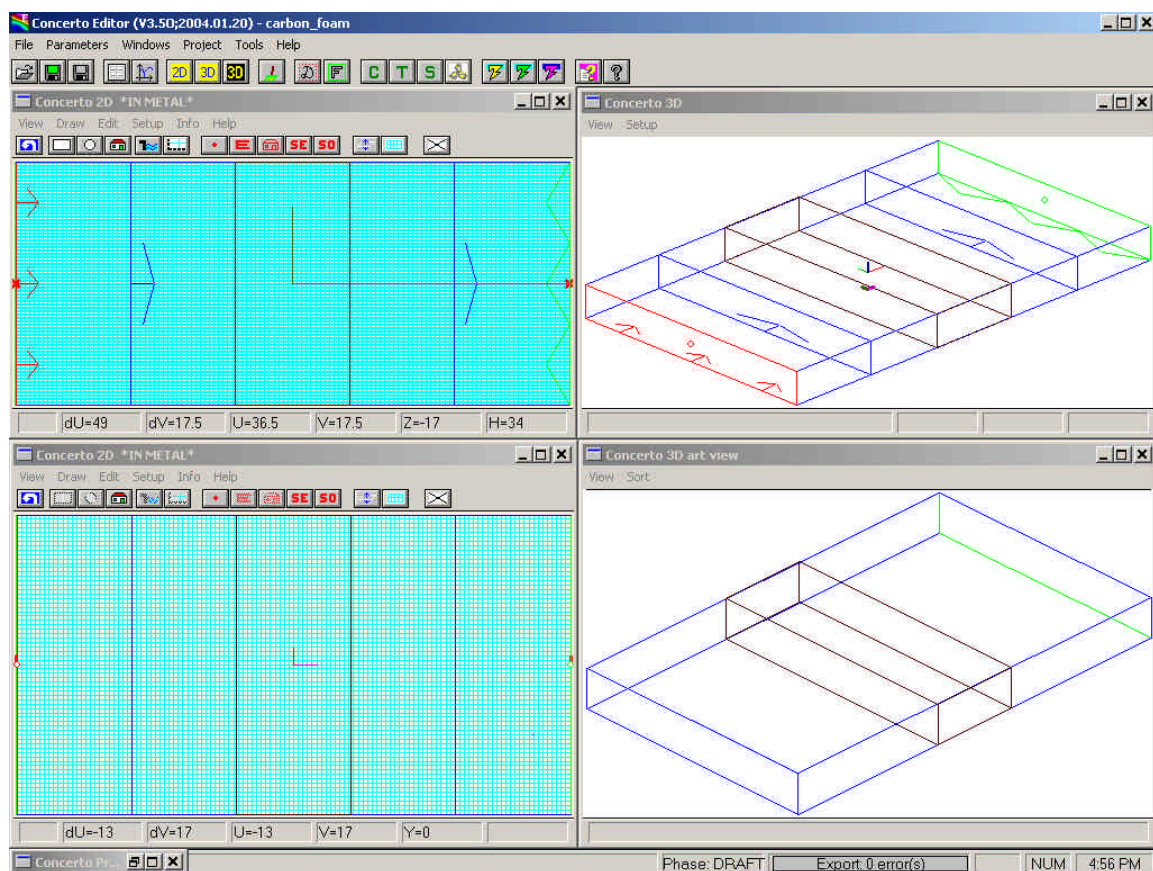


Figure 5.8 - WG simulation model with reference planes at both sides of the sample

Figure 5.8 represents the *WG SH* with a homogeneous sample. Reference planes on both sides of the sample were defined in order to extract both  $S_{11}$  and  $S_{21}$ . The excitation port is to the left of the sample in the figure above. A port with an absorbing boundary was defined on the right hand side of the sample.

Table 5.1 gives a summary of comparisons that will be made in agreement with Figure 5.3 and material properties that were used by simulation.

**Table 5.1 - Table showing the different materials' simulation models and their properties**

<b>Experiment vs.</b>	<b>Simulation model</b>					
Slab carbon foam (Homogeneous sample)	<b>(I) Homogeneous</b>					
	<b>Material</b>	$\epsilon'_r$	$\epsilon''_r$	$m'_r$	$m''_r$	<b>Source of Material Properties (Experiment/Edited/Literature)</b>
	Carbon Foam	2.15	0.473	1	0	Experiment; Appendix A
Slab of carbonatite ore (Two phase sample)	<b>(I) Homogeneous</b>					
	<b>Material</b>	$\epsilon'_r$	$\epsilon''_r$	$m'_r$	$m''_r$	<b>Source of Material Properties (Experiment/Edited/Literature)</b>
	Carbonatite	12.72	7.21	0.24	0.0493	Experiment; Section 4.6
	<b>(II) Two phase</b>					
	<b>Material</b>	$\epsilon'_r$	$\epsilon''_r$	$m'_r$	$m''_r$	<b>Source of Material Properties (Experiment/Edited/Literature)</b>
	Calcite	6	0.012	1	0	Edited; Section 4.5.2
	Magnetite	-	-	100	$s_e=100$	Literature; [36] and [37]
Crushed carbonatite ore in cavity (Three phase sample)	<b>(I) Homogeneous</b>					
	<b>Material</b>	$\epsilon'_r$	$\epsilon''_r$	$m'_r$	$m''_r$	<b>Source of Material Properties (Experiment/Edited/Literature)</b>
	Bulk Ore	3.5	0.35	1	0	Edited; Section 4.6
	<b>(II) Two phase</b>					
	<b>Material</b>	$\epsilon'_r$	$\epsilon''_r$	$m'_r$	$m''_r$	<b>Source of Material Properties (Experiment/Edited/Literature)</b>
	Carbonatite	12.72	7.21	0.24	0.0493	Experiment; Section 4.6
	Air	1	0	1	0	Experiment; Appendix A
	<b>(III) Three phase</b>					
	<b>Material</b>	$\epsilon'_r$	$\epsilon''_r$	$m'_r$	$m''_r$	<b>Source of Material Properties (Experiment/Edited/Literature)</b>
	Calcite	6	0.012	1	0	Edited; Section 4.5.2
	Magnetite	-	-	100	$s_e=100$	Literature; [36] and [37]
	Air	1	0	1	0	Experiment (Appendix A)



The column for each material displaying “*Experiment/Edited/Literature*” gives an indication of the data used. “*Experiment*” is indicative that raw experimental data were used for the material properties. “*Edited*” is indicative that some alterations were made to the experimental data. The alterations of data were made either after values in the literature were consulted or in accordance with results from various experiments and iterative simulations. “*Literature*” is indicative that the data is independent of any measurements made and based on values in literature alone.

Each of the simulation-experimental comparisons will be followed by a table showing the *average* and *maximum* percentage errors of the simulation compared to the measurement. The average error was determined by taking the difference between measured and simulated results at every frequency point. The percentage error for every frequency point was then calculated relative to the measured results and the mean value was recorded. This was implemented in a Matlab<sup>®</sup> routine and can be found in Appendix D. This applies to all subsequent comparisons. In all instances the average error is expected to be more representative of the comparison.

### 5.5.1 Carbon Foam: Homogeneous Sample vs. Homogeneous Model

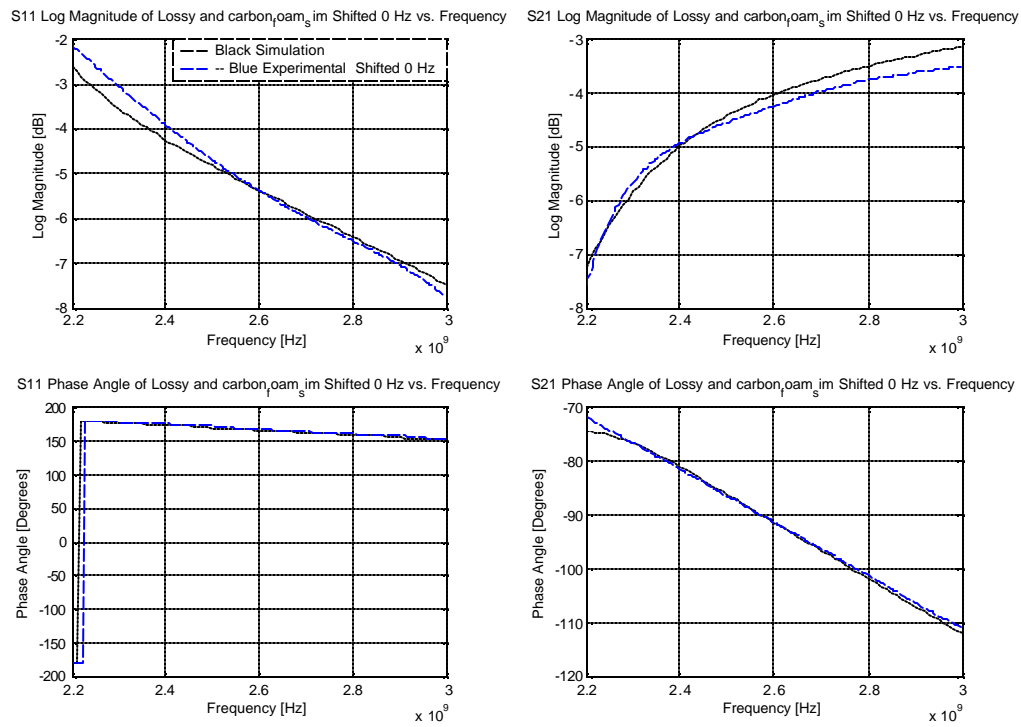
#### Load Geometry

Figure 5.8 shows the simulation model of carbon foam. The load-model takes on the same geometry as the physical sample of carbon foam ( $72 \times 34 \times 25$ ) mm. The carbon foam material was easy to cut and fits tightly into the WG SH. The model and physical load geometries are equivalent.

### Material Properties

The material properties of carbon foam used in the simulation are as listed in Table 5.1, ( $\epsilon_r = 2.15 - j0.473$  and  $\mu_r = 1$ ). The material properties for carbon foam presented in Appendix A, Figure A.9 (*median* values) were used directly in the WG simulation.

Comparisons of experimental and simulated S-parameters are presented in Figure 5.9.



**Figure 5.9 - S<sub>11</sub> and S<sub>21</sub> comparison of carbon foam using the WG system**

The results comparison of Figure 5.9 is shown in the following table

**Table 5.2 - Quantitative results comparison; Carbon Foam-Homogeneous Model**

Parameter	Average Error [%]	Maximum Error [%]
$ S_{11} $	5.64	21.29
$\angle S_{11}$	4.56	4.76
$ S_{21} $	4.9	10.47
$\angle S_{21}$	0.57	3.75

### 5.5.2 Carbonatite Ore

The sample of carbonatite ore used during measurements was shown in Figure 4.1 and is approximated as a two phase material of 20% *magnetite* and 80% *calcite* (see Section 4.3.2).

#### (I) Two Phase Solid Sample vs. Homogeneous Model

##### Load Geometry

The homogeneous model of Figure 5.8 was used for the simulation.

##### Material Properties

Material properties of carbonatite corresponding to that listed in Table 5.1 ( $\epsilon_r = 12.72 - j7.21$  and  $\mu_r = 0.24 - j0.0493$ ) were used. These quantities are unedited experimentally extracted parameters (see Section 4.6 for a discussion on these properties). Comparisons of experimental and simulated S-parameters are presented in Figure 5.10.

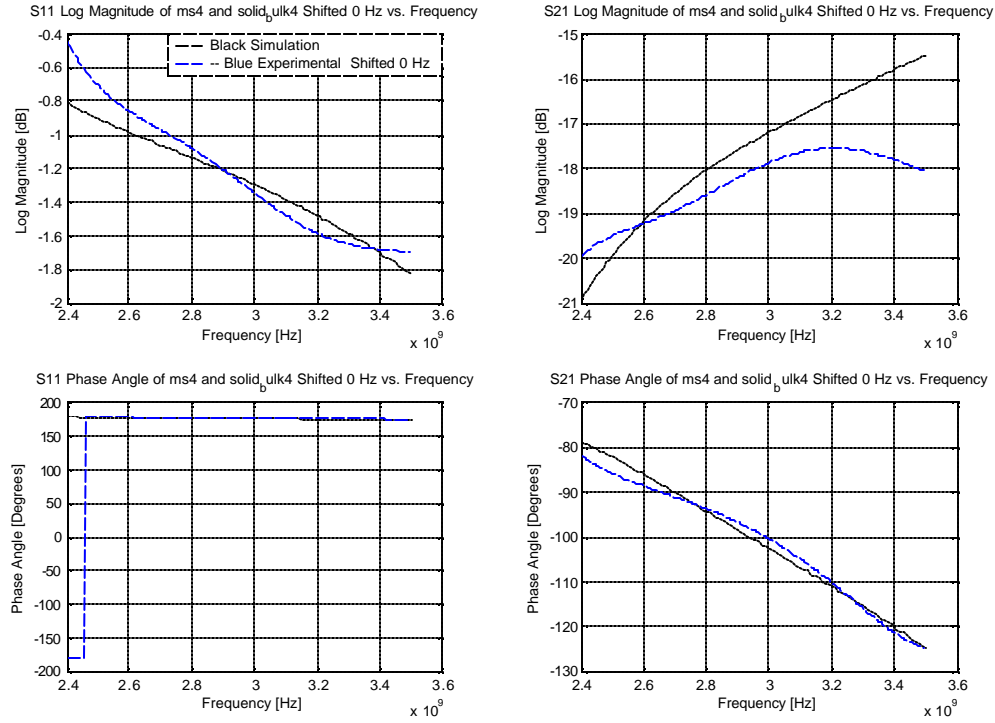


**Figure 5.10 - Homogeneous S<sub>11</sub> and S<sub>21</sub> comparison between measurement and simulation of carbonatite**

The results comparison is shown in the following table.

**Table 5.3 - Quantitative results comparison; Carbonatite-Homogeneous Model**

Parameter	Average Error [%]	Maximum Error [%]
$ S_{11} $	10.68	84.02
$\angle S_{11}$	3.23	5.56
$ S_{21} $	4.96	14.39
$\angle S_{21}$	1.74	4.4

## (II) Two Phase Solid Sample vs. Two Phase Model

### Load Geometry

For reasons stated in Section 5.3 a two phase model of the carbonatite rock needs an accurate geometrical representation of the two phases. To achieve this, the face of the carbonatite sampled was scanned, enlarged and reconstructed digitally as the two phase model presented in Figure 5.11. It was assumed that there is no variation through the thickness of the sample. The visual resemblance of the two phase approximation of the carbonatite is clear from the figure below.

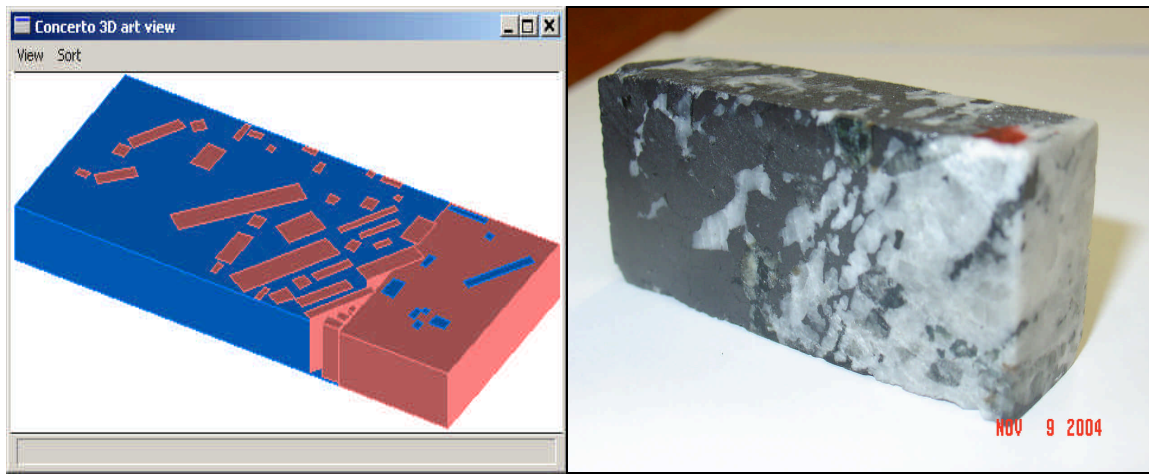


Figure 5.11 - Two phase model of carbonatite reconstructed in Concerto

The blue represents the magnetite phase and the red-brown the calcite. The carbonatite model also took the 2 mm gap between the top of the sample and WG into account (see Section 4.3.2 Figure 4.1).

### Material Properties

Properties for calcite were chosen to be:  $\epsilon_r = 6 - j0.012$  and  $m_r = 1$ . These were decided upon after measurement and iterative simulations were done.

Both measurement systems indicated that magnetite is a conductive material (Sections 4.4.1 and 4.4.2). Therefore surface losses are defined in Concerto and both  $\dot{m}_r$  and  $s_e$  must be specified (Section 5.4.1.1). As discussed in Section 4.5.2 a value of  $\dot{m}_r = 100$  was found in Haus and Melcher [36]. Shuey [37] quoted a wide range of values for  $s_e$  ( $50 \text{ S/m}$  to  $3 \times 10^4 \text{ S/m}$ ). After reviewing [37] and conductivity values of semi-conductor materials [13] a value of  $s_e = 100$  was chosen for magnetite.

The S-parameter comparison is shown in Figure 5.12.

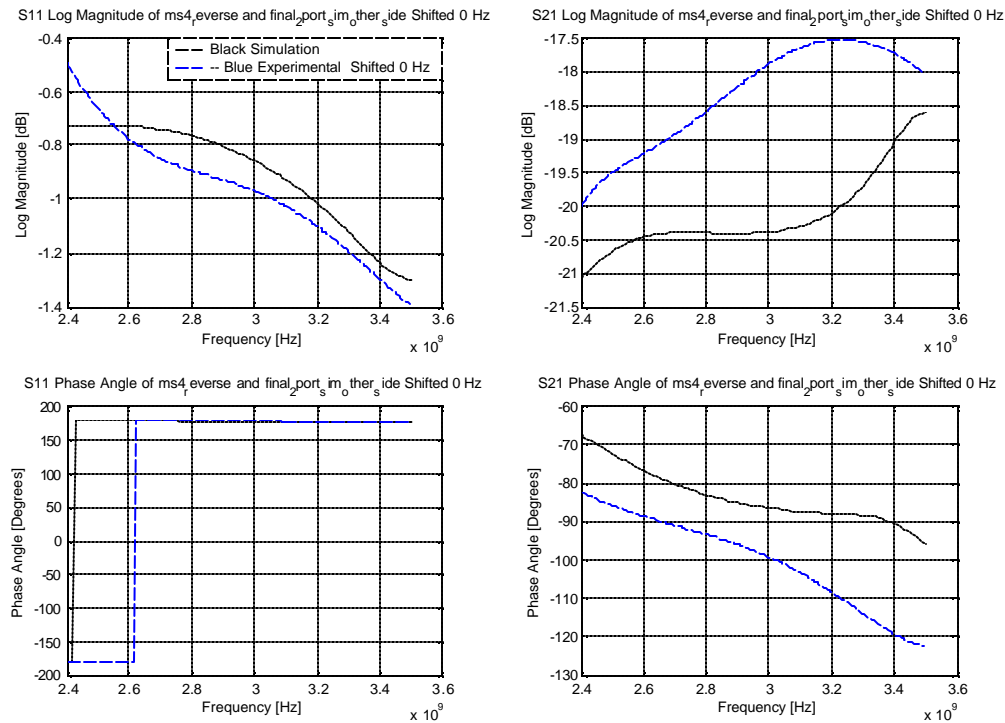


Figure 5.12 - Two-phase  $S_{11}$  and  $S_{21}$  comparison between measurement and simulation of carbonatite

The results comparison is shown in the following table.

**Table 5.4 - Quantitative results comparison; Carbonatite-2 Phase model**

<b>Parameter</b>	<b>Average Error [%]</b>	<b>Maximum Error [%]</b>
$ S_{11} $	10.71	46.49
$\angle S_{11}$	3.83	4.66
$ S_{21} $	9.95	15.13
$\angle S_{21}$	16.1	24.08

### 5.5.3 Crushed Carbonatite Ore

The crushed carbonatite ore sample was shown in Figure 4.3 and had a packing density of 44% rocks to 56% air (Section 4.3.3). Different rock packings inside the *SH* had an anisotropic effect and different S-parameters were measured for different packings. The minimum and maximum S-parameter values of two different packings interrogated from both sides (4 sets of S-parameters) were determined. These upper and lower bounds were compared with simulation results to account to some extent for the anisotropy of the load.

#### (I) Three Phase Sample vs. Homogeneous Model

##### Load Geometry

The homogeneous model of Figure 5.8 was used.

##### Material Properties

As anticipated from the anisotropic nature of the crushed ore in the cavity, different properties were measured for different packings of rocks inside the cavity (see Appendix A, Table A.1 for results). The dielectric constant values range between 2.6 and 4.21. An average value of 3.5 was chosen. The loss factor was chosen after iterative simulations

were done. The magnetic properties were chosen an average number of the repeatable results and rounded (where a negative sign indicates an indeterminate value because of higher order modes or half wavelength uncertainty). The material properties used are listed in Table 5.1 ( $\epsilon_r = 3.5 - j0.35$ ;  $\mu_r = 1$ ).

Comparative results are shown in Figure 5.13.

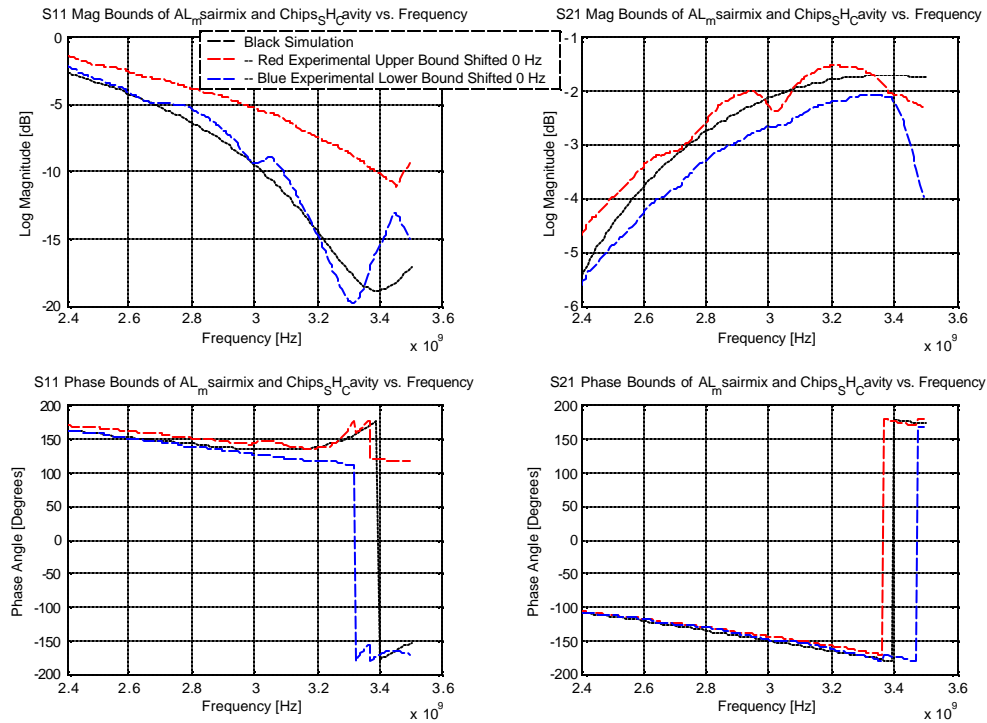


**Figure 5.13 - S<sub>11</sub> and S<sub>21</sub> boundary comparison between measurement and simulation of crushed ore. There was no discretization frequency shift required to compare the measured and simulated results**

Average and maximum percentage errors were determined for the simulation results compared to the measured bounds. Where the simulation S-parameters are within the bounds it is considered to agree with measured results. If the simulation is above or below the bounds, the error is determined relative to the closest boundary. This argument applies to all subsequent boundary comparisons. The following table gives the percentage errors.



**Table 5.5 - Quantitative results comparison; Crushed Ore-Homogeneous model**

Parameter	Average Error [%]	Maximum Error [%]
$ S_{11} $	9.99	40.44
$\angle S_{11}$	0.28	73.74
$ S_{21} $	3.11	25.24
$\angle S_{21}$	1.73	23.06

## (II) Three Phase Sample vs. Two Phase Model

Two different two-phase models and results are presented here to illustrate the effect the load geometry can have on the simulation model.

### (II.I) Clustered Simple Geometry

#### Load Geometry

An unrealistic geometrical representation of the load was simulated deliberately to expose the sensitivity of the model to geometry. This model consisted of 30 homogeneous carbonatite particles of size  $(10 \times 10 \times 10)$  mm immersed in air within the dimensions of the SH2 cavity  $(72 \times 34 \times 25)$  mm. This gives a packing density of 49% and is close to the 44% packing density *measured* (see Section 4.3.3), however the rock particles are clustered in the middle of the cavity. The model is shown in Figure 5.14.

#### Material Properties

The material properties used for the carbonatite are the same as used for the homogeneous representation of the solid slab of carbonatite (Section 5.5.2). It was experimentally determined (Section 4.6) and listed in Table 5.1 ( $\epsilon_r = 12.72 - j7.21$ ;  $m_r = 0.24 - j0.0493$ ).

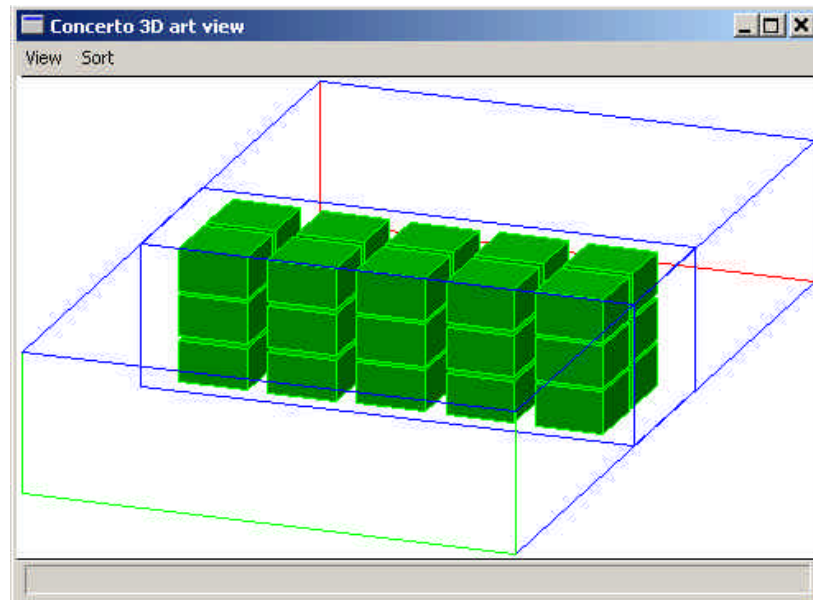


**Figure 5.14 - 3D view of an unlikely rock distribution in the WG SH**

Comparative results are presented in Figure 5.15.

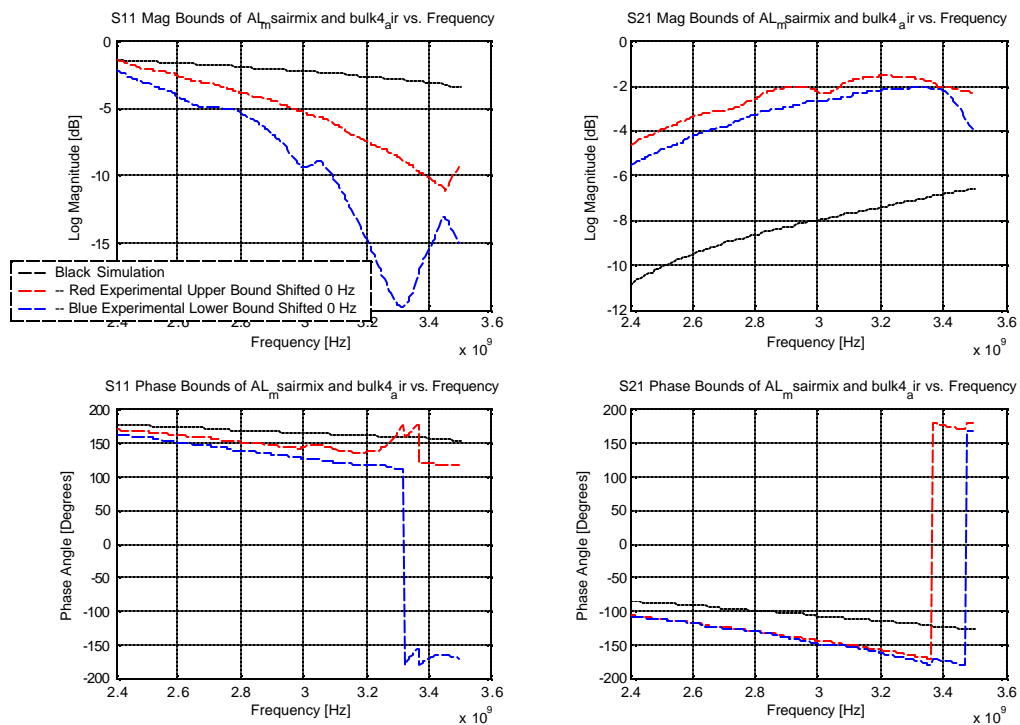


**Figure 5.15 -  $S_{11}$  and  $S_{21}$  comparison between measurement and simulation of crushed ore**

The results comparison is shown in the following table.

**Table 5.6 - Quantitative results comparison; Crushed Ore-Simple 2 Phase model**

Parameter	Average Error [%]	Maximum Error [%]
$ S_{11} $	51.24	70.28
$\angle S_{11}$	9.88	33.87
$ S_{21} $	171.15	171.42
$\angle S_{21}$	24.97	29.06

## (II.II) Rock Particles Spread and Rotated Alternately

### Load Geometry

A more realistic model is the rock particles spread evenly and to the sides of the cavity. This model consists of 30 carbonatite particles of dimensions  $(10 \times 10 \times 9) \text{ mm}$ , giving a packing density of 44.1% (consistent with the measured ratio, see Section 4.3.3). Note that each alternate particle was *rotated* by 45 degrees. This model is presented below.

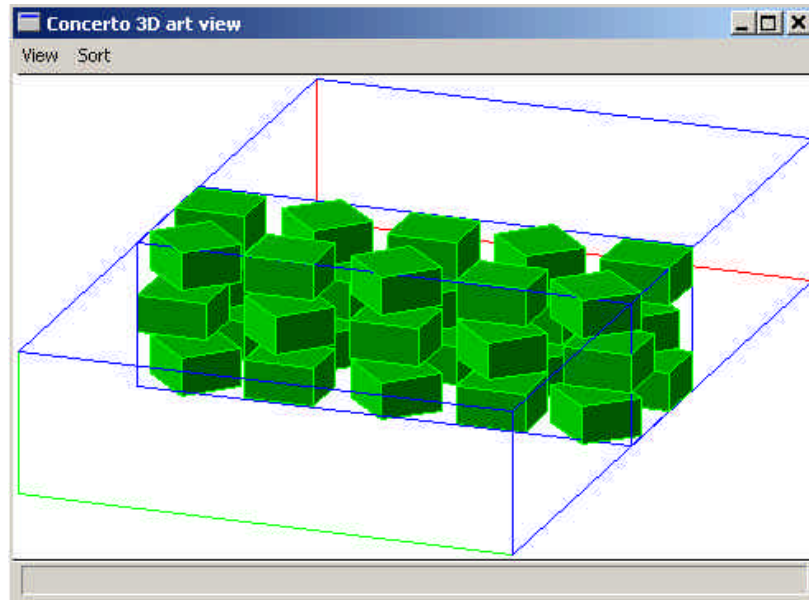


**Figure 5.16 - 3D view of a more representative model of the physical load of crushed rocks**

### Material Properties

Material properties of the rock particles are the same as the unrepresentative model displayed in Figure 5.14 ( $\mathbf{e}_r = 12.72 - j7.21$ ;  $\mathbf{m}_r = 0.24 - j0.0493$ ).

Figure 5.17 presents the comparative results.

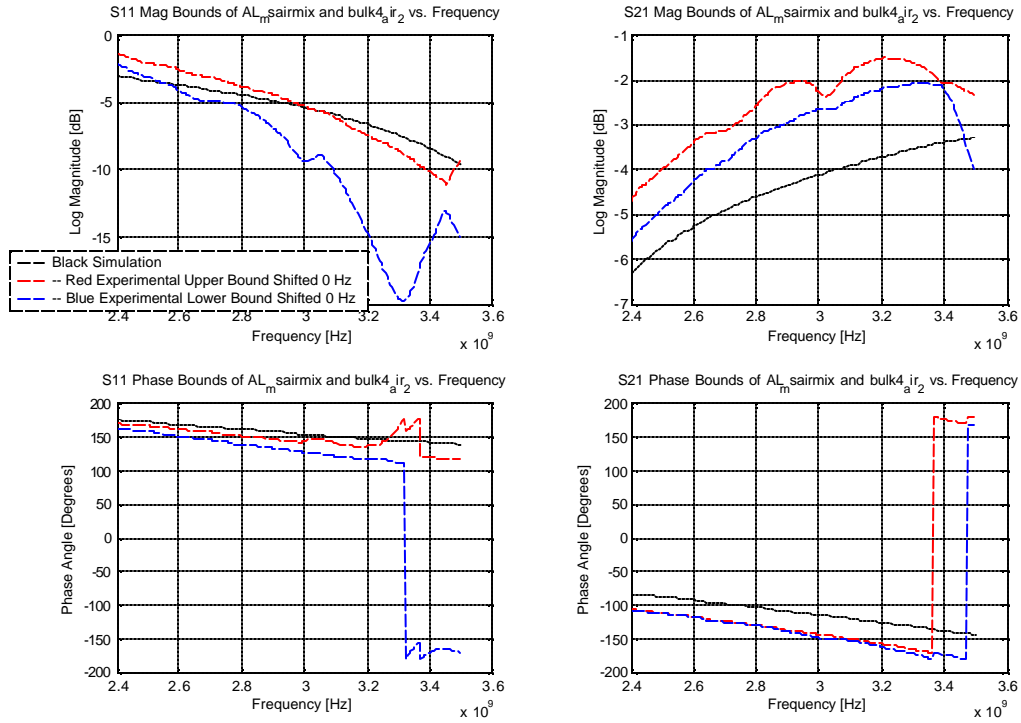


**Figure 5.17 - S<sub>11</sub> and S<sub>21</sub> boundary comparison between measurement and simulation of crushed ore**

The results look more convincing and the percentage comparison is shown in the following table.

**Table 5.7 - Quantitative results comparison; Crushed Ore-Improved 2 Phase model**

Parameter	Average Error [%]	Maximum Error [%]
$ S_{11} $	6.5	17.9
$\angle S_{11}$	4.93	21.08
$ S_{21} $	41.89	67.25
$\angle S_{21}$	20.65	20.68

It is clear from Tables 5.6 and 5.7 that by changing the geometry, an improvement on simulation results can be made. Appropriate geometrical representation becomes important for multiphase models.

### (III) Three Phase Sample vs. Three Phase Geometry

#### Load Geometry

The geometry consists of 30 particles of rock inside *SH2*. Each rock particle has dimensions of  $(10 \times 10 \times 9)$  mm to give a 44.1% *packing density* of rock particles to air (consistent with the measured rock air ratio; see Section 4.3.3). The spread particle approach of (II.II) above was used, but without the particles being rotated. Each rock particle consists of 4 blocks of *magnetite* of  $(3 \times 3 \times 3)$  mm immersed in a *calcite* particle of  $(10 \times 10 \times 9)$  mm to give a *magnetite/calcite ratio* of 13.6/86.4%. This is a little less than predicted by the discussion in Section 4.3.3. As a naturally occurring element, variations to 20% are expected. The magnetite blocks are spaced to the four corners of the rock particle. The model is presented in the following figure.

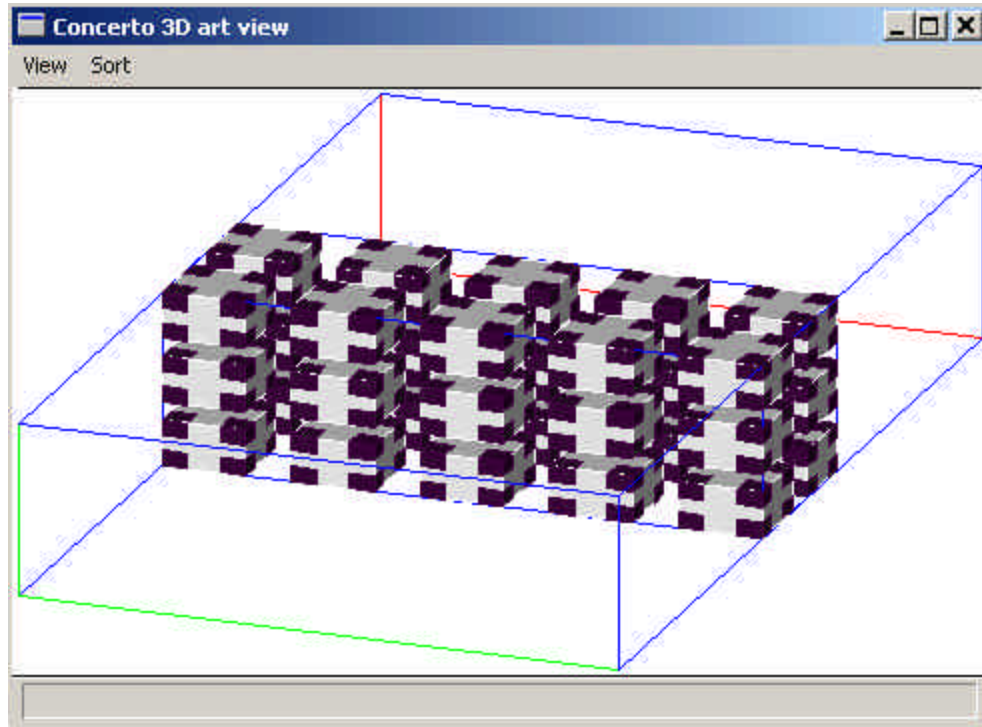


Figure 5.18 - Three phase model of the crushed ore inside the WG SH

The white-grey represents calcite and the black the magnetite.

### Material Properties

The material properties of each phase were listed in Table 5.1 but are repeated here for convenience. Calcite:  $\epsilon_r = 6 - j0.012$  and  $\mu_r = 1$ ; Magnetite (defined with surface loss):  $\mu_r = 100$  and  $s_c = 100$ .

Comparative results are presented in Figure 5.19.

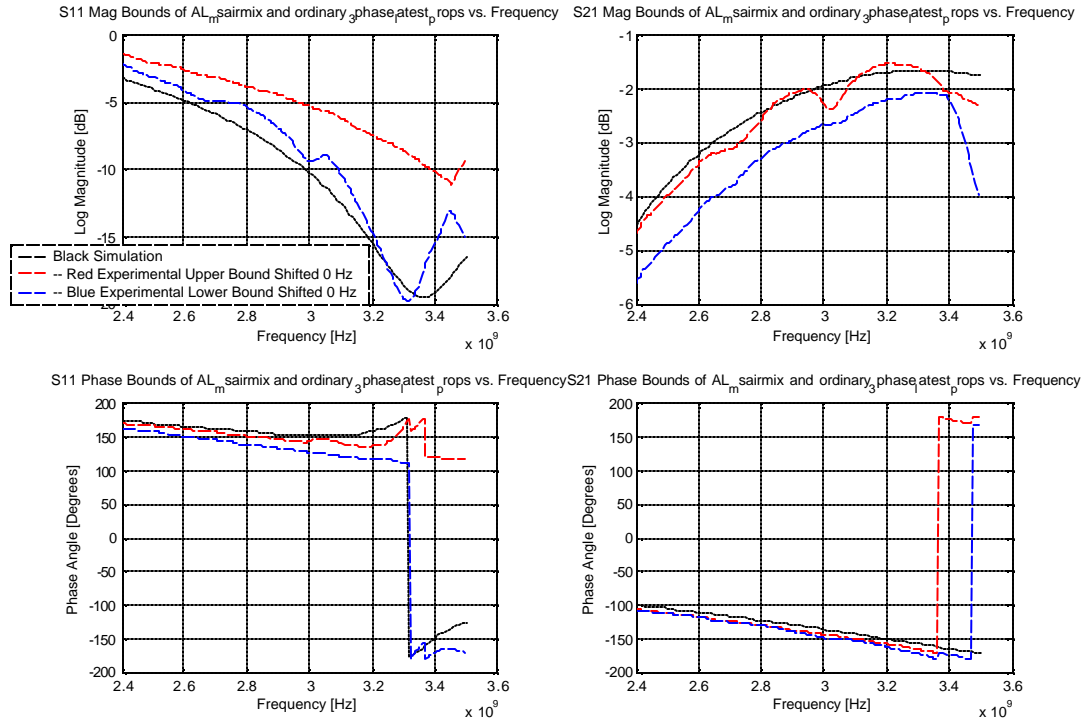


Figure 5.19 -  $S_{11}$  and  $S_{21}$  comparison between measurement and simulation of crushed ore

A results comparison is shown in the following Table.

Table 5.8 - Quantitative results comparison; Crushed Ore-3 Phase model

Parameter	Average Error [%]	Maximum Error [%]
$ S_{11} $	19.46	38.54
$\angle S_{11}$	7.94	26.65
$ S_{21} $	6.66	25.02
$\angle S_{21}$	5.18	5.31

This section showed that using three different models for a three phase material, results agree in or close to experimental bounds. Some results are better than others as a function of geometry. It is not known *a priori* how good the geometrical representation needs to

be. More simulations should be conducted to establish a better relationship between material properties and geometry.

In Section 5.6 the same approach will be followed but for a cylindrical single mode cavity.

## ***5.6 Comparison of Single Mode (SM) Cavity Measurement and Simulation***

To support the *WG* measurements and simulations similar comparisons were done on a cylindrical single mode cavity. The single mode cavity is a one port system and therefore only an  $S_{11}$  comparison was possible. Only the  $S_{11}$  magnitude will be compared.

### **5.6.1 Description of Single Mode Cavity Experiment**

A single mode cavity, developed at Nottingham University (*NU*) in England, was replicated at the *US* with inner dimensions shown in Figure 5.20. After a full one port calibration the applicator was connected to the *ANA* via the left hand *WG* as shown in Figure 5.20. The other end of *WG* was short circuited. After the cavity was loaded, the top and bottom ends were sealed with metal discs and metallic tape.



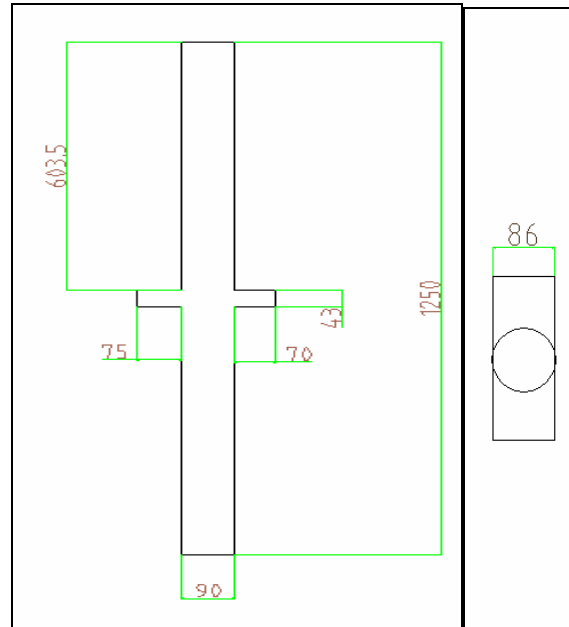


**Figure 5.20 - Transverse and plan view of the NU single mode cavity; dimensions in mm**

Two different carbonatite loads were placed inside the cavity. *Firstly* a solid carbonatite cylinder (dimensions: *height* = 74mm, *diameter* = 36mm) was placed coaxially in the middle of the cavity with the help of Styrofoam support. The cylinder is approximated to consist only of calcite and magnetite. *Secondly* crushed ore was placed inside a Pyrex<sup>®</sup> (Borosilicate glass) cylinder (inner dimensions: *height* = 300mm, *diameter* = 72mm) and supported by strings positioning the load vertically in the middle of the cavity. Styrofoam rings placed at the top and bottom of the Pyrex<sup>®</sup> cylinder helped to position the load horizontally in the middle (Figure 5.21).



Figure 5.21 - Load of crushed ore (approximated as a 3 phase load)

According to von Hippel [20] the properties of Styrofoam and Pyrex<sup>®</sup> are

Table 5.9 - Table showing the material properties of Styrofoam and Pyrex<sup>®</sup>, (after von Hippel [20])

Material	T [°C]	f [GHz]	Composition	$\epsilon_r'$	$\epsilon_r''$
Styrofoam	25	1.6	Close to air	1.03	0.0001545
Pyrex <sup>®</sup>	25	1.6	73.2% SiO <sub>2</sub> ; 24.8% B <sub>2</sub> O <sub>3</sub>	4.05	0.00628

From Table 5.9 it is clear that Pyrex<sup>®</sup> and Styrofoam are low loss materials and for modelling purposes it can be ignored. The strings are volumetrically minute and displaced from the active region of the applicator and can also be ignored in the load model.

The packing density is assumed to be the same as calculated for the *SH* (i.e. 44% rock-air ratio). Note that since the rocks are randomly spaced inside the Pyrex cylinder, the load is expected to be anisotropic. In an attempt to compensate for the anisotropy of the load geometry, the cylinder was rotated to four different angles (90 degrees out of phase) inside the cavity and  $S_{11}$  was extracted at each position. The four different sets of  $S$ -

parameters were used to calculate an upper and lower boundary of experimental data. Simulation S-parameters are then compared to these boundary values.

### 5.6.2 Two Phase Load vs. Homogeneous Model

The two phase load refers to the solid carbonatite cylindrical load.

#### Load Geometry

The homogeneous model are of the same dimensions as the solid carbonatite cylinder (*height = 74mm, diameter = 36mm*) and is shown in the figure below.

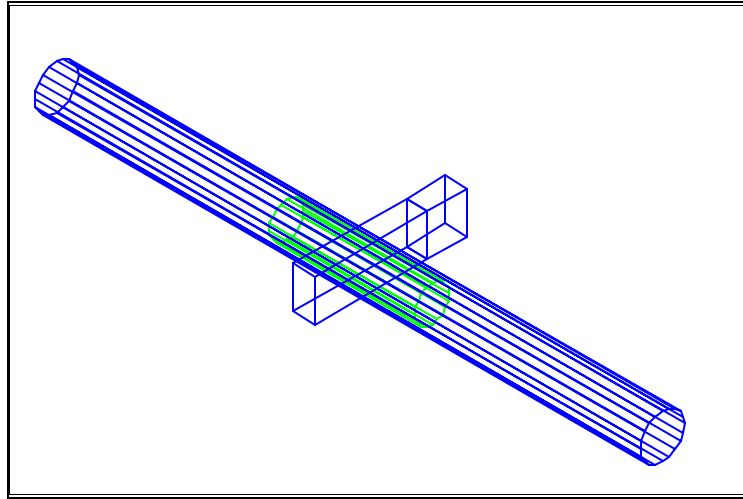
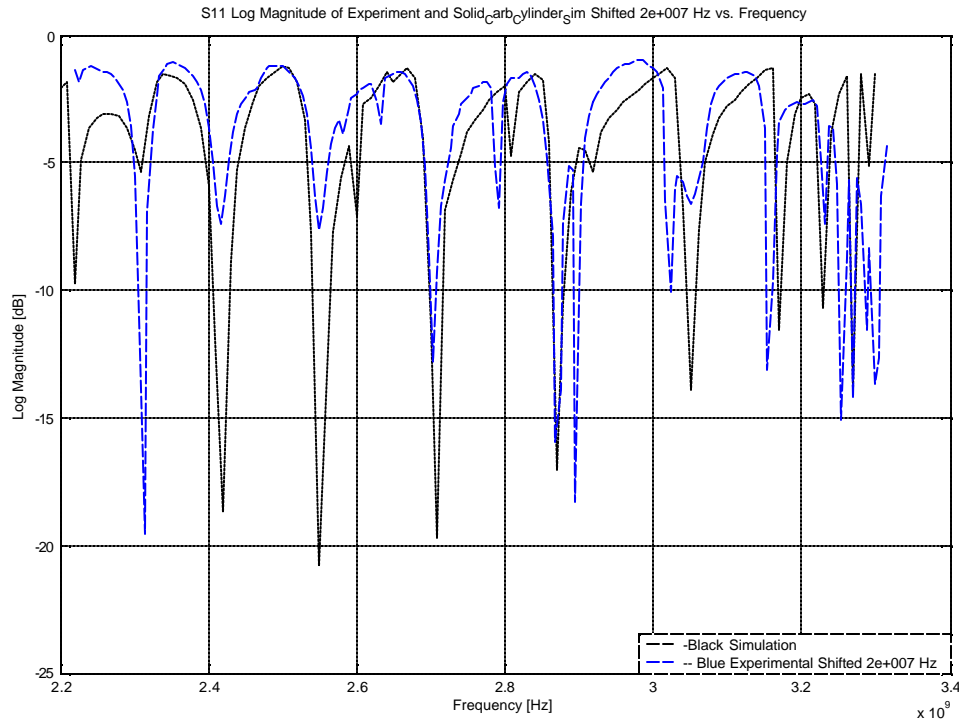


Figure 5.22 - Isometric view of homogeneous load inside the single mode cavity

#### Material Properties

Material properties for the carbonatite model are summarised in Table 5.9. It is the same properties used in the *WG* simulation of the carbonatite slab in Section 5.5.2-(I) ( $\epsilon_r = 12.72 - j7.21$  and  $m_r = 0.24 - j0.0493$ ). These properties were experimentally extracted and unedited. Comparative results are shown in the following figure.



**Figure 5.23 -  $S_{11}$  Magnitude comparison of a solid carbonatite cylinder**

After a 20 MHz shift in frequency, all the dominant resonances are found by the simulation. The required shift in frequency can be a combination of a discretization error and incorrect material properties. This matter requires further investigation and no conclusion regarding this frequency shift will be made here.

Determining an average percentage error can be misleading since resonant points that do not align with each other can create errors of a few hundred percent. Even though the simulation and measured  $S_{11}$  do show similar resonant modes, huge errors will dominate the average value. It was therefore decided to take a *median* error to reduce the weighting of the large errors. This argument regarding a median error comparison will apply to all the single mode cavity comparisons. In Figure 5.23 the first and last few frequency points were also ignored to focus on the central region where predicted and measured results show a similar behaviour.

The median error of the simulation results in Figure 5.23 compared to measurement is 42.9%. This figure is relatively large and one should not forget that a qualitative comparison of resonant modes show good agreement.

### 5.6.3 Three Phase Load vs. Homogeneous Model

The three phase load refers to the crushed carbonatite ore inside the Pyrex<sup>®</sup> cylinder.

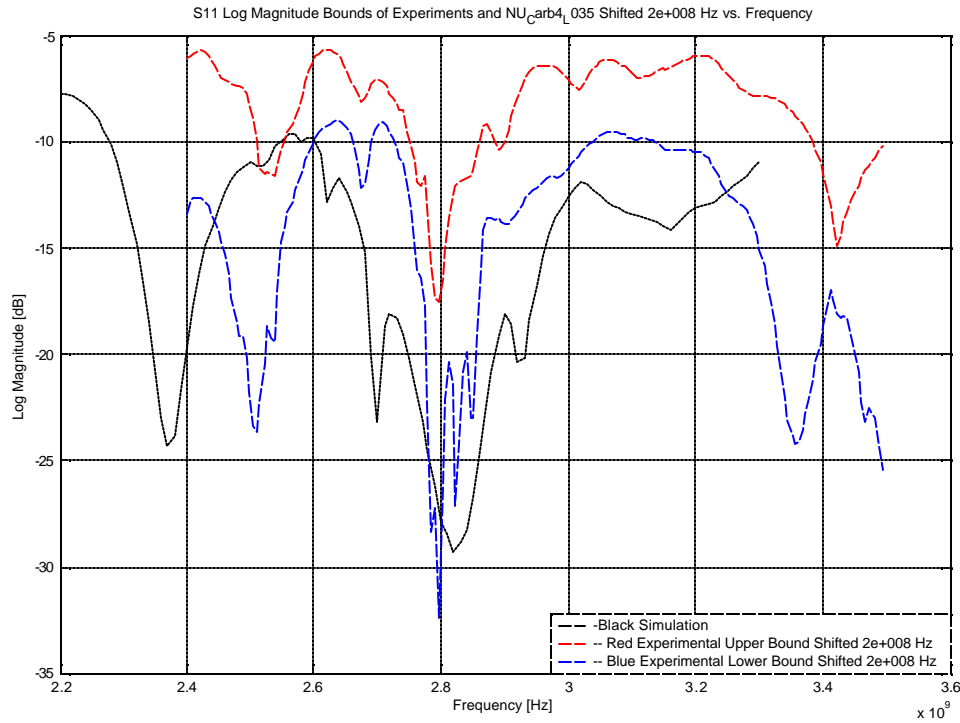
#### Load Geometry

Figure 5.22 gives an isometric view of the simulation model. The homogeneous load geometry takes the shape of the Pyrex<sup>®</sup> cylinder's inner dimensions (*diameter of 72mm and 300mm high*).

#### Material Properties

The same material properties were used as in the *WG* homogeneous model of crushed ore (Table 5.1) and are repeated here;  $\epsilon_r = 3.5 - j0.35$  and  $\mu_r = 1$ .

Results are presented in Figure 5.24.



**Figure 5.24 - Experimental upper and lower bounds compared to the homogeneous simulation model**

A frequency shift of  $200 \text{ MHz}$  is required to achieve the best comparison between simulation and experiment. The level of absorption is the same and all the main features of the experimental data are captured by the simulation.

For this and all subsequent bound comparisons the median error of *the entire region* where *the graphs overlap* will be determined. The *median error* of simulation compared to the measured bounds in Figure 5.24 is 27.75%.

### 5.6.3.1 Sensitivity Analysis of Material Properties

To demonstrate parameter sensitivity, the above simulation was repeated but with material properties changed to the following,  $\mathbf{e}_r = 3.5 - j0.375$  and  $\mathbf{m}_r = 1$  (i.e.  $\mathbf{e}_r''$  increases by 7.1%).

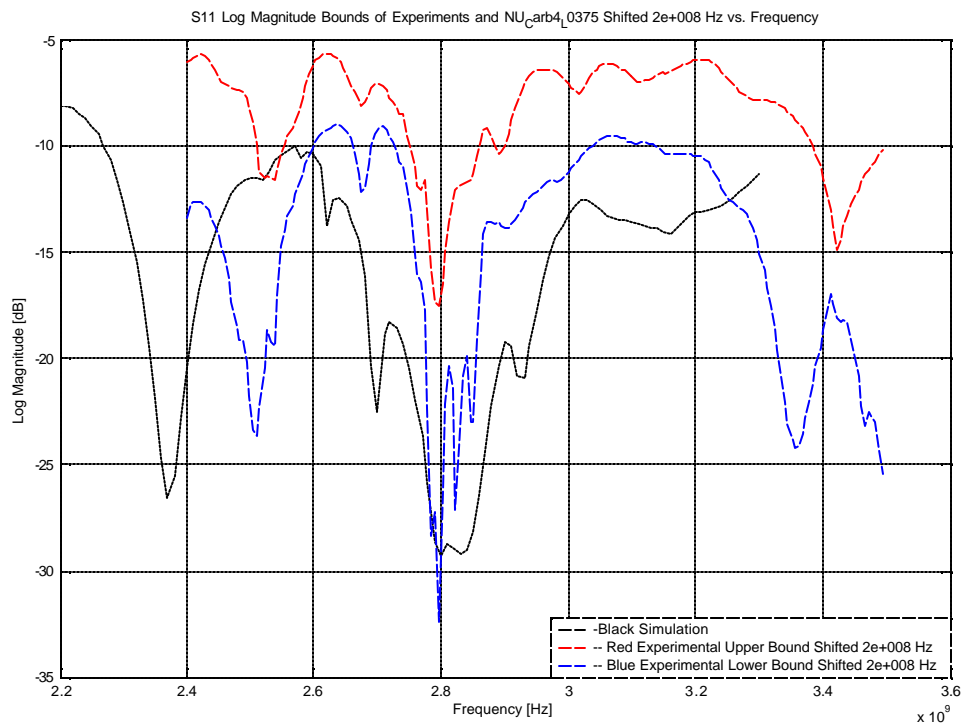


**Figure 5.25 -  $S_{11}$  Magnitude comparisons with changed material properties**

The *median* percentage error is 31.83%, a 4% increase on Figure 5.24. This indicates that small errors in measured material property results will not have a dramatic effect on the simulation S-parameter results.

#### 5.6.4 Three Phase Load vs. Two Phase Model

##### Load Geometry

The simulation model of the two phase load is shown in Figure 5.26.

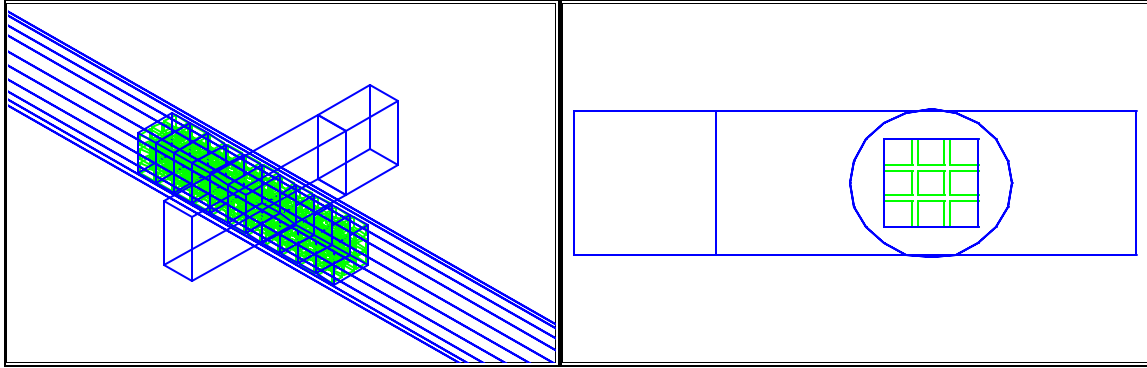


**Figure 5.26 - Isometric and plan view of 2 phase simulation model of the load**

The load model consists of 11 slabs of air, each 27 mm high stacked onto one another to give a height of 297 mm. Each slab is 52 x 52 mm which results in a diagonal of 73.5 mm. Every layer of air contains 9 rectangles of rock (15 x 15 x 20) mm spaced to the edges, with a layer of air above and below them. This yields a packing density of 55.47%, which is 11% higher than measured for the *WG SH*. A less dense packing density is simulated in the next section.

### **Material Properties**

Each of the 9 rocks take on experimentally determined carbonatite properties (Table 5.1;  $\mathbf{e}_r = 12.72 - j7.21$  and  $\mathbf{m}_r = 0.24 - j0.0493$ ).

Comparative results are shown in Figure 5.27.



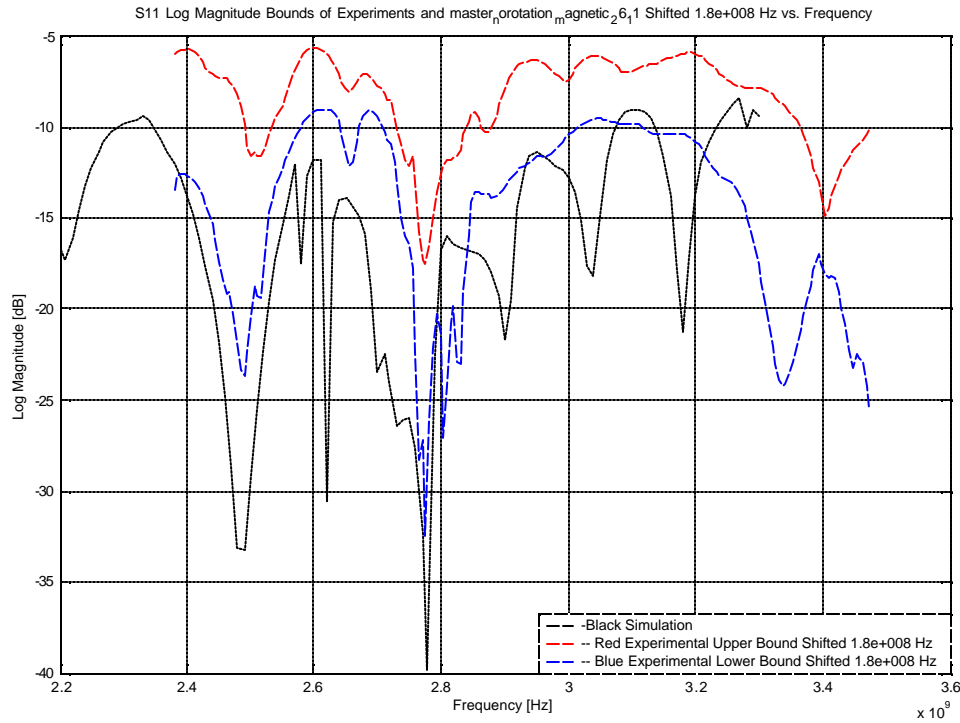


**Figure 5.27 -  $S_{11}$  Magnitude of 2 phase load compared to measured bounds**

A frequency shift of a  $180\text{ MHz}$  is introduced. In general the simulated results show more power absorption, but the main features are captured together with a few spurious resonances. The percentage median error is  $28.9\%$ . Even though the packing density is  $11\%$  higher than the real system, the agreement is relatively good.

#### 5.6.4.1 Less Dense Load Model

The same load geometry as above was used, but with the rectangular rocks ( $15 \times 15 \times 16\text{ mm}$ ). This gives a packing density of  $44.4\%$ , compared with  $55\%$  in the previous model.

The material properties stayed the same and the result is presented in the following figure.

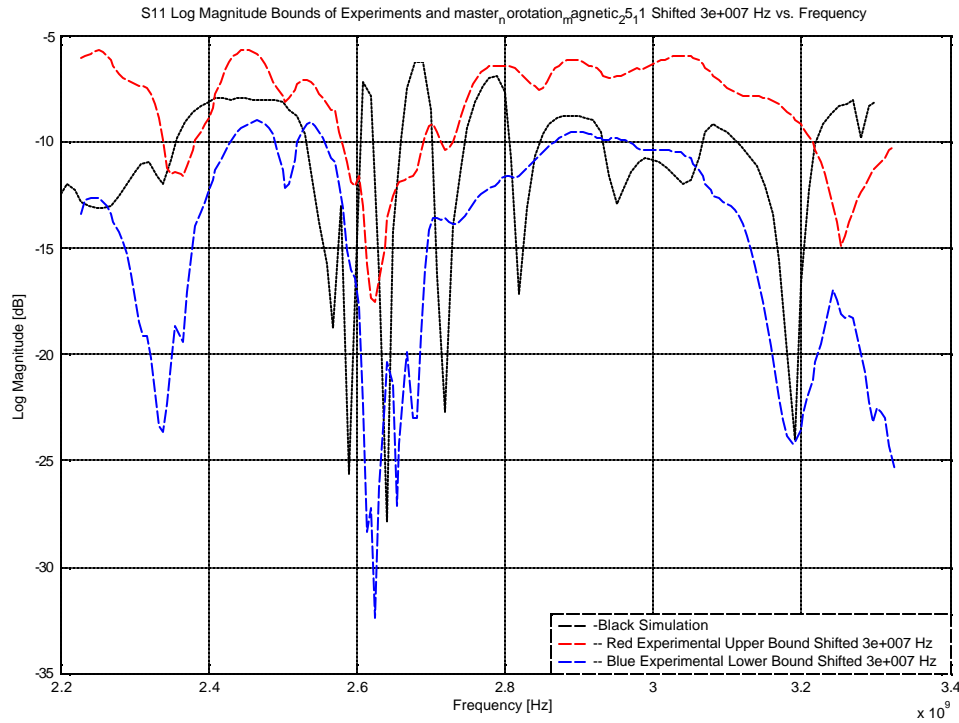


**Figure 5.28 -  $S_{11}$  Magnitude comparison of a less dense 2 phase model**

A 30 MHz frequency shift is required for comparison. The level of absorption agrees, but the result shows more resonances than the densely packed model. The median error is 0% and the average error is determined. The percentage average error is 10.6%. The less dense model, in agreement with the real cavity, *improved* the average error with approximately 18%.

### 5.6.5 Three Phase Load vs. Three Phase Model

Again, to illustrate the importance of accurate geometric representation a simple three phase geometry with results will be given and then a more complex representation with results.

### 5.6.5.1 Simple Load Model

#### Load Model

The load model consists of fifteen,  $20\text{ mm}$  high slabs of air placed on top of one another. This gives a load height of  $300\text{ mm}$ . The side lengths are  $(51 \times 51)\text{ mm}$  and each slab is rotated by  $45\text{ degrees}$  alternately. Nine blocks of calcite, geometry of  $(14 \times 14 \times 14)\text{ mm}$ , are placed inside each slab of air. To complete the three phase model each block of calcite contains 4 magnetite particles, geometry:  $(4 \times 4 \times 4)\text{ mm}$ , immersed inside it. The densities calculate to the following: *Packing Density* =  $47.47\%$ ; *Magnetite/Calcite* =  $9.3/90.7\%$ . The load model is showed in the figure below.

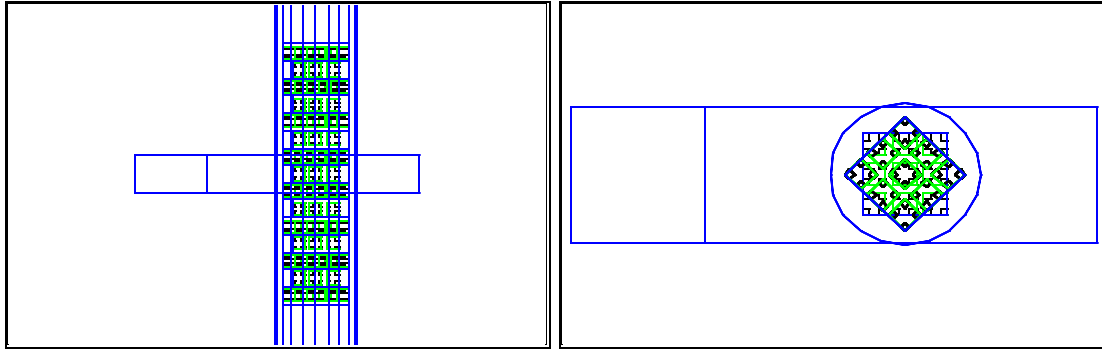
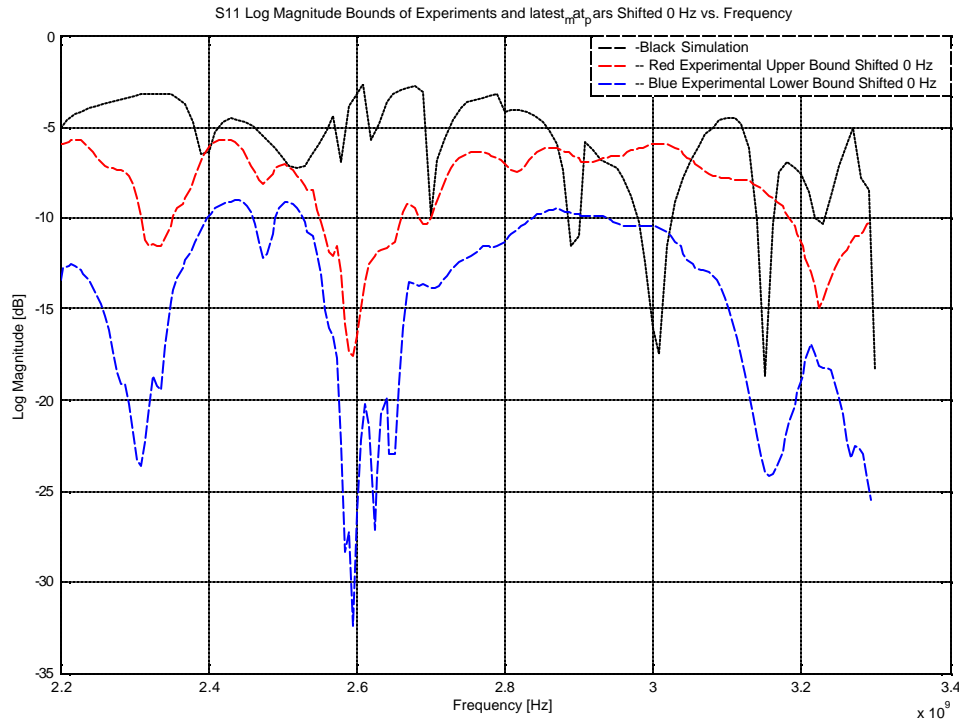


Figure 5.29 - Transverse and plan view of an unrealistic three phase model

#### Material Properties

The material properties listed in Table 5.1 are used (Calcite:  $\epsilon_r = 6 - j0.012$  and  $\mu_r = 1$ ; Magnetite (defined with surface loss):  $\mu_r = 100$  and  $s_c = 100$ ). The choice of properties was explained in Section 5.5.2.

Results are presented in the following figure.



**Figure 5.30 -  $S_{11}$  Magnitude comparison of an unrealistic load model with experimental bounds**

From the figure above it is clear that the main features of the experimental results are not replicated. However, the *median* error is 33.6%, which is in line with, or better than *median* errors quoted for results showing a superior qualitative comparison (e.g. Figure 5.23). It is therefore important to note that a *median* error alone is not enough to judge the comparison. A qualitative analysis of replication of resonant frequencies is also important. Again the importance of geometrical representation becomes clear.

### 5.6.5.2 More Realistic Load Model

#### Load Geometry

A load was designed that consists of three different patterns that are alternately stacked on one another and rotated. This model had a 50% *packing density* and a 10/90% *magnetite/calcite* mixture. The load model is presented in the following figure.

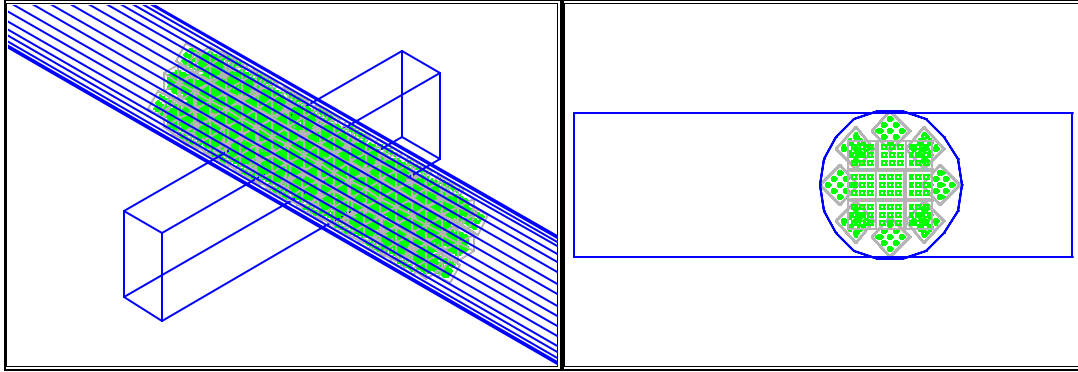


Figure 5.31 - Isometric and Plan View of 3 phase simulation model for rock and air mixture

### Material Properties

Material properties are the same as in the previous simulation and were listed in Table 5.1. (Calcite:  $\epsilon_r = 6 - j0.012$  and  $\mu_r = 1$ ; Magnetite (defined with surface loss):  $\mu_r = 100$  and  $s_c = 100$ ).

Comparative results are shown in the figure below.

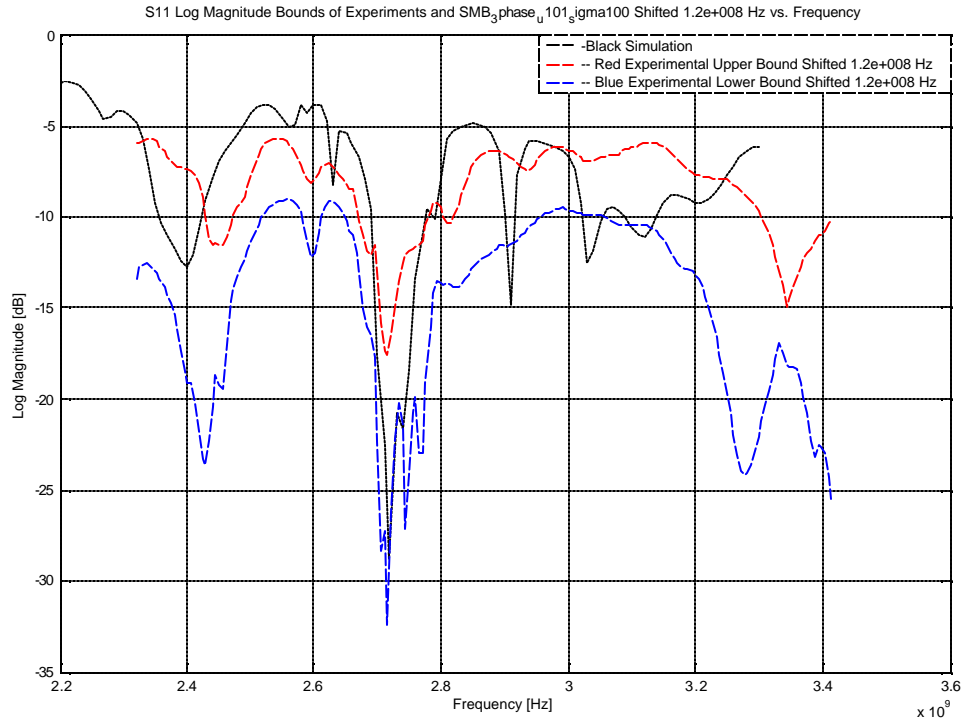


Figure 5.32 -  $S_{11}$  Magnitude comparison of complex 3 phase model and experimental bounds

After a  $120\text{ MHz}$  frequency shift all the main features of the experimental results are captured by the simulation. The level of absorption is also the same. The simulation does show a few spurious resonances. However the *median* error is  $6.54\%$ . This is the best agreement achieved, qualitatively and quantitatively, of all the simulations of the single mode cavity.

### 5.6.5.3 Sensitivity Analysis of $s_c$

Using the same complex load model of Section 5.6.5.2, the sensitivity of the system to the conductivity parameter was analysed. This was of particular interest as the chosen value of  $s_c = 100$  was the parameter with most uncertainty (estimated from literature). Values of conductivity were halved and doubled ( $s_c = 50$  and  $s_c = 200$ ) and the three comparative results are presented in the figure below.

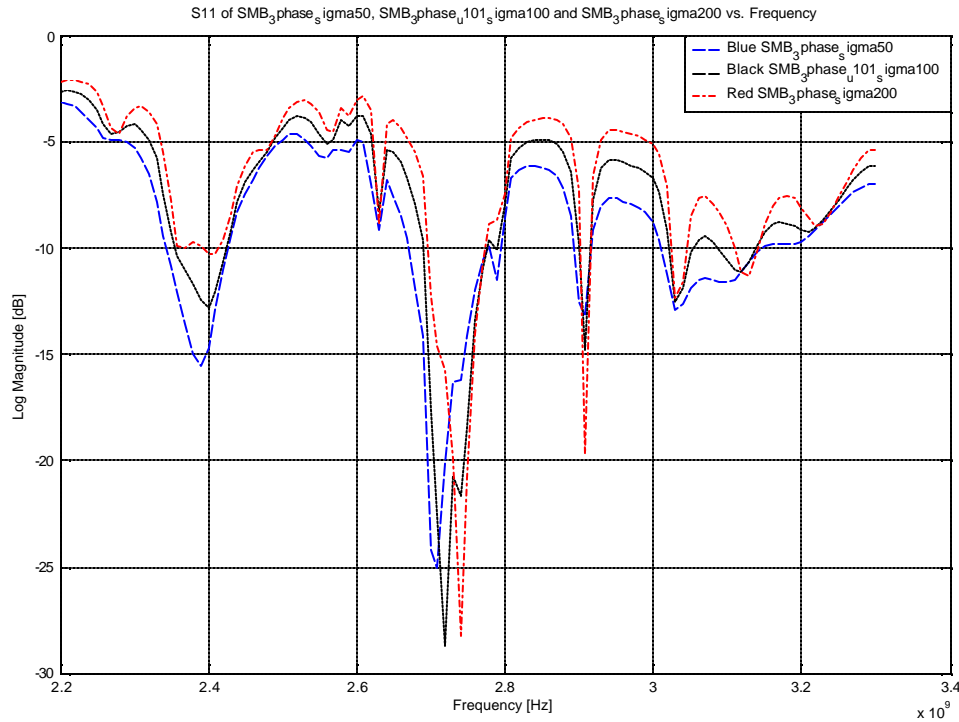


Figure 5.33 -  $S_{11}$  Magnitude comparisons for different values of conductivity

From the figure above the variation in the  $S_{11}$  magnitude is small and will not be quantified. There is also a marginal frequency shift in resonance, but the general comparison is good. This indicates that by increasing the conductivity by 100% and decreasing it by 50% no significant changes on the scale of experimental comparison are observed.

## 5.7 Conclusion

This Chapter focussed on *FDTD* simulated and measured S-parameters comparison as a technique to verify different material models of different samples. This approach was applied to a *WG* sample holder cavity and a cylindrical single mode cavity and results were presented. Some differences are observed in the S-parameter comparisons. Unrealistic geometrical models were simulated and showed differences of up to 180% for some of the parameters compared to the measured results. More realistic geometrical models were simulated and compared to within 5% of the measured results. The general accuracy for the various realistic geometrical models is good. It can be concluded from these comparisons that the various material properties have been determined well, but accurate geometrical representation of multiphase materials is important.

The simulation results of the cylindrical single mode applicator required a shift in frequency for results to be comparative to measurement. The required shift needs further investigation but may be a combination of a discretization error and incorrect material properties.

Not all of the materials could be quantified with the available measurement techniques and values recorded in literature were consulted. The conductivity and permeability of magnetite were approximated from literature values. As a sensitivity analysis, it was shown that the complex three phase model used in the single mode applicator is not sensitive to variations in the value of conductivity.

## Chapter 6

# Cavity Probing and Simulation Field Plots: An Application of Material Properties

---

### ***6.1 Introduction***

Measured material properties and geometrical representation were refined and verified in Chapter 5. This chapter presents cavity probing and field distributions of a cylindrical applicator with a rock sample positioned close to the top of the cavity. Homogeneous and two phase models are used in simulations to illustrate the importance of an accurate representation of multiphase materials. Simulation and experimental field distributions are then compared.

The chapter starts with a discussion on the experimental determination of electrical field (E-field) distribution in Section 6.2. Section 6.3 presents the simulation model and comparative results are presented in Section 6.4. Section 6.5 present simulation and measured electric field comparisons of a prototype mineral processing applicator. A chapter conclusion is made in Section 6.5.

### ***6.2 Experimental Determination of E-Field Distribution***

A general measurement setup for field probing is shown in the following figure.



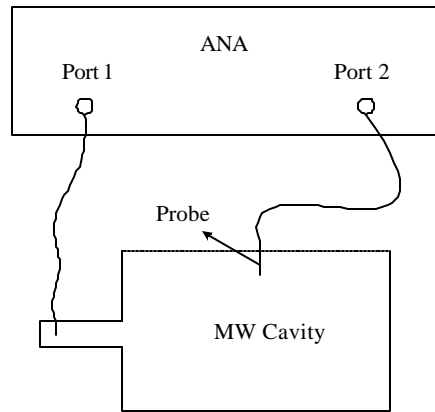


**Figure 6.1 - General setup for field probing**

General field-probing of a *MW* cavity consist of the following steps. Port 1 of the *ANA* is calibrated and connected to the cavity feed. Resonant frequencies are then determined from an  $S_{11}$  measurement. Port 2 of the *ANA* is connected to a probe and the  $S_{21}$ -parameter is measured through different holes of a meshed metal plate. It is then converted to a composite E-field distribution-plot at the frequency of interest.

### 6.2.1 Field-Probing of a Cylindrical MW Cavity

The system under investigation was a cylindrical cavity that is fed with a current loop. This cavity has been probed by van der Merwe [43]. This technique will be described, results presented and applied to a potential mineral processing cavity. The measurement setup is shown in the following figure.

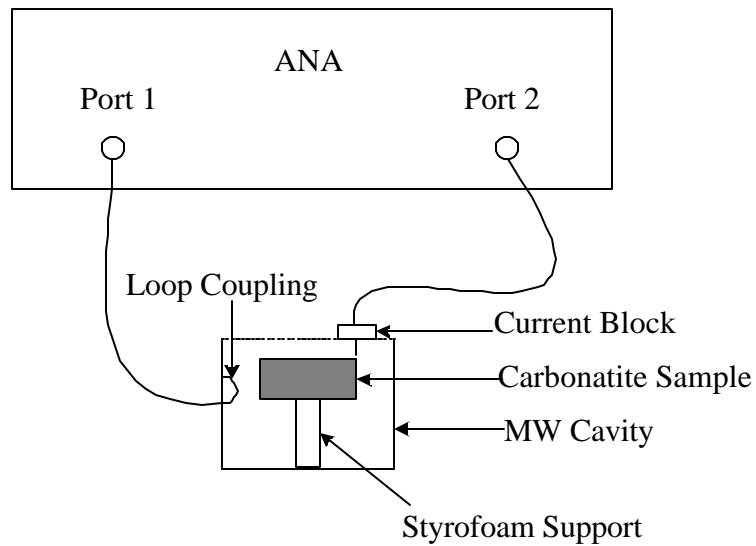


**Figure 6.2 - Measurement setup for cylindrical cavity probing**

The dimensions of the cylindrical microwave cavity used in the experiments are: *diameter - 94mm; height - 75mm.*

The cavity was loaded with the carbonatite slab, introduced in Section 4.3.2 - Figure 4.1, positioned *5mm* from the top of the cavity with the help of Styrofoam support (Figure 6.2). This enables interrogation of the E-field close to the material. The cylinder was covered with a metal grid with an array of holes, each *3mm* in diameter. The following figure shows the cavity, metal grid and semi-rigid coaxial probe (field-probe).

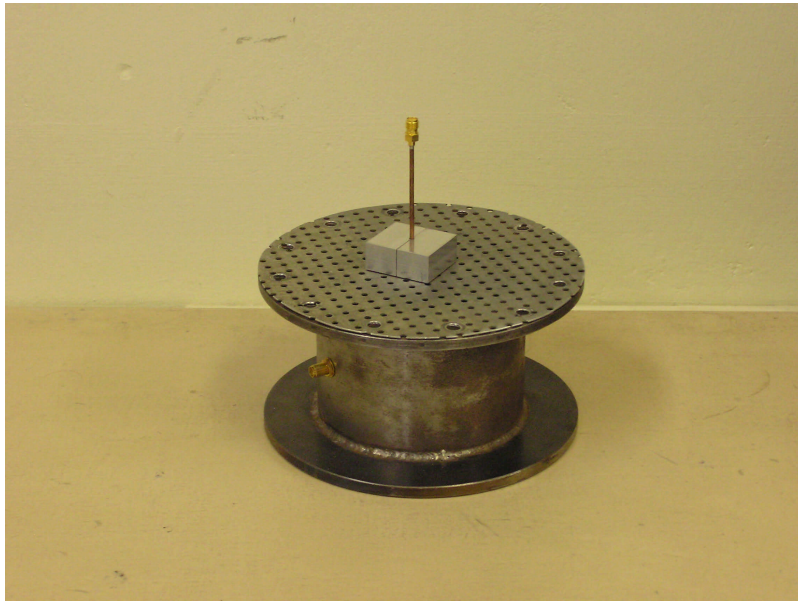


**Figure 6.3 - Cylindrical cavity and probe**

Port 1 of the ANA is connected to an *SMA* connector in the middle of the cylinder (Figure 6.3). The centre conductor of the *SMA* connector extends on the inside of the cavity and is bent back to form a loop (Figure 6.2). When excited, this forms a current loop that generates modes inside the cavity. It was shown by Pozar [12] that the dominant *TM* mode supported by a general cylindrical *WG* is the  $TM_{010}$  mode.

The holes in the metal grid are small enough (*diameter*  $< \lambda/20$ ) so that no, or very little energy escapes through them. To prevent current from leaking out at the sides of the grid, a braided wire was placed around the perimeter of the metal disc.

The field-probe consists of a length of semi-rigid coaxial cable, 2.5 mm in diameter, with the centre conductor protruding 3 mm from the end of the cable. When probing the cavity, the outer conductor of the probe should end flush with the inside of the metal grid and fit tightly into the hole. This ideal setup is shown in the following figure.

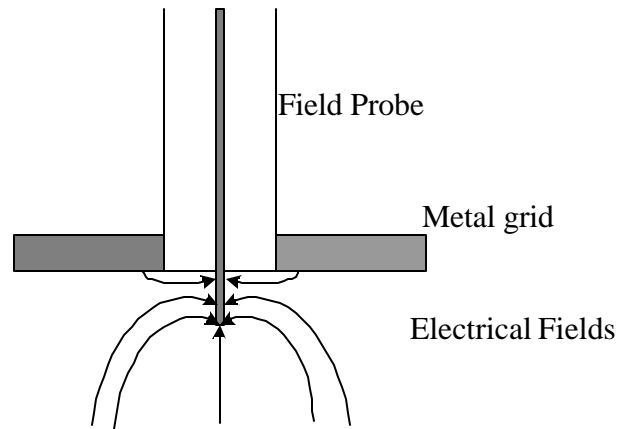


**Figure 6.4 - Ideal setup for field-probing**

This setup will ensure that only the centre conductor interrogates the fields and prevents common mode current from leaking out through the outer conductor of the probe. When probing the cavity, electrical fields bend toward the centre conductor and terminate on it. This registers as an  $S_{21}$  measurement on the ANA. If the probe centre conductor is too short the signal to noise ( $S/N$ ) ratio of the measurement is small and only noise is measured. Conversely, if the centre conductor is too long, the E-field is disturbed greatly. Instead of determining a point specific E-field it is integrated over the length of the probe resulting in a cumulative value. To help keep the centre conductor as short as possible the power level of the ANA was increased from  $0dBm$  to  $20dBm$ . The correct length was decided after  $S_{21}$  was measured for different lengths of centre conductor and repeatable measurements could be made.

However, the ideal measurement setup of Figure 6.4 was not possible since the field-probe does not fit tightly into the mesh holes and right-angled positioning of the probe with the mesh was difficult. To prevent common mode current induction, a current block (consisting of two aluminum blocks connected with adjustable screws and underlined with a resistive braiding) was fitted tightly around the outer conductor at the end of the probe. The metal block also helps with the vertical positioning of the field-probe. Without the aluminium block measurements were not repeatable. Empty cavity field comparisons can be found in Appendix B and will serve as a validation of the probing technique.

Another alternative to prevent common mode current induction may be to use a bazooka balun. The problem is that a bazooka balun is a narrowband structure. The resonant frequency for different loads inside the cavity will vary. It will therefore be necessary to design a new bazooka balun for different loads and it does not help with the vertical positioning of the probe.

### 6.3 Simulation Models

The simulation model of the carbonatite slab placed at the top of the cavity is presented in the figure below.

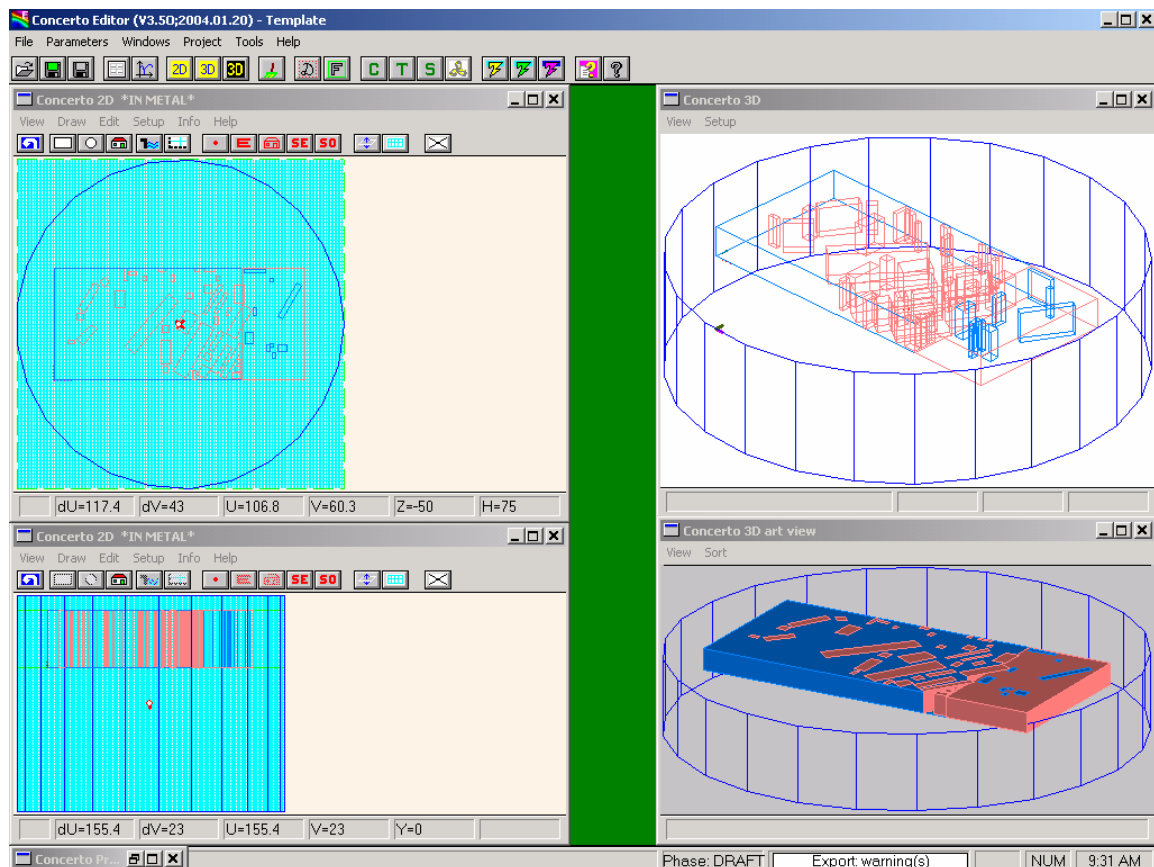


**Figure 6.5 - Simulation model of carbonatite slab at the top of the cylindrical cavity**

The loop excitation (inducing the  $TM_{010}$  mode in the empty cavity) is represented by a point source in the model. One of two options can be used which will induce the  $TM_{010}$  mode in the empty cavity. The point source can be positioned close to the side-wall and

specified to excite the  $H_x$  or  $H_y$ -field component, depending on where in the plane it is positioned. This would be the direct equivalent of the loop excitation. Alternatively, the point source can be positioned volumetrically in the middle of the cavity, and specified to excite the  $E_z$ -field component. The latter option was chosen since the  $H$ -field excitation takes very long to converge.

Before viewing field patterns, the resonance of the simulation model should be checked against the measured  $S_{11}$ -parameter. When working with a point source, this is done by a method called frequency-domain probing (*FD-probing*) in Concerto<sup>®</sup> [41]. After the simulation model resonant frequencies are identified (should be close to, or the same as the measured resonant frequencies), the field distribution can be viewed at the frequency of interest and compared with the measured field plot. To compare the equivalent simulated  $E$ -field with measurement, the magnitude of the  $E_z$ -field component is viewed at a depth of approximately 3 mm.

## **6.4 Field Plots: Experimental vs. Simulation**

The S-parameter comparisons between experiments and different simulation models that were done in Chapter 5 contained no detailed information on the interaction of the electromagnetic field with the different phases in the load. To investigate the electric field distribution in the vicinity of a multiphase material would be of interest. Both homogeneous and two phase models of the mineral sample were created and the simulation field distributions investigated and compared to a measured field distribution. Note that in figures 6.6, 6.8 and 6.11 screen shots are displayed of simulated S-parameters. The scales on these figures are not clear, but they were used to determine resonant frequencies from point source excitations and the magnitude of these resonances are ignored. Resonant frequencies are recorded for every figure to aid interpretation.

### **6.4.1 Carbonatite at Top of Cavity**

#### **Homogeneous Model**

Experimental and simulation resonant frequencies are presented in the following figure.

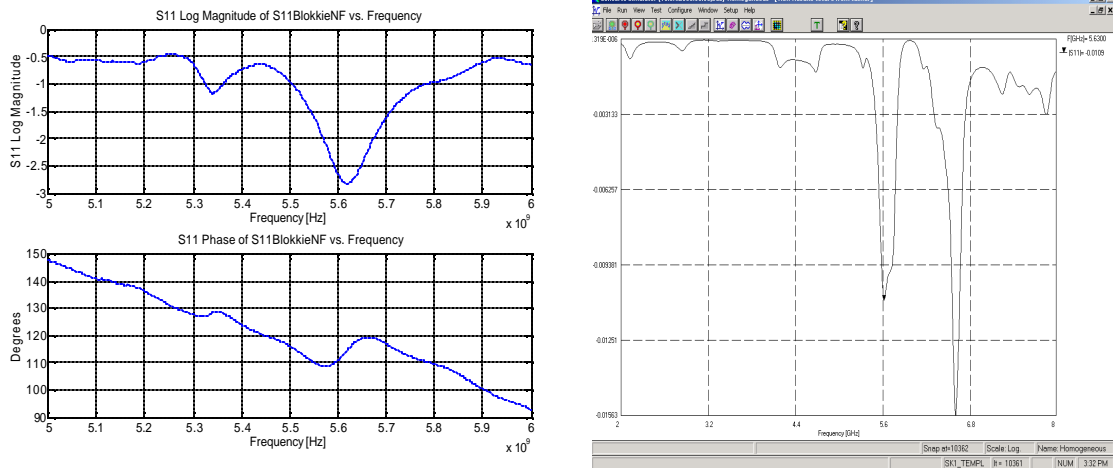


**Figure 6.6 - Experimental and simulation resonant frequencies respectively (Homogeneous model)**

According to experiment, the loaded cavity has a resonance at  $5.62 \text{ GHz}$ . The simulation (using the model presented in Figure 6.4, but with a homogeneous model of carbonatite; material properties as defined before) found a resonant frequency at  $5.63 \text{ GHz}$ . Simulation and experimental resonances are close to one another (within  $0.2\%$ ). The electric field distributions, at the measured and simulated resonant frequencies respectively, are presented in the figure below.

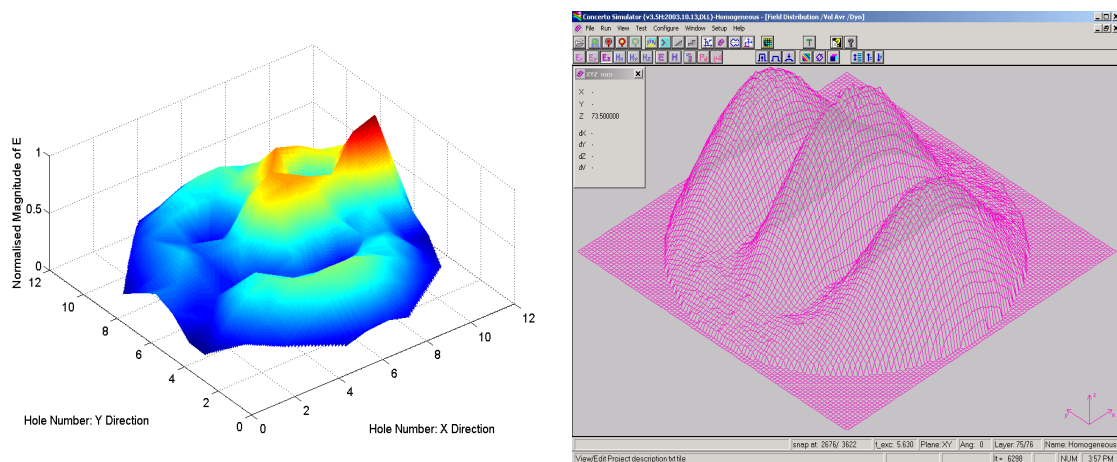


**Figure 6.7 - Ez-Field comparisons between experiment and homogeneous model of load respectively**

The measured field distribution is normalised to its maximum value. Both the experimental and simulation  $E_z$ -field distributions show three lobes across the surface. The measured distribution shows a disturbance at the lobe in the middle which is not

predicted by the homogeneous model of the load. No attempt at quantification of the comparison between experiment and simulation was made.

### Two Phase Model

The model and material properties used have been defined before and can be found in Section 5.5.2, Figure 5.11. Experimental and simulation resonant frequencies are presented in the figure below.

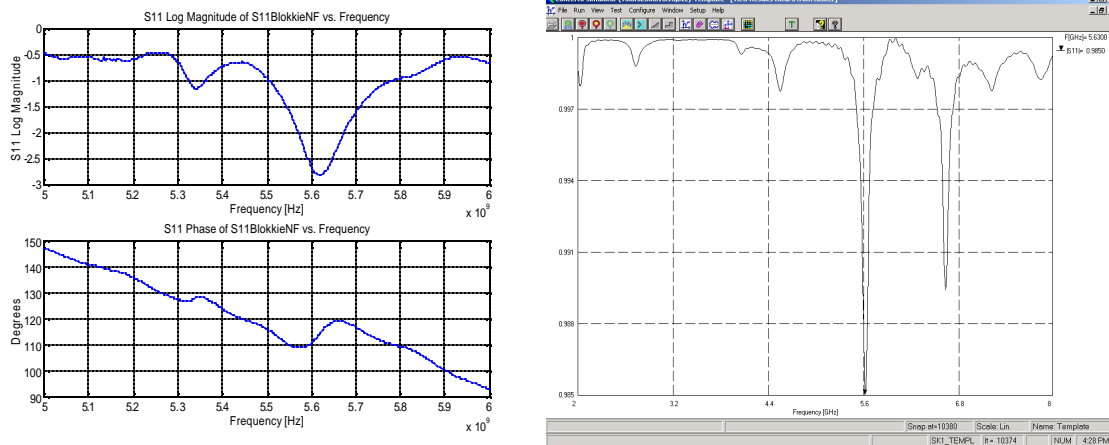


**Figure 6.8 - Experimental and simulation resonant frequencies respectively (Two Phase simulation model)**

Again the measured and simulated results show resonant frequencies at 5.62 and 5.63 GHz respectively (within 0.2% of one another). The field distributions at the respective frequencies are compared in the figure below.

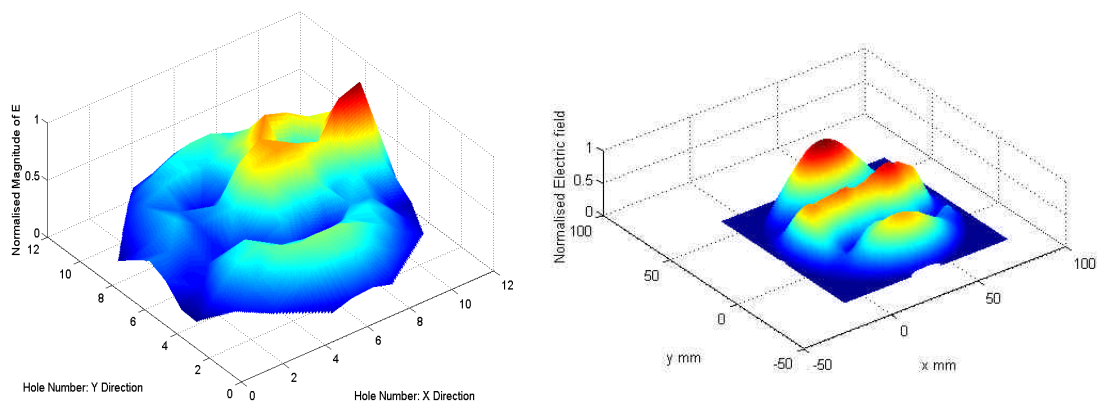


**Figure 6.9 - Ez-Field comparisons between experiment and two phase model of load respectively**



Note that both the measured and predicted field distributions are normalised to their maximum values for a direct comparison. The two phase model of the bad also predicts three lobes across the surface, and a disturbance at the right hand side of the centre lobe. The experimental distribution shows a maximum distortion on the right hand side of the centre lobe. The simulated distribution shows a similar distortion, but has a maximum on the middle of the upper lobe. However, comparison of Figures 6.7 and 6.9 shows that the two phase model gives a better prediction of the field distribution close to the rock surface.

### ***6.5 Field Probing Applied to an Industrial Cavity***

A prototype mineral processing applicator was designed through an iterative series of simulations to achieve a uniform power density over the cross section of the applicator when considering continuous flow of material. The design steps will not be outlined here, but the dimensions of the cavity can be found in Appendix C. The simulation model with carbon foam blocks at both ends is presented in the following figure.

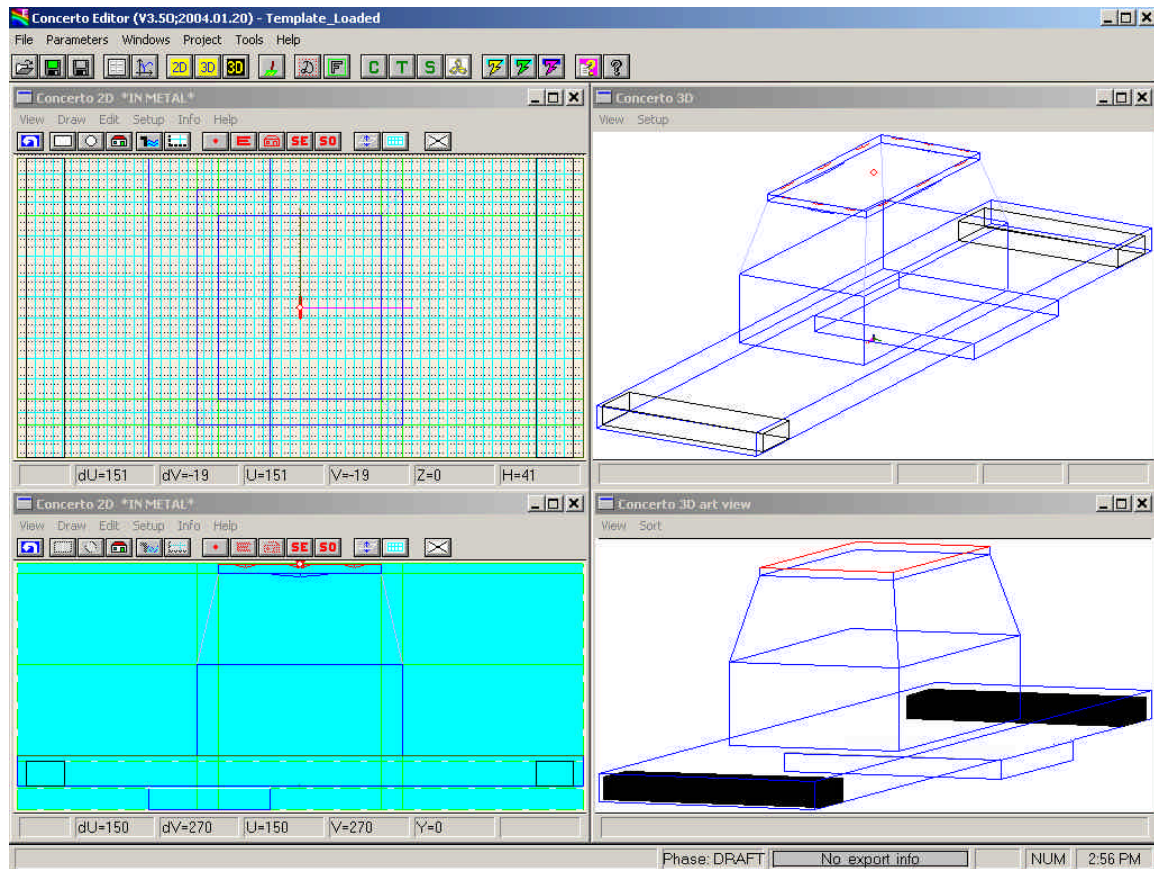


**Figure 6.10 – Simulation model of mineral processing applicator**

The cavity is fed with WR 340 from the top end. From there the feed opens into a tunnel that could support a conveyor belt system. The tunnel has a step at one end to achieve better uniformity in power density. For field probing purposes both ends of the tunnel were covered with metal plates, with a regular grid of holes drilled through it. Two blocks of carbon foam were placed at the end of the tunnel. The same principles as described for the cylindrical cavity are applicable for probing of the tunnel applicator. The measurement setup is shown in the following figure.

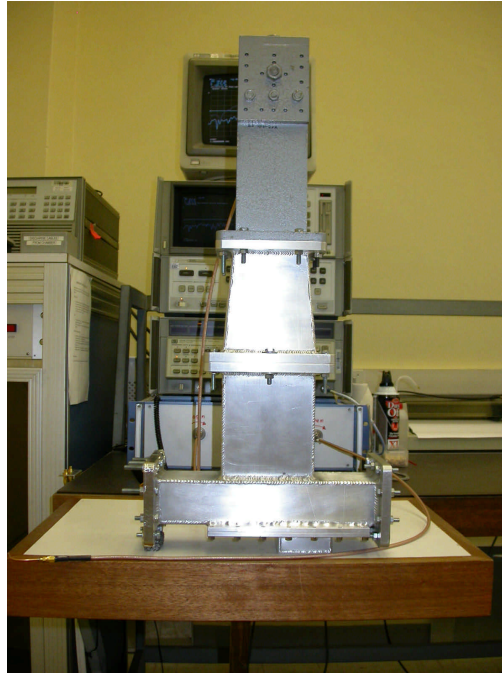


Figure 6.12 – Measurement setup for field probing of tunnel applicator

The measured and simulated  $S_{11}$ -parameters were compared and are shown below.

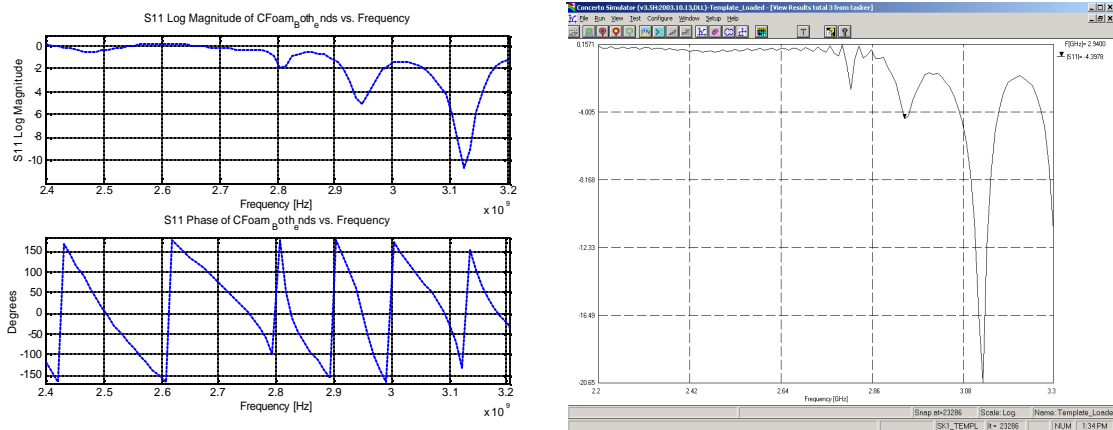


Figure 6.11 – Experimental and simulation  $S_{11}$  comparison of loaded tunnel applicator

Three resonant frequencies were found by experiment and simulation and are as follows:

**Measured  $S_{11}$ :** Resonance found at 2.805GHz, 2.95GHz and 3.125GHz

**Simulated  $S_{11}$ :** Resonance found at 2.81GHz, 2.94GHz and 3.13GHz

The simulation resonances agree to within  $0.4\%$  of the measured resonant frequencies.

The measured and simulated field-plots at  $3.125\text{ GHz}$  and  $3.13\text{ GHz}$  respectively, at the step end of the tunnel *and* parallel with the long axis of the tunnel (i.e.  $E_x$ -field component) are presented in the following figure. No quantitative comparison will be made here.

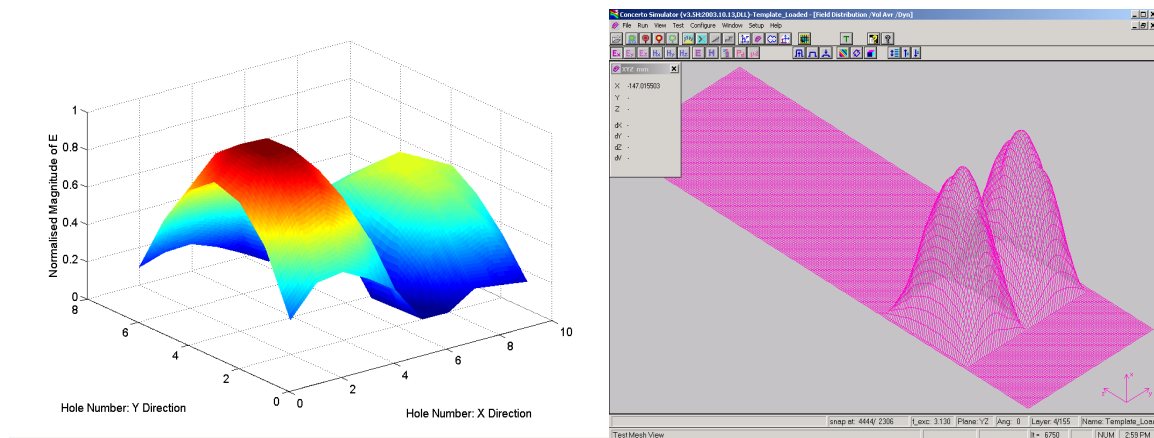


**Figure 6.13 – Experiment and simulation comparative  $E_x$ -field distributions; step end of applicator**

Note that the simulation field distribution is shown in relation to the dimensions of the rest of the applicator and therefore appears to be out of proportion. The magnitudes of the lobes in the measured field distribution are not equal. However, the two modes predicted by simulation are measured by the field-probe. This corresponds to a  $TM_{21p}$  mode, where  $p$  indicates any number of field variations down the length of the tunnel. It must be noted that the boundary conditions for the electric field (must be zero parallel to a metal wall) are not shown in the measured field distribution. This is because probing was done at a finite distance from the lateral walls.

Comparison of the simulation field distributions at the end of the tunnel loaded with carbon foam and empty, shows little or no difference. Results are presented in the following figure.

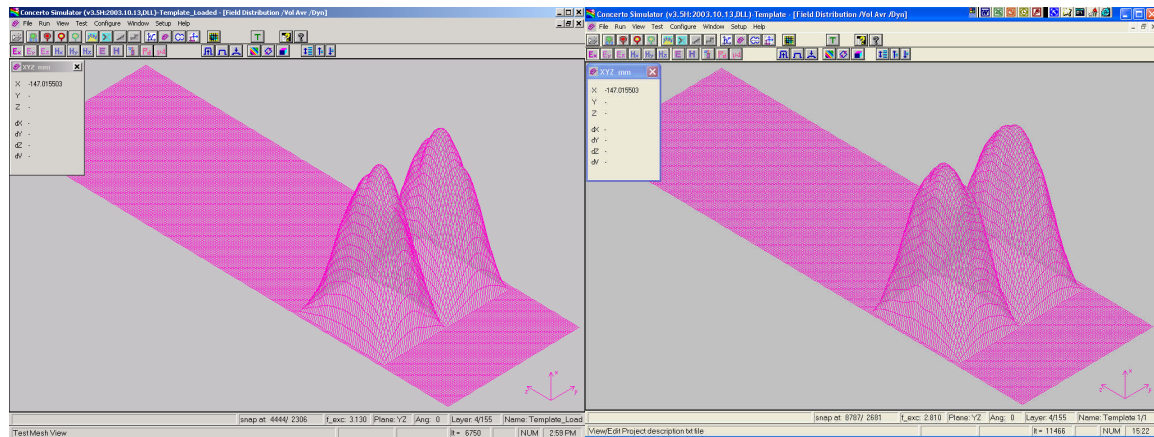


**Figure 6.14 – Loaded and empty cavity  $E_x$  field distribution at the face of the tunnel; step end of applicator**

This shows that the mode at the end faces seem to have settled down after a certain number of guide wavelengths away from the feed region. It indicates that the behaviour of the field distribution *at the end faces* might be dominated by the cavity and not the load.

It would be more interesting to probe the tunnel applicator close to the middle active region. This was not done here since it would require drilling holes into the tunnel itself. High power measurements are still to be made with the cavity and holes inside the tunnel could jeopardise the safety of the system.

## 6.6 Conclusion

Resonant frequencies of a cylindrical cavity, loaded with a mineral sample close to the top were measured and predicted by simulation models. Cavity field-probing was introduced and applied to the relevant applicator. The measured field-distribution was compared with simulated field distributions of both homogeneous and two phase models of the rock. It was shown that the field distribution, using the two phase model, was more realistic than the field-distribution using the homogeneous model. This illustrates the importance of accurate model representation of multiphase materials when determining field stress in and around different phases.

The same probing principles were applied to an industrial system. The field distribution predicted by simulation was measured by field probing. The end faces probed did not show interesting results however, but the distribution seems to be dominated by the cavity and not the load. Unfortunately probing in the active region of the applicator was not possible due to safety concerns for high power measurements still to be made.

The results presented here do show that simulated field distributions can be trusted but accurate representation of the load is important.

# Chapter 7

## Conclusion and Recommendations

---

### 7.1 Conclusion

In this thesis the process of multiphase material property determination and *FDTD* simulation model representation has been presented. A flanged coaxial probe and a *WG* measurement system have been used to determine permittivity and permeability. These properties were used in various simulation models. Both materials measurements and iterative simulations contributed to accurate model representation of a multiphase ore. An applicator was also built and its field distribution was determined via a field probing technique. This illustrated the importance of accurate model representation of multiphase materials. This work hopes to contribute to microwave assisted comminution.

The coaxial probe uses a lumped model and applied the inversion technique developed by Stuchly and Stuchly [9]. It was found that, after calibration at the plane of measurement, that the probe has an internal fringing capacitance which is a function of the material under test. This capacitance introduces an additional phase shift into the measurement, but the measured material properties agree within 10% compared to a full wave inversion technique. Compared to a reference material the probe produced accurate results, but cannot measure low loss factors or conductive materials.

The *WG* measurements utilised the Nicholson and Ross [32] and Weir [16] inversion algorithm. An *n*-factor correction, suggested by Cloete [34], was applied to account for a mathematical ambiguity in the inversion technique. There is an area of high uncertainty when the wavelength inside the sample approaches a half wavelength. When measuring inhomogeneous materials higher order modes *could* be excited by the sample and produce unrealistic results. The inversion code tested for this possibility. Using a

reference material, the *WG* measurement technique was found to produce accurate results, but it cannot measure low loss factors or conductive materials.

The measured material properties were implemented in *FDTD* simulation models and an S-parameter comparison was made between measurements and simulations. The *WG* measurement system and a single mode cylindrical cavity were modelled with both solid and crushed ore. The S-parameters were extracted and compared to measurements. It was found after iterative simulations that material properties of the ore were determined accurately, but vary strongly as a function of geometrical representation. Different models inside the different cavities showed agreement (or disagreement) with measured results in the range of 5 – 200%. This illustrates the fact that accurate simulation model representation becomes important for multiphase materials.

A field probing technique was exploited and simulations and experimental field distributions were compared. It was shown that accurate simulation model representation of multiphase materials becomes especially important in the determination of power densities in and around different rock phases.

In conjunction with work that is being conducted at Nottingham University this thesis is done as part of a project sponsored by AMIRA and is expected to make a valuable contribution in the investigation of microwave mineral processing.

## **7.2 Recommendations**

Materials property measurement and accurate representation of two phase materials in *FDTD* simulations have been the main focus of this thesis. The field distribution of a prototype microwave mineral cavity has also been measured. Both measurement and modelling described here have limitations and details will be discussed next.

The *WG* and coaxial probe measurement systems are of the reflection-transmission kind and it was found that both measure the dielectric constant (and real part of permeability



for the *WG* system) reliably. However, dielectric and magnetic loss factors of low loss materials cannot be determined accurately. Resonant measurement techniques should be exploited to measure the loss factors of low loss materials. Measurement of conductivity was not possible and techniques to accomplish this should be investigated.

The *WG* matched load standard introduces an unwanted reflection during calibration. This should be eliminated by using a higher loss material in the design of the *WG* matched load, or by using time domain gating on the off line data during calibration.

The measurement of some solid mineral ore displayed a unrealistic strong diamagnetic effect. This should be investigated to determine whether it is a physical property of the sample or not. One possible means of doing this would be to produce an artificial diamagnetic material as was done by Haus and Melcher [36] and to measure it with the *WG* system and compare results with relevant simulations.

More simulations should be conducted to establish a better relationship between the simulation models' geometrical representation of multiphase materials and their material properties. Two possible means of pursuing this would be to use mixing rules [44] and/or genetic algorithms [45]. This approach is not unknown and Wäppling-Raaholt et al. [46] used a retro-modelling approach similar to genetic algorithms to determine the permittivity of inhomogeneous materials.

Simulation results of the cylindrical single mode cavity showed a shift in frequency. Further investigations could test to see whether this is a function of discretization or incorrect material properties or both of these factors.

The field distribution in the vicinity of the rock sample was measured and compared with simulation results. Only a visual comparison was done and a technique should be investigated or developed to quantify the comparison. The power density in and around different phases should be determined from simulation data and used in thermal stress

modelling. This could predict the nature of stress fractures between different phases and can be used as a design parameter for *MW* cavities with the view to mineral processing.

## Bibliography:

- [1] J.M. Osepchuk, "A History of Microwave Heating Applications," *IEEE Transactions on Microwave Theory and Techniques*, vol. MTT – 32, no. 9, pp. 1200 – 1223, September 1984.
- [2] A.C. Metaxas, "Applicators for Industrial Microwave Processing," *Microwaves: Theory and Application in Materials Processing II, Ceramic Transactions*, vol. 36, pp. 549 – 562, April 1993.
- [3] A.C. Metaxas, "Microwave Heating," *Power Engineering Journal*, pp. 237 – 247, September 1991.
- [4] A.C. Metaxas and R.J. Meredith, *Industrial Microwave Heating*, Peter Peregrinus Ltd., 1983.
- [5] R. Meredith, *Engineers' Handbook of Industrial Microwave Heating*, The Institution of Electrical Engineers, 1998.
- [6] H. Püschner, *Heating with Microwaves*, N.V. Philips' Gloeilampenfabrieken, 1966.
- [7] T.V.C.T. Chan and H.C. Reader, *Understanding Microwave Heating Cavities*, Artech House Publishers, 2000.
- [8] S.W. Kingman, K. Jackson, A. Cumbane, S.M. Bradshaw, N.A. Rowson and R. Greenwood, "Recent developments in microwave-assisted comminution," *International Journal of Mineral Processing*, Article in Press, September 2003.
- [9] M.A. Stuchly and S.S. Stuchly, "Coaxial Line Reflection Methods for Measuring Dielectric Properties of Biological Substances at Radio and Microwave Frequencies – A Review," *IEEE Transactions on Instrumentation and Measurement*, vol. IM-29, no. 3, pp. 176 – 183, September 1980.
- [10] M. Rimbi, *Wood Microwave Dielectric Heating and Measurement of Material Properties*, PhD Dissertation, Department of Electrical and Electronic Engineering, University of Stellenbosch, 2004.
- [11] H. Zhang and A.K. Datta, "Coupled Electromagnetic and Thermal Modelling of Microwave Oven Heating of Foods," *Journal of Microwave Power and Electromagnetic Energy*, vol. 35, no. 2, pp. 71 – 85, 2000.
- [12] D.M. Pozar, *Microwave Engineering*, John Wiley & Sons Inc., 2<sup>nd</sup> edition, 1998.

- [13] N. Braithwaite and G. Weaver, *Electronic Materials*, Butterworth Heinemann, 1998.
- [14] J.H. Cloete, *Unpublished Lecture Notes as Part of the Engineering Materials 244 Course*, Department of Electrical and Electronic Engineering, University of Stellenbosch, 1999.
- [15] A. von Hippel, *Dielectrics and Waves*, Artech House, 1995.
- [16] W.B. Weir, "Automatic Measurement of Complex Dielectric Constant and Permeability at Microwave Frequencies," *Proceedings of the IEEE*, vol. 62, no. 1, pp. 33 – 36, January 1974.
- [17] T.W. Athey, M.A. Stuchly and S.S. Stuchly, "Measurement of Radio Frequency Permittivity of Biological Tissues with an Open-Ended Coaxial Line: Part 1," *IEEE Transactions on Microwave Theory and Techniques*, vol. MTT-30, no. 1, pp. 82 – 86, January 1982.
- [18] G.Q. Jiang, W.H. Wong, E.Y. Raskovich, W.G. Clark, W.A. Hines and J. Sanny, "Open-ended coaxial-line technique for the measurement of the microwave dielectric constant for low-loss solids and liquids," *Rev. Sci. Instrum.*, vol. 64, no. 6, pp. 1614 – 1621, June 1993.
- [19] M. Arai, J.G.P. Binner, G.E. Carr and T.E. Cross, "High Temperature Dielectric Property Measurements of Engineering Ceramics," *Microwaves: Theory and Application in Materials Processing II, Ceramic Transactions*, vol. 36, pp. 483 – 492, April 1993.
- [20] A. von Hippel, *Dielectric Materials and Applications*, The M.I.T. Press, 1961.
- [21] Network Analysis, "Specifying Calibration Standards for the HP 8510 Network Analyzer," *Hewlett Packard Product Note 8510-5A*.
- [22] Materials Measurement, "Measuring the Dielectric Constant of Solids with the HP 8510 Network Analyzer," *Hewlett Packard Product Note 8510-3*.
- [23] P. Guillon, "Microwave Techniques for Measuring Complex Permittivity and Permeability of Materials," *Materials Research Society Symposium Proceedings*, vol. 347, pp. 203 – 208, 1994.
- [24] M. Bingle and D.F. Pansegrouw, *A Coaxial System for Measuring the Complex Permittivity of Fluids and Gels at 1 – 12 GHz*, Internal Report, Department of Electrical and Electronic Engineering, University of Stellenbosch, May 1997.

- [25] A.G. Smith, *An Experimental Study of Artificial isotropic Chiral Media at Microwave Frequencies*, PhD Dissertation, Department of Electrical and Electronic Engineering, University of Stellenbosch, 1998.
- [26] N. Marcuvitz, *Waveguide Handbook*, Peter Peregrinus Ltd., 1986.
- [27] W.B. Westphal, "Distributed Circuits," A. von Hippel, *Dielectric Materials and Application*, The M.I.T. Press, pp. 68 – 70, 1961.
- [28] J. Baker-Jarvis, M.D. Janezic, P.D. Domich and R.G. Geyer, "Analysis of an Open-Ended Coaxial Probe with Lift-Off for Nondestructive Testing," *IEEE Transactions on Instrumentation and Measurement*, vol. 43, no. 5, pp. 711 – 717, October 1994.
- [29] W.J. Louw, *Mikrogolf Dielektriese Eienskap Meting van Minerale*, Unpublished report as partial fulfilment of the requirements of the course Project (E) 448 for the Degree Baccalaurean in Engineering, Department of Electrical and Electronic Engineering, University of Stellenbosch, November 2002.
- [30] C. Fouché, *Measurement of the Dielectric Properties of Materials*, Unpublished report as partial fulfilment of the requirements of the course Project (E) 448 for the Degree Baccalaurean in Engineering, Department of Electrical and Electronic Engineering, University of Stellenbosch, June 2004.
- [31] Kraus and Fleisch, *Electromagnetics with Applications*, McGraw-Hill, 5<sup>th</sup> edition, 1999.
- [32] A.M. Nicholson and G.F. Ross, "Measurement of the Intrinsic Properties of Materials by Time Domain Techniques," *IEEE Transactions on Instrumentation and Measurement*, vol. IM-19, pp. 377 – 382, November 1970.
- [33] J. Baker-Jarvis, M.D. Janezic, J.H. Grosvenor, Jr. and R.G. Geyer, "Transmission/Reflection and Short Circuit Line Methods for Measuring Permittivity and Permeability," *NIST Technical Note 1355-R*, pp. 15 – 51, December 1993.
- [34] J.H. Cloete, "High Precision Measurement of Complex Permittivity and Permeability at Microwave Frequencies," *IEEE Symposium on Antennas and Propagation and Microwave Theory and Techniques*, vol. AP/MTTS – 90 Proceedings, pp. 365 – 369, August 1990
- [35] C.J. van der Merwe, *Uniform Multiconductor Transmission Lines Above a Dissipative Earth: Direct FDTD Analysis and Experimental Validation*, PhD dissertation, Department of Electrical and Electronic Engineering, University of Stellenbosch, December 1998.

- [36] H.A. Haus and J.R. Melcher, *Electromagnetic Fields and Energy*, The M.I.T. Press, 1998.
- [37] R.T. Shuey, *Semiconducting Ore Materials*, Elsevier Scientific Publishing Company, pp. 371 – 388, 1975.
- [38] Kansas Geological Survey, “Modelling Dielectric Constant Values of Geological Materials: An Aid to Ground-Penetrating Radar Data Collection and Interpretation,” <http://www.kgs.ukans.edu/Current/2001/martinez/martinez2.html>, 2001.
- [39] D.B. Davidson, *Computational Electromagnetics for RF and Microwave Engineering*, Cambridge University Press, Chapter 1, 2005.
- [40] A. Taflove and S.C. Hagness, *Computational Electrodynamics: The Finite-Difference Time-Domain Method*, Artech House, 2<sup>nd</sup> edition, 2000.
- [41] Concerto<sup>®</sup> User’s Guide, Vector Fields<sup>®</sup> Limited, 24 Bankside, Kidlington, Oxford OX5 1JE, England, December 2003.
- [42] D.B. Davidson, *Numerical Analysis of Microstrip Antennas*, Paper presented during the Microstrip Antenna Analysis and Design Short Course, Department of Electrical and Electronic Engineering, University of Stellenbosch, November 1996.
- [43] C. van der Merwe, *’n Studie van Silindriese Holte Mikrogolf Toevoegers*, Unpublished report as partial fulfilment of the requirements of the course Project (E) 448 for the Degree Baccalaurean in Engineering, Department of Electrical and Electronic Engineering, University of Stellenbosch, December 2004.
- [44] W.R. Tinga and W.A.G. Voss, “Generalized Approach to Multiphase Dielectric Mixture Theory,” *Journal of Applied Physics*, vol. 44, no. 9, pp. 3897 – 3902, September 1973.
- [45] E. Michielssen, Y Rahmat-Samii and D.S. Wiele, “Electromagnetic System Design Using Genetic Algorithms,” M.A. Stuchly, *Modern Radio Science 1999*, Oxford University Press, pp. 91 – 123, 1999.
- [46] B. Wäppling-Raaholt and P.O. Rismann, “Permittivity Determination of Inhomogeneous Items by Retro-Modelling with a Degenerate Mode Cavity,” *9th International Conference on Microwave and High Frequency Heating*, Loughborough, UK, 1-5 September.

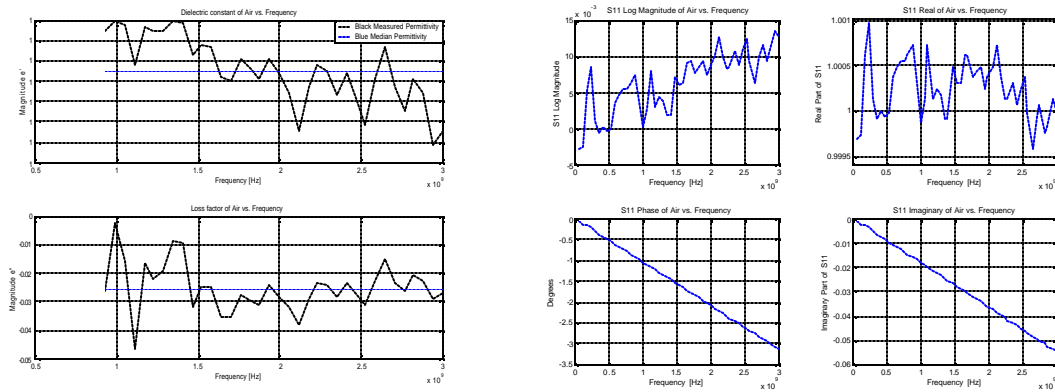
## Appendix A

### Material Properties and Measured S-Parameters

This Appendix presents additional results of measurements made by both the coaxial probe and *WG* measurement systems on various materials. Some known materials will serve as a verification of the measurement systems. Results on carbon foam and rock samples are also included to support the results and discussions in Chapter 4. Results can be analysed in the same manner as in Sections 4.5 and 4.6. Where required, for analytical purposes, the measured S-parameters are also included. Unless stated otherwise literature values in this section are quoted from [Metaxas and Meredith].

#### A.1 Coaxial Probe Measurements

##### Air

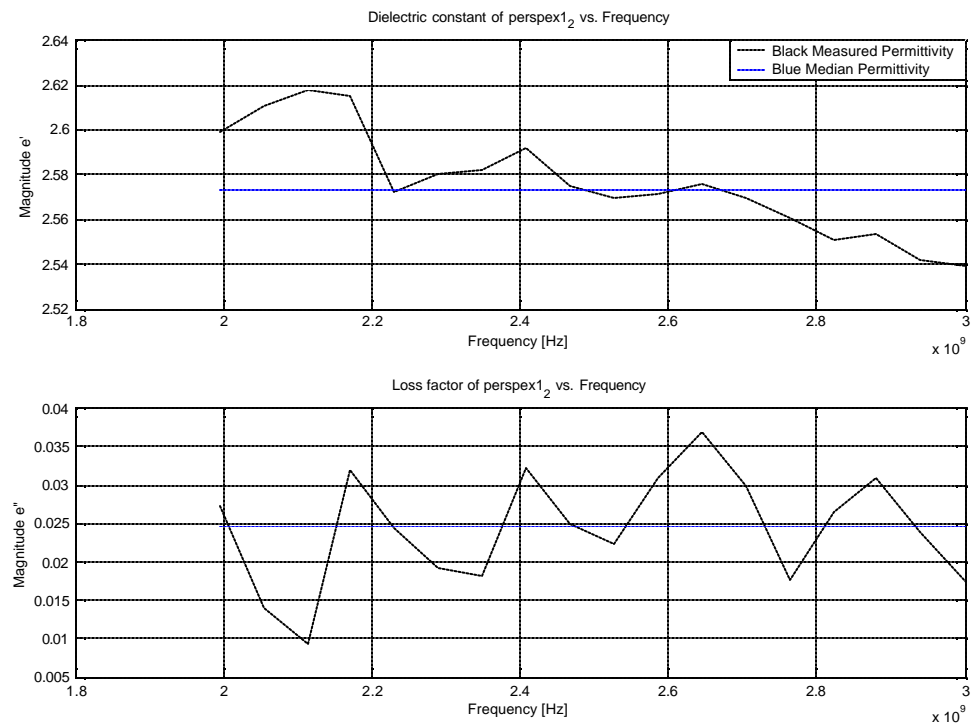


Material	$\epsilon_r'$ (Probe)	$\epsilon_r''$ (Probe)	$\epsilon_r'$ (Literature)	$\epsilon_r''$ (Literature)
Air	1	-0.025	1	0

Figure A.1 - Dielectric constant and loss factor of Air as measured with the coaxial probe

It can be seen from (3.5) that if the magnitude of the measured  $S_{11}$  is bigger than  $0 \text{ dB}$  it will results in a loss factor smaller than  $0$ . This is shown in Figure A.1.

**Perspex**

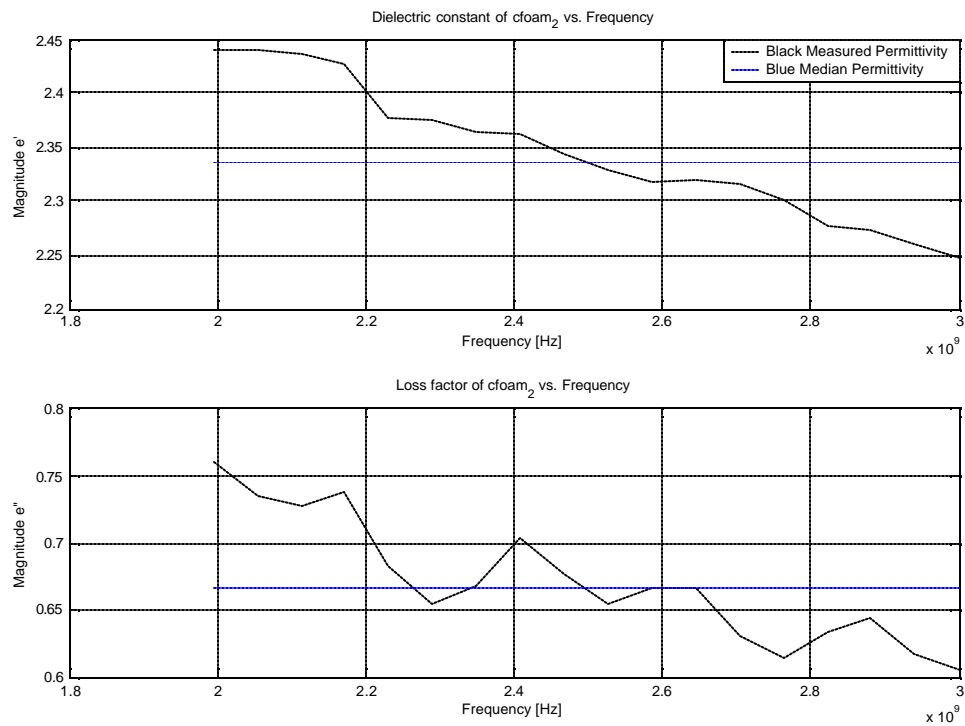


Material	$e_r'$ (Probe)	$e_r''$ (Probe)	$e_r'$ (Literature)	$e_r''$ (Literature)
Perspex	2.57	0.025	2.60	0.015

Figure A.2 - Dielectric constant and loss factor of Perspex as measured with the coaxial probe



### Carbon Foam

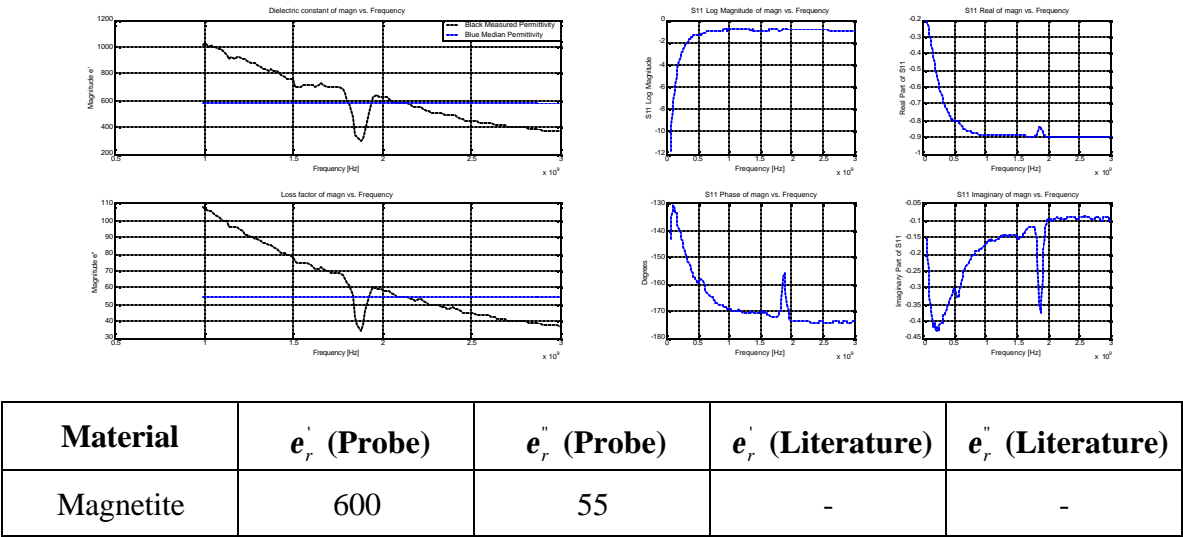


Material	$e'_r$ (Probe)	$e''_r$ (Probe)	$e'_r$ (Literature)	$e''_r$ (Literature)
Carbon Foam	2.33	0.67	-	-

**Figure A.3 - Dielectric constant and loss factor of carbon foam as measured with the coaxial probe**

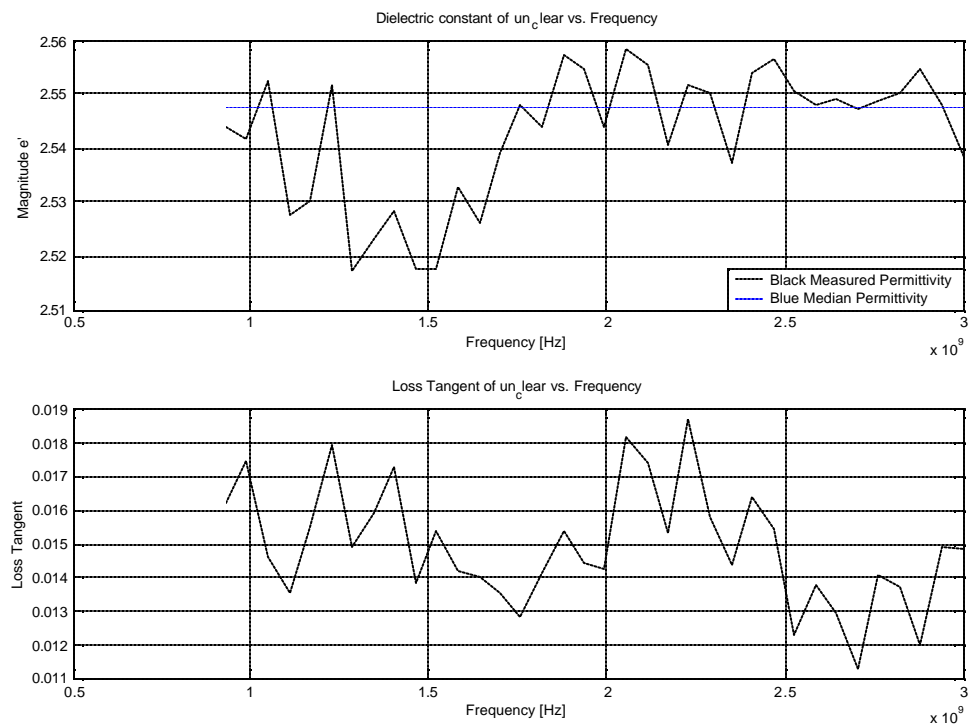
No reference is available for the carbon foam as this is an in house material. However results can be compared to *WG* measurement.

**Magnetite**



**Figure A.4 - Dielectric constant and loss factor of magnetite as measured with the coaxial probe**

From Figure A.4 the magnitude of  $S_{11}$  is measured as -1 dB and the angle is between 170 and 180 degrees above 1 GHz across the band. This is similar to the behaviour of a short circuit which will measure  $|S_{11}| = 0$  dB and  $\angle -180^\circ$  across the band.

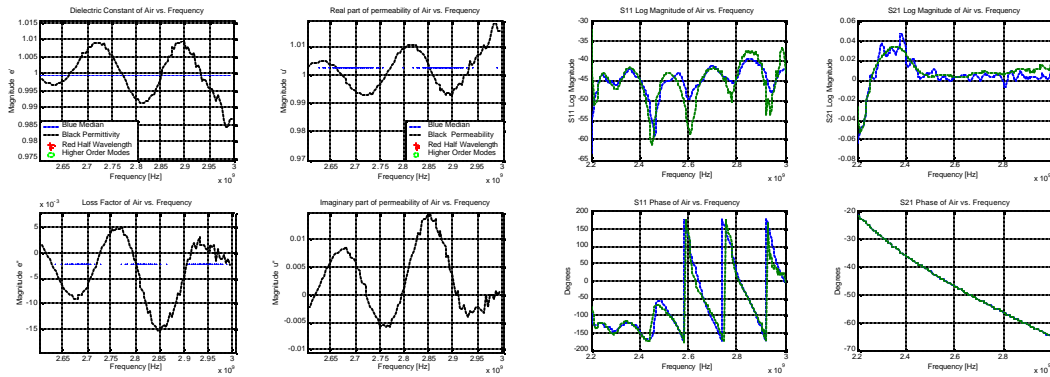
**A Probe Measurement with a High Quality Phase Stable Cable****Figure A.5 – A probe measurement of a material with a high quality phase stable cable**

It can be seen from Figure A.5 that there is no drift in dielectric constant. The ripple in the results is due to measurement noise.

## A.2 WG Measurements and S-Parameters

All WG S-parameters are included since they help with the analysis of results. The S-parameter data include both the original measurement and the “smoothed” data.

### Air

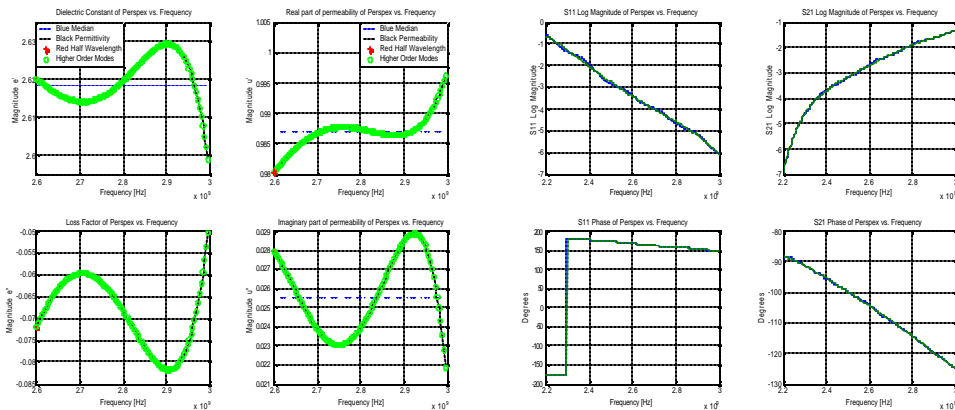


Material	$\epsilon_r'$	$\epsilon_r''$	$\mu_r'$	$\mu_r''$	$\epsilon_r'(\text{Lit})$	$\epsilon_r''(\text{Lit})$	$\mu_r'(\text{Lit})$	$\mu_r''(\text{Lit})$
Air	1	-0.002	1	0.001	1	0	1	0

Figure A.6 - Dielectric and magnetic properties of Air as measured with the WG system

The negative loss factor is because the measured  $S_{21}$  magnitude is bigger than 0.

**Perspex**



Material	$\epsilon_r'$	$\epsilon_r''$	$\mu_r'$	$\mu_r''$	$\epsilon_r'$ (Lit)	$\epsilon_r''$ (Lit)	$\mu_r'$ (Lit)	$\mu_r''$ (Lit)
Perspex	2.62	-0.067	0.99	0.026	2.6	0.015	1	0

Figure A.7 - Dielectric and magnetic properties of Perspex as measured with the WG system

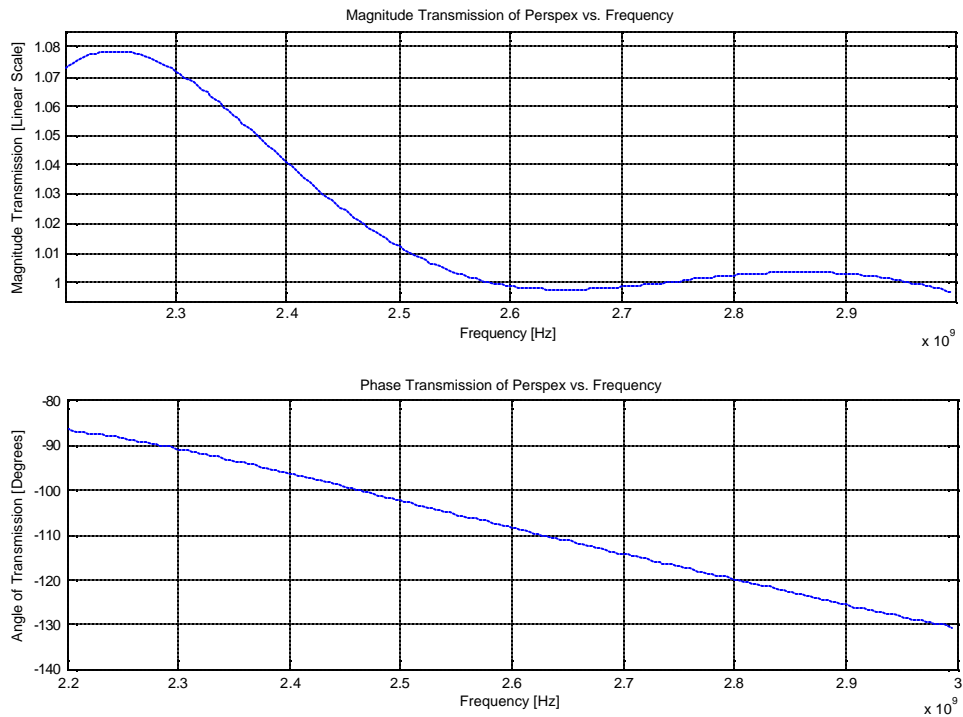
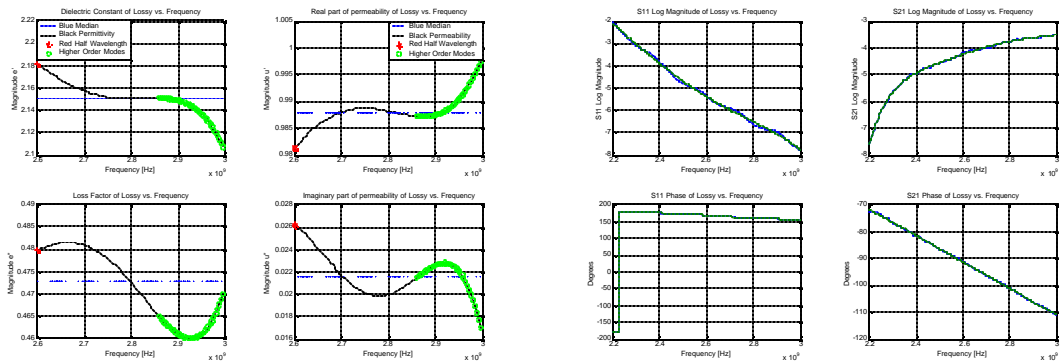


Figure A.8 - Transmission coefficient of Perspex as measured with the WG system

The negative loss factor is because the transmission coefficient (T) is bigger than 1 (Section 4.5.2).

**Carbon Foam**

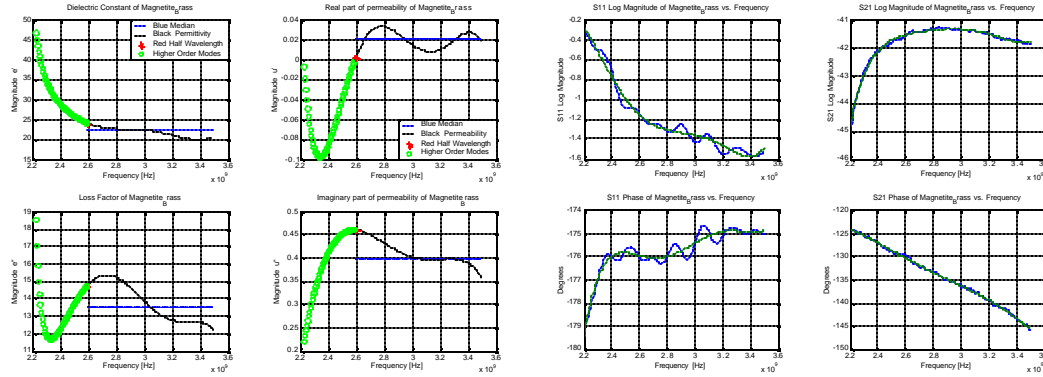


Material	$\epsilon_r'$	$\epsilon_r''$	$m_r'$	$m_r''$	$\epsilon_r'(\text{Lit})$	$\epsilon_r''(\text{Lit})$	$m_r'(\text{Lit})$	$m_r''(\text{Lit})$
Carbon Foam	2.15	0.473	0.99	0.022	-	-	-	-

**Figure A.9 - Dielectric and magnetic properties of carbon foam as measured with the WG system**

No reference available as this is an in house material. The WG results are lower than the probe measurements. This can be because the probe was pushed into the carbon foam, compressing its immediate surroundings and interrogating a more dense material.

## Magnetite



Material	$\epsilon_r'$	$\epsilon_r''$	$m_r'$	$m_r''$	$\epsilon_r'$ (Lit)	$\epsilon_r''$ (Lit)	$m_r'$ (Lit)	$m_r''$ (Lit)
Magnetite	23	13.6	0.02	0.4	-	-	100	-

**Figure A.10 - Dielectric and magnetic properties of magnetite as measured with the WG system**

The literature value for permeability is quoted from Haus and Melcher.

From the S-parameters it is clear that a short circuit behaviour is measured ( $|S_{11}| = 0$  dB and  $\angle -180^\circ$  across the band).

The following table shows extracted material properties of crushed ore for various experiments. The *median* values above 2.6 GHz are recorded.

**Table A.1 – Extracted material properties of three different experiments for crushed ore**

<b>Experiment</b>	<b>Parameters Used</b>	<b><math>\epsilon_r'</math></b>	<b><math>\epsilon_r''</math></b>	<b><math>m_r'</math></b>	<b><math>m_r''</math></b>
1	$S_{11}, S_{21}$	3.75	2.75	0.56	-0.432
1	$S_{22}, S_{12}$	4.21	-0.62	0.67	0.118
2	$S_{11}, S_{21}$	3.36	-0.025	0.979	0.077
2	$S_{22}, S_{12}$	3.48	-0.07	0.95	0.072
3	$S_{11}, S_{21}$	2.6	-0.72	1.15	0.39
3	$S_{22}, S_{12}$	2.71	0.49	1.25	-0.07

The table shows two sets of results for each experiment, depending on the set of parameters used. Refer to Sections 3.4.4 and 3.4.5 for a discussion on S-parameters sets and material properties.



## Appendix B

### Field Probing

---

This Appendix is included to validate the probing technique by comparing simulation and experimental field plots of the empty cylindrical cavity. The dominant resonance is found by S-parameter measurement and simulation. It is expected to be the  $TM_{010}$  mode.

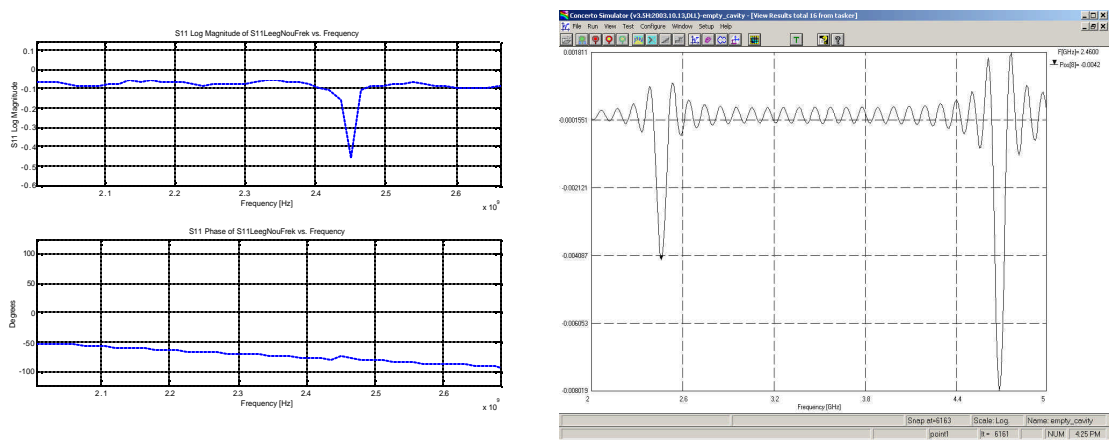


**Figure B.1 - Experimental and simulation resonant frequencies of empty cavity**

The dominant resonances found is  $2.45 \text{ GHz}$  experimentally and  $2.46 \text{ GHz}$  by simulation. Next the field distributions are presented. No attempt will be made here to make a quantified comparison.

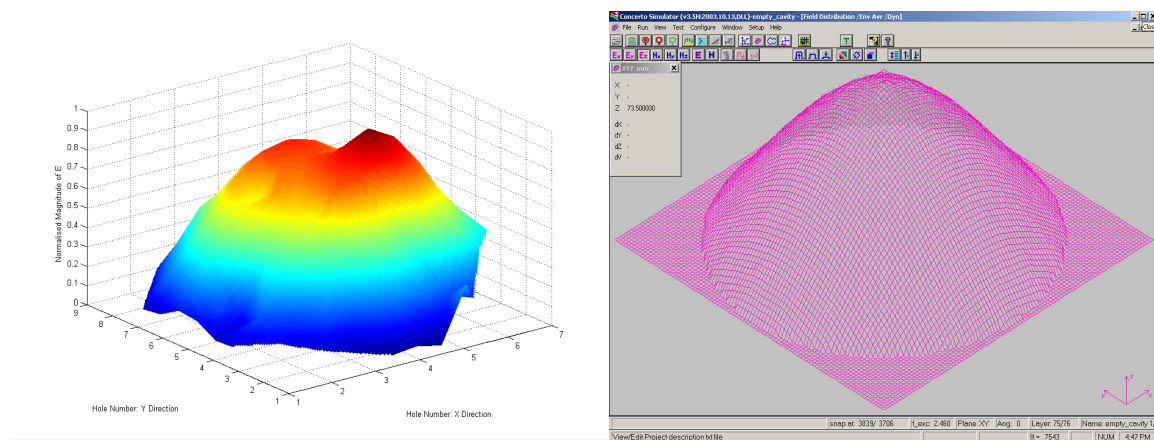


**Figure B.2 - Experimental and simulation  $TM_{010}$  field distribution**

The measured field distribution is normalised to its maximum. From Figure B.2 it is clear that both field probing and simulation displays the  $TM_{010}$  field distribution at the respective frequencies.

## Appendix C

### Dimensions of Tunnel Applicator

---

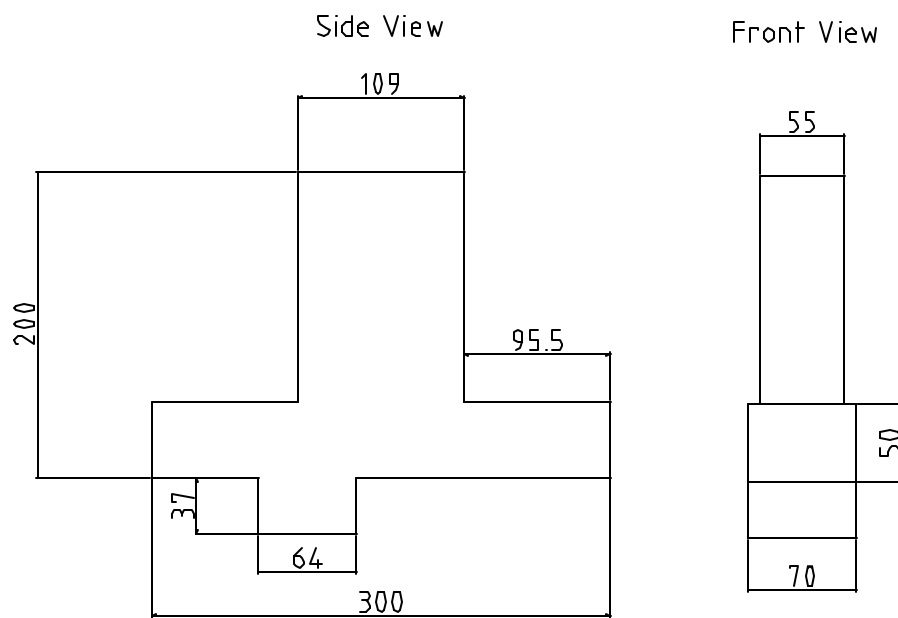


Figure C.1 – Dimensions of the tunnel applicator in mm

## Appendix D

### Matlab<sup>®</sup> Routines

---

#### Coaxial Probe Inversion Program

```
%-----%
% W.J. Louw

% Program that calculates the permittivity of a sample material using
% the s11 parameter as measured by a coaxial probe system. The original
% design for this system was proposed by Morris Rimbi as part of his
% PhD studies.
%
% Remember that this system is sensitive to thermal drift and cable
% movement. Data files must be in same directory as program.
%-----%

%-----DEFINE FUNCTION & SETUP MATLAB-----%

function extract(datafile, refdata) % User must input files
close all; % Close all graphs presently open.
format long g; % Convenient format for small numbers.

%-----%

%-----IMPORT S-PARAMETERS AND DEFINE CONSTANTS-----%

if (nargin < 2), refdata = 'Air'; end; % Check for reference other than air.

eval(datafile); %Load file with unknown dielectric property s11 data
eval(refdata); %Load file with known dielectric property s11 data

var = eval(strcat(refdata,'_s11(:)')); % s11 parameter of known material loaded from file.
s = abs(var); % Magnitude of s11 of known material
p = angle(var); % Angle in radians of known material
dphi = abs(p);
phase = (p*180)/pi; % Angle in degrees of known material

temp = eval(strcat(datafile,'_s11(:)')); % s11 parameter of sample material loaded from
file.
s11 = abs(temp); % Magnitude of s11 of unknown material
p11 = angle(temp); % Angle in radians of unknown material
phase11 = (p11.*180)./pi; % Angle in degrees of unknown material
```

```

%-----CONSTANTS-----%
f = linspace(Start, Stop, Points)'; % Frequency range divided into number of frequency
points
w = (2*pi).*f;          % Radian freq
z = 50;                 % Characteristic impedance is 50 ohm.
b = (1.28/2)*10^-3;     % Radius of inner conductor
a = (4.1/2)*10^-3;      % Radius of outer conductor
c = 2.99792458e8;       % Speed of light in a vacuum in metres per second
lambda = c./f;          % Wavelength in air
%-----%

%---DETERMINE REFERENCE TO BE USED FROM USER INPUT-----%

if (strcmp(refdata, 'air') == 1|strcmp(refdata, 'Air') == 1|strcmp(refdata, 'Air2') == 1)
    er = 1.00064 % Dielectric constant of air.
    disp('Using air')
elseif (strcmp(refdata, 'teflon') == 1|strcmp(refdata, 'Teflon') == 1|strcmp(refdata,
'teflon2') == 1)
    er = 2.08 % Dielectric constant of teflon.
    disp('Using teflon')
elseif (strcmp(refdata, 'perspex') == 1|strcmp(refdata, 'Perspex') == 1|strcmp(refdata,
'perspex1') == 1|strcmp(refdata, 'perspex1_2') == 1)
    er = 2.6 % Dielectric constant of perspex.
    disp('Using perspex')
elseif (strcmp(refdata, 'water') == 1|strcmp(refdata, 'Water') == 1)
    er = 78.6 % Dielectric constant of perspex.
    disp('Using water')
end
%-----%

%---PARAMETERS TO BE USED FOR CALCULATING PERMITTIVITY--%

Co = tan(dphi./2)./(2*pi.*f.*z); % Probe capacitance
Cf = 0; % Capacitance inside probe dielectricum.
%-----%

%-----CALCULATE PERMITTIVITY-----%

k = Cf./Co; % Factor to be used in calculation of permittivity.
nume1 = (2*s11.*sin(-p11)); % Numerator of dielectric constant.
dene1 = (z*w.*Co);
dene12 = (1 + 2*s11.*cos(p11) + s11.^2);
den = dene1.*dene12; % Denominator of dielectric constant.
nume2 = (1 - s11.^2); % Numerator of loss factor.

```

```

e1 = (nume1./den) - k;                                %Calculate the dielectric constant
                                                        according to Stuchly and Stuchly.
e11 = (nume2)./(z*w.*Co).*(1 + 2*(s11.^2).*cos(p11) + s11.^2)); % Calculate the loss
factor according to Stuchly and Stuchly.
%-----%
%-----PLOT PERMITTIVITY-----%

% The following plots starts at 1 GHz

Df = (Stop - Start)/Points;
StartPoint = round((1e9 - Start)/Df);

E1avg = linspace(median(e1(StartPoint:length(f))), median(e1(StartPoint:length(f))),
length(f(StartPoint:length(f)))); % Calculate the median
E1 = E1avg(1)

figure(1)
subplot(2,1,1)    % Top figure
plot(f(StartPoint:length(f)), e1(StartPoint:length(f)), 'k', f(StartPoint:length(f)), E1avg, 'b')
% Plot the dielectric constant
title(['Dielectric constant of ', datafile, ' vs. Frequency']);
xlabel('Frequency [Hz]');
ylabel('Magnitude e"');
grid

legend('Black Measured Permittivity', 'Blue Median Permittivity', 0);

E11avg = linspace(median(e11(StartPoint:length(f))), median(e11(StartPoint:length(f))),
length(f(StartPoint:length(f)))); % Calculate the median
E11 = E11avg(1)

subplot(2,1,2)    % Bottom figure
plot(f(StartPoint:length(f)), e11(StartPoint:length(f)), 'k', f(StartPoint:length(f)), E11avg,
'b') % Plot the loss factor
title(['Loss factor of ', datafile, ' vs. Frequency']);
xlabel('Frequency [Hz]');
ylabel('Magnitude e"');
grid

figure(2)
plot(f, Co)
title(['Ceff vs. Frequency']);
xlabel('Frequency [Hz]');
ylabel('Ceff [F]');
grid on;
%-----THE END-----%

```

**WG Inversion Code**

```

%-----%
% W.J. Louw

% Program that calculates the permeability & permittivity
% of a sample material using either the S11 & S21 or S22 & S12
% parameters obtained from a S-Band Waveguide (WG) system & the
% Network Analyzer.

% Remember that Z0 should be set to 1 for all the standards and
% also the "Set Z0" parameter on the ANA should be set to 1.
%
% The code tests data for higher order mode propagation and the
% half-wavelength uncertainty area. It also determines a median value
% from 2.6 GHz upwards.
%-----%

%-----DEFINE FUNCTION & SETUP MATLAB-----%

function Extract_WG(datafile, d, PFC, direction) % User must input file with S-
parameter data

close all; % Close all graphs presently open
clc; % Clears Matlab command window
format long g; % Convenient format for displaying small numbers.
%-----%

%-----IMPORT S-PARAM & DEFINE CONSTANTS-----%

eval(datafile); % Loads file with S-Parameter data

if direction == 11
    disp('Nou vorentoe')
    SPar1 = eval(strcat(datafile,'_s11(:)')); %Loads the S11 parameter from "Data" file
    SPar2 = eval(strcat(datafile,'_s21(:)')); %Loads the S21 parameter from "Data" file
elseif direction == 22
    disp('Nou terug')
    SPar1 = eval(strcat(datafile,'_s22(:)')); %Loads the S11 parameter from "Data" file
    SPar2 = eval(strcat(datafile,'_s12(:)')); %Loads the S21 parameter from "Data" file
end

f = linspace(Start, Stop, length(SPar1)); % Define frequency range.

SPReal = real(SPar1);
SPImag = imag(SPar1);

```

```

%-----SMOOTHING OF MEASURED DATA-----%

SPar1_real_fit = polyfit(f,real(SPar1),PFC);
SPar1_real_val = polyval(SPar1_real_fit, f);
SPar1_imag_fit = polyfit(f,imag(SPar1),PFC);
SPar1_imag_val = polyval(SPar1_imag_fit, f);

SPar1_smooth = SPar1_real_val + i.*SPar1_imag_val;

SPar1new = SPar1_smooth(1:(length(SPar1_smooth)-1)); % Average between every 2
successive data points.

SPar2_real_fit = polyfit(f,real(SPar2),PFC);
SPar2_real_val = polyval(SPar2_real_fit, f);
SPar2_imag_fit = polyfit(f,imag(SPar2),PFC);
SPar2_imag_val = polyval(SPar2_imag_fit, f);

SPar2_smooth = SPar2_real_val + i.*SPar2_imag_val;

SPar2new = SPar2_smooth(1:(length(SPar2_smooth)-1));
%-----%

%-----DEFINE VARIABLES-----%

fnew = f(1:(length(f)-1));
ur = 1;
er = 1;
a = 72e-3;
c = 2.997924580e8; % Speed of light in vacuum
Lc = 144e-3; % Cut off wavelength of the WG for TE10 mode (2.082GHz)
L0 = c./f; % Wavelength in air at each frequency point
L0new = c./fnew; % Wavelength calculated using average frequency
Lgnew = (L0new./sqrt(ur*er-(L0new./Lc).^2));

Df = (Stop - Start)/Points; %Frequency steps
StartPoint = round((2.6e9 - Start)/Df) % To take median from 2.6GHz for any number of
points!
%-----%

%-----DETERMINE GROUP DELAY-----%

%Group delay = Negative rate of change of phase of SPar2 with respect to frequency.

mag = abs(SPar2_smooth); % Magnitude of SPar2

```



```
phase = unwrap(angle(SPar2_smooth)); % Angle of SPar2 in radians; Unwrap to avoid
jumps in phase
```

```
gradient = diff(-phase); % Difference in angle between every 2 successive f-points in
degrees.
```

```
df = diff(f); % Difference between each 2 successive frequency points
```

```
tg = (gradient./df)/(2*pi); % Group delay according to definition
```

```
%-----%
```

```
%-----CALCULATE GAMMA-----%
```

```
K = (SPar1new.^2 - SPar2new.^2 + 1)/(2.*SPar1new); % Determine K as defined.
```

```
tel = 1; % Define counter
```

```
while(tel <= length(SPar1new)) % Test if gamma <= 1
    %If not the negative sign of root should be used
    gammaB(tel) = K(tel) + sqrt(K(tel)^2 - 1); % Reflection coefficient
    if abs(gammaB(tel)) > 1 % Test if bigger than 1
        disp('Nou in if stelling')
        gammaB(tel) = K(tel) - sqrt(K(tel)^2 - 1); %Use the negative sign if gamma > 1
    end
    tel = tel + 1;
end
```

```
gamma = gammaB.'; % NB use .' to convert gamma to row format
%-----%
```

```
%-----PLOT GAMMA-----%
```

```
figure(1)
subplot(2,1,1)
plot(fnew, real(gamma))
title(['Real Part of Gamma ', datafile, ' vs. Frequency']);
xlabel('Frequency [Hz]');
ylabel('Real Gamma [Linear Scale]');
grid;
```

```
subplot(2,1,2)
plot(fnew, imag(gamma))
title(['Imag Part of Gamma ', datafile, ' vs. Frequency']);
xlabel('Frequency [Hz]');
ylabel('Imaginary Part of Gamma [Linear Scale]');
```

```

grid;

figure(2)
subplot(2,1,1)
plot(fnew, abs(gamma))
title(['Magnitude Gamma of ', datafile, ' vs. Frequency']);
xlabel('Frequency [Hz]');
ylabel('Magnitude Gamma [Linear Scale]');
grid;

subplot(2,1,2)
plot(fnew, angle(gamma).*(180/pi))
title(['Phase of Gamma ', datafile, ' vs. Frequency']);
xlabel('Frequency [Hz]');
ylabel('Angle of Gamma [Degrees]');
grid;
%-----%

%-----DETERMINE VALUE OF N-----%

% Calculate the value of N to be used as part of the ln of
% the complex propagation factor P.

P = (SPar1new + SPar2new - gamma)./(1 - (SPar1new + SPar2new).*gamma); %
Propagation factor
%Propagation factor (P) = exp(-gd); with g = alpha + jBeta = Propagation Constant

phi = log(1./P); % Natural log of complex Propagation Factor
phi2 = real(phi) + i*unwrap(imag(phi))

n2 = (fnew.*(tg) - unwrap(imag(phi))./(2*pi)); % n2 calculated from formula & rounded
to nearest integer.
%n2 = 0;

z = 1; % Counter z

while(z < Points)
    if n2(z) > 0
        n(z) = floor(n2(z));
    elseif n2(z) < 0
        n(z) = abs((ceil(n2(z))));
    else
        n(z) = 0;
    end;
    z = z + 1;
end

```

```

n = n'

while(z < Points)
    if n(z) > 0; disp('N groter as 0'); end; % Show message when n2 > 0
    if n(z) < 0; n(z) = 0; end;
    z = z + 1;
end

n = 0;
%-----%

%-----PLOT TRANSMISSION COEFFICIENT-----%

figure(3) % Plot real and imaginary
subplot(2,1,1)
plot(fnew, real(P))
title(['Real Transmission of ', datafile, ' vs. Frequency']);
xlabel('Frequency [Hz]');
ylabel('Real Part of Transmission [Linear Scale]');
grid;

subplot(2,1,2)
plot(fnew, imag(P))
title(['Angle Transmission of ', datafile, ' vs. Frequency']);
xlabel('Frequency [Hz]');
ylabel('Imaginary Part of Transmission');
grid;

figure(4) % Plot magnitude and Phase
subplot(2,1,1)
plot(fnew, abs(P))
title(['Magnitude Transmission of ', datafile, ' vs. Frequency']);
xlabel('Frequency [Hz]');
ylabel('Magnitude Transmission [Linear Scale]');
grid;

subplot(2,1,2)
plot(fnew, angle(P).*(180/pi))
title(['Phase Transmission of ', datafile, ' vs. Frequency']);
xlabel('Frequency [Hz]');
ylabel('Angle of Transmission [Degrees]');
grid;
%-----%

%-----CALCULATE PARAMETER WITH CORRECT N-----%

```

```

inv_lambda2 = -((((1/(2*pi*d)).*phi2 + (2.*pi.*n).*j)).^2); % Calculated from definition
inv_lambda = sqrt(inv_lambda2);
%-----%

%-----Calculate Permeability and Permittivity-----%

permeability = ((1 + gamma).*inv_lambda)./((1 - gamma).*sqrt((1./(L0new.^2)) -
(1/Lc^2)));

mag_factor = (inv_lambda2)./permeability;

permittivity = ((L0new.^2).*(inv_lambda2 + 1/(Lc^2)))./(permeability);

%-----Calculate Tan(d)-----%

%Tan(d) calculated according to W.B. Weir

delta1 = real(permeability).*real(permittivity) - (-imag(permeability).*-
imag(permittivity));
delta2 = real(permeability).*(- imag(permittivity)) + (-
imag(permeability).*real(permittivity));

tand = delta2./delta1; % Tan(d) according to W.B. Weir
%-----%

%-----Determine region of LambdaG/2-----%

Lc_10 = (144e-3).*sqrt(abs(real(permittivity)).*abs(real(permeability))));

Lgnew = (L0new./sqrt(abs(real(permittivity)).*abs(real(permeability)) -
(L0new./Lc_10).^2));

count = 1;
q = 1;
fedit = fnew(StartPoint);
t = StartPoint;

if d == 25e-3 % Test for LambdaG/2 in SH1
    while(count <= length(SPar1new))
        if isreal(Lgnew(count)) ~= 1 % If L0new > Lc_10 you have very small ur*er
values. This condition can't be true, i.e. ignore this value of Lgnew
            Lgnew(count) = 0;
        elseif ((Lgnew(count)) > 48e-3) && ((Lgnew(count)) < 52e-3)
            t(q) = count;
            fedit(q) = fnew(count); %Frequency point at which problem occurs.
        end
        count = count + 1;
        q = q + 1;
    end
end

```

```

        q = q + 1;
    end
    count = count + 1;
end
end

if d == 19.7e-3          % Test for LambdaG/2 in SH2
    while(count <= length(SPar1new))
        if isreal(Lgnew(count)) ~= 1 % If L0new > Lc_10 you have very small ur*er
            values. This condition can't be true, i.e. ignore this value of Lgnew
            Lgnew(count) = 0;
            elseif ((Lgnew(count)) > 38e-3) && ((Lgnew(count)) < 42e-3)
                t(q) = count;
                fedit(q) = fnew(count);
                q = q + 1;
            end
            count = count + 1;
        end
    end
end

fedit = fedit'
t = t'
%-----%

%---Determine if Higher Order Modes can Propagate in the Medium---%

fedit2 = fnew(1);
b = 1;
h = 1;
teller = 1;
while(teller <= length(fnew))
    fc_20(teller) = c/(a*sqrt(real(permeability(teller))*real(permittivity(teller))));
    if fc_20(teller) < fnew(teller)
        disp('Higher order mode can propogate')
        h(b) = teller;
        fedit2(b) = fnew(teller); %Frequency point at which problem occurs.
        b = b + 1;
    end
    teller = teller + 1;
end

fedit2 = fedit2'
h = h'

%-----Write Data Out to .txt file-----%
```

```

cl = fopen(strcat(datafile,'.txt'), 'w');

fprintf(cl, 'Permeability = \n');
fprintf(cl, 'Real\nPermeability');
fprintf(cl, '  Imag Permeability\n');
for (i=1:length(permeability))
    fprintf(cl, '%f', real(permeability(i,:)));
    fprintf(cl, '  %f\n', abs(imag(permeability(i,:))));
end

fprintf(cl, 'Permittivity = \n');
fprintf(cl, 'Dielectric\nConstant');
fprintf(cl, '  Loss Factor\n');
for (i=1:length(permittivity))
    fprintf(cl, '%f', real(permittivity(i,:)));
    fprintf(cl, '  %f\n', -imag(permittivity(i,:)));
end

fclose(cl);
%-----%

%-----Graph of permittivity vs. frequency-----%

% Calculate the median
DCnew = linspace(median(real(permittivity(StartPoint:length(fnew)))),
median(real(permittivity(StartPoint:length(fnew)))), length(StartPoint:length(fnew)));
DCnew1 = DCnew(1) % Display the median value.

% Plot the real & imaginary parts of permittivity and permeability on one page.
figure(5)
subplot(2,2,1)
plot(fnew(StartPoint:length(fnew)), DCnew, 'b', fnew(StartPoint:length(fnew)),
real(permittivity(StartPoint:length(fnew))), 'k', fedit, real(permittivity(t)), 'r*', fedit2,
real(permittivity(h)), 'go'); % Plot the median & real data of the Dielectric Constant.
title(['Dielectric Constant of ', datafile, ' vs. Frequency']);
xlabel('Frequency [Hz]');
ylabel('Magnitude e"');
grid;

legend('Blue Median', 'Black Permittivity', 'Red Half Wavelength', 'Higher Order Modes',
0)

LFnew = linspace(median(imag(permittivity(StartPoint:length(fnew)))),
median(imag(permittivity(StartPoint:length(fnew)))), length(StartPoint:length(fnew))); %
Calculate the median

```

% of the Loss Factor and creates a vector of its value.

LFnew = -LFnew(1) % Display the median value.

subplot(2,2,3)

plot(fnew(StartPoint:length(fnew)), LFnew, 'b', fnew(StartPoint:length(fnew)), -  
imag(permittivity(StartPoint:length(fnew))), 'k', fedit, -imag(permittivity(t)), 'r\*', fedit2, -  
imag(permittivity(h)), 'go'); % Plot the median & real data of the Loss Factor.

title(['Loss Factor of ', datafile, ' vs. Frequency']);

xlabel('Frequency [Hz]');

ylabel('Magnitude e''');

grid;

Magnet\_Real = linspace(median(real(permeability(StartPoint:length(fnew)))),  
median(real(permeability(StartPoint:length(fnew)))), length(StartPoint:length(fnew))); %  
Calculate the median

Magnet\_Real = Magnet\_Real(1) % Display the median value.

subplot(2,2,2)

plot(fnew(StartPoint:length(fnew)), real(permeability(StartPoint:length(fnew))), 'k',  
fnew(StartPoint:length(fnew)), Magnet\_Real, '-b', fedit2, real(permeability(h)), 'go', fedit,  
real(permeability(t)), 'r\*'); % Plots the real part

title(['Real part of permeability of ', datafile, ' vs. Frequency']);

xlabel('Frequency [Hz]');

ylabel('Magnitude u''');

grid;

Magnet\_Imag = linspace(median(imag(permeability(StartPoint:length(fnew)))),  
median(imag(permeability(StartPoint:length(fnew)))), length(StartPoint:length(fnew)));

% Calculate the median

Magnet\_Imag = -Magnet\_Imag(1) % Display the median value.

subplot(2,2,4)

plot(fnew(StartPoint:length(fnew)), Magnet\_Imag, 'b', fnew(StartPoint:length(fnew)), -  
imag(permeability(StartPoint:length(fnew))), 'k', fedit, -imag(permeability(t)), 'r\*', fedit2,  
-imag(permeability(h)), 'go'); % Plots the imaginary part.

title(['Imaginary part of permeability of ', datafile, ' vs. Frequency']);

xlabel('Frequency [Hz]');

ylabel('Magnitude u''');

grid;

%-----%

%-----Graph of tan(delta) vs. frequency-----%

```
figure(6)
plot(fnew, tand);
title(['Tan(delta) of ', datafile, ' vs. Frequency']);
xlabel('Frequency [Hz]');
ylabel('Magnitude tan(delta)');
grid;
%-----THE END-----%
```



**Experiment/Simulation Comparison**

```

%-----%
% W.J. Louw

% This program plot experimental and simulation results on the same axes
% for results comparison. The peak and average percentage errors are calculated
% at the end of the code.

%-----%
%-----SETUP MATLAB-----%

function Plot_Exp_Sim_fshift(exp1, exp2, exp3, exp4, sim, fshift)

close all;
format long g;

eval(sim);
eval(exp1);
eval(exp2);
eval(exp3);
eval(exp4);
%-----%
%-----LOAD SIMULATION DATA-----%

var_mag11 = eval(strcat(sim,'_mag11')); % S11 parameter of known material loaded
from file.
var_ang11 = eval(strcat(sim,'_ang11')); % S11 parameter of known material loaded from
file.
var_mag21 = eval(strcat(sim,'_mag21')); % S11 parameter of known material loaded
from file.
var_ang21 = eval(strcat(sim,'_ang21')); % S11 parameter of known material loaded from
file.

mag11 = var_mag11(:,2);
ang11 = var_ang11(:,2);
mag21 = var_mag21(:,2);
ang21 = var_ang21(:,2);

LogMagSim11 = 20*log10(mag11);
LogMagSim21 = 20*log10(mag21);

fsim = var_mag11(:,1).*10^9;
%-----LOAD EXPERIMENTAL DATA-----%

%-----Eksp. 1-----%

```

```
temp11_exp1 = eval(strcat(exp1,'_s11(:)')); % S11 parameter of sample material loaded
from file.
```

```
s11_exp1 = 20*log10(abs(temp11_exp1));          % Magnitude of S11 of unknown
material
```

```
exp1_ang_s11 = angle(temp11_exp1).*(180/pi);
```

```
temp21_exp1 = eval(strcat(exp1,'_s21(:)')); % S11 parameter of sample material loaded
from file.
```

```
s21_exp1 = 20*log10(abs(temp21_exp1));          % Magnitude of S11 of unknown
material
```

```
exp1_ang_s21 = angle(temp21_exp1).*(180/pi);
```

```
%-----%
```

```
%-----Eksp. 2-----%
```

```
temp11_exp2 = eval(strcat(exp2,'_s11(:)')); % S11 parameter of sample material loaded
from file.
```

```
s11_exp2 = 20*log10(abs(temp11_exp2));          % Magnitude of S11 of unknown
material
```

```
exp2_ang_s11 = angle(temp11_exp2).*(180/pi);
```

```
temp21_exp2 = eval(strcat(exp2,'_s21(:)')); % S11 parameter of sample material loaded
from file.
```

```
s21_exp2 = 20*log10(abs(temp21_exp2));          % Magnitude of S11 of unknown
material
```

```
exp2_ang_s21 = angle(temp21_exp2).*(180/pi);
```

```
%-----%
```

```
%-----Eksp. 3-----%
```

```
temp11_exp3 = eval(strcat(exp3,'_s11(:)')); % S11 parameter of sample material loaded
from file.
```

```
s11_exp3 = 20*log10(abs(temp11_exp3));          % Magnitude of S11 of unknown
material
```

```
exp3_ang_s11 = angle(temp11_exp3).*(180/pi);
```

```
temp21_exp3 = eval(strcat(exp3,'_s21(:)')); % S11 parameter of sample material loaded
from file.
```

```
s21_exp3 = 20*log10(abs(temp21_exp3));          % Magnitude of S11 of unknown
material
```

```

exp3_ang_s21 = angle(temp21_exp3).*(180/pi);

%-----%

%-----Eksp. 4-----%

temp11_exp4 = eval(strcat(exp4,'_s11(:)')); % S11 parameter of sample material loaded
from file.
s11_exp4 = 20*log10(abs(temp11_exp4));          % Magnitude of S11 of unknown
material
exp4_ang_s11 = angle(temp11_exp4).*(180/pi);

temp21_exp4 = eval(strcat(exp4,'_s21(:)')); % S11 parameter of sample material loaded
from file.
s21_exp4 = 20*log10(abs(temp21_exp4));          % Magnitude of S11 of unknown
material
exp4_ang_s21 = angle(temp21_exp4).*(180/pi);

%-----%

%-----%

%DETERMINE UPPER AND LOWER BOUNDARIES OF EXPERIMENTAL DATA

%-----S11 Magnitude-----%

mat11_mag = zeros(Points,4);
mat11_mag(:,1) = s11_exp1;
mat11_mag(:,2) = s11_exp2;
mat11_mag(:,3) = s11_exp3;
mat11_mag(:,4) = s11_exp4;
mattrans11_mag = mat11_mag';
maxs11_mag = max(mattrans11_mag); % upper and lower bounds on experimental data
mins11_mag = min(mattrans11_mag);

%-----S11 Angle-----%

mat11_ang = zeros(Points,4);
mat11_ang(:,1) = exp1_ang_s11;
mat11_ang(:,2) = exp2_ang_s11;
mat11_ang(:,3) = exp3_ang_s11;
mat11_ang(:,4) = exp4_ang_s11;
mattrans11_ang = mat11_ang';
maxs11_ang = max(mattrans11_ang); % upper and lower bounds on experimental data

```

```

mins11_ang = min(mattrans11_ang);

%-----S21 Magnitude-----%

mat21_mag = zeros(Points,4);
mat21_mag(:,1) = s21_exp1;
mat21_mag(:,2) = s21_exp2;
mat21_mag(:,3) = s21_exp3;
mat21_mag(:,4) = s21_exp4;
mattrans21_mag = mat21_mag';
maxs21_mag = max(mattrans21_mag); % upper and lower bounds on experimental data
mins21_mag = min(mattrans21_mag);

%-----S21 Angle-----%

mat21_ang = zeros(Points,4);
mat21_ang(:,1) = exp1_ang_s21;
mat21_ang(:,2) = exp2_ang_s21;
mat21_ang(:,3) = exp3_ang_s21;
mat21_ang(:,4) = exp4_ang_s21;
mattrans21_ang = mat21_ang';
maxs21_ang = max(mattrans21_ang); % upper and lower bounds on experimental data
mins21_ang = min(mattrans21_ang);

%-----%

%-----%

fexp = linspace(Start, Stop, Points)' + fshift; %

%-----Grafieke-----%

figure(1)
subplot(2,2,1)
plot(fsim, LogMagSim11, '-k', fexp(1:(length(fexp)-1)), maxs11_mag(1:(length(fexp)-1)), '--r', fexp(1:(length(fexp)-1)), mins11_mag(1:(length(fexp)-1)), '--b');
title(['S11 Mag Bounds of', ' ', exp1, ' and ', sim, ' vs. Frequency']);
xlabel('Frequency [Hz]');
ylabel('Log Magnitude [dB]');
grid;

legend('Black Simulation', ['-- Red Experimental Upper Bound Shifted ', num2str(fshift, '%5.5g'), ' Hz'], ['-- Blue Experimental Lower Bound Shifted ', num2str(fshift, '%5.5g'), ' Hz'], 0);

```

```

subplot(2,2,3)
plot(fsim, ang11, '-k', fexp(1:(length(fexp)-1)), maxs11_ang(1:(length(fexp)-1)), '--r',
fexp(1:(length(fexp)-1)), mins11_ang(1:(length(fexp)-1)), '--b');
title(['S11 Phase Bounds of', ' ', exp1, ' and ', sim, ' vs. Frequency']);
xlabel('Frequency [Hz]');
ylabel('Phase Angle [Degrees]');
grid;

```

```

subplot(2,2,2)
plot(fsim, LogMagSim21, '-k', fexp(1:(length(fexp)-1)), maxs21_mag(1:(length(fexp)-1)), '--r',
fexp(1:(length(fexp)-1)), mins21_mag(1:(length(fexp)-1)), '--b');
title(['S21 Mag Bounds of', ' ', exp1, ' and ', sim, ' vs. Frequency']);
xlabel('Frequency [Hz]');
ylabel('Log Magnitude [dB]');
grid;

```

```

subplot(2,2,4)
plot(fsim, ang21, '-k', fexp(1:(length(fexp)-1)), maxs21_ang(1:(length(fexp)-1)), '--r',
fexp(1:(length(fexp)-1)), mins21_ang(1:(length(fexp)-1)), '--b');
title(['S21 Phase Bounds of', ' ', exp1, ' and ', sim, ' vs. Frequency']);
xlabel('Frequency [Hz]');
ylabel('Phase Angle [Degrees]');
grid;

```

```
%-----Percentage Average and Peak Error-----%
```

```
%-----S11 Magnitude-----%
```

```
% Interpolate the simulation results to set exp. and sim vectors
% to the same points.
```

```
Sim_S11_Interp_Mag = interp1(fsim, LogMagSim11, fexp, 'spline');
```

```
% Test if sim data is within, lower or higher than bounds. Determine
% difference in comparison and setup a new S-parameter with which to
% compare the difference in comparison.
```

```
z = 1;
```

```

while (z <= Points)
    if (mins11_mag(z) < Sim_S11_Interp_Mag(z) && Sim_S11_Interp_Mag(z) <
maxs11_mag(z))
        delta_S11_mag(z) = 0;
        new_s11_mag(z) = mins11_mag(z);

```

```

elseif Sim_S11_Interp_Mag(z) > maxs11_mag(z)
    delta_S11_mag(z) = abs(abs(Sim_S11_Interp_Mag(z)) - abs(maxs11_mag(z)));
    new_s11_mag(z) = maxs11_mag(z);
elseif Sim_S11_Interp_Mag(z) < mins11_mag(z)
    delta_S11_mag(z) = abs(abs(Sim_S11_Interp_Mag(z)) - abs(mins11_mag(z)));
    new_s11_mag(z) = mins11_mag(z);
else
    delta_S11_mag(z) = 0;
    new_s11_mag(z) = mins11_mag(z);
end
    z = z + 1;
end

```

```

Avg_11Mag_M = mean(delta_S11_mag./(abs(new_s11_mag)).*100)

```

```

zet=1;

```

```

% Determine peak error

```

```

n = 0;

```

```

while(zet <= Points)
    if delta_S11_mag(zet) == max(delta_S11_mag)
        n = zet
    end
    zet = zet + 1;
end

```

```

Peak_11Mag = (max(delta_S11_mag)/abs(new_s11_mag(n)))*100

```

```

%-----S11 Phase-----%

```

```

% Interpolate the simulation results to set exp. and sim vectors
% to the same points.

```

```

Sim_S11_Interp_Phase = interp1(fsim, ang11, fexp, 'spline');

```

```

% Test if sim data is within, lower or higher than bounds. Determine
% difference in comparison and setup a new S-parameter with which to
% compare the difference in comparison.

```

```

z = 1;

```

```

while (z <= Points)

```

```

    if (mins11_ang(z) < Sim_S11_Interp_Phase(z) && Sim_S11_Interp_Phase(z) <
maxs11_ang(z))
        delta_S11_phase(z) = 0;
        new_s11_phase(z) = mins11_ang(z);
    elseif Sim_S11_Interp_Phase(z) > maxs11_ang(z)
        delta_S11_phase(z) = abs(abs(unwrap(Sim_S11_Interp_Phase(z))) -
abs(unwrap(maxs11_ang(z))));
        new_s11_phase(z) = maxs11_ang(z);
    elseif Sim_S11_Interp_Phase(z) < mins11_ang(z)
        delta_S11_phase(z) = abs(abs(unwrap(Sim_S11_Interp_Phase(z))) -
abs(unwrap(mins11_ang(z))));
        new_s11_phase(z) = mins11_ang(z);
    else
        delta_S11_phase(z) = 0;
        new_s11_phase(z) = mins11_ang(z);
    end
    z = z + 1;
end

```

```
delta_S11_phase;
```

```
new_s11_phase;
```

```

Avg_11Phase_M =
mean(unwrap(delta_S11_phase)./(abs(unwrap(new_s11_phase)))*100)

```

```
zet = 1;
```

```
% Determine peak error
```

```
n = 0;
```

```

while(zet <= Points)
    if delta_S11_phase(zet) == max(delta_S11_phase)
        n = zet;
    end
    zet = zet + 1;
end

```

```
Peak_11Phase = (max(delta_S11_phase)/abs(unwrap(new_s11_phase(n))))*100
```

```
%-----S21 Magnitude-----%
```

```

% Interpolate the simulation results to set exp. and sim vectors
% to the same points.

```

```
Sim_S21_Interp_Mag = interp1(fsim, LogMagSim21, fexp, 'spline');
```

```

% Test if sim data is within, lower or higher than bounds. Determine
% difference in comparison and setup a new S-parameter with which to
% compare the difference in comparison.

z = 1;

while (z <= Points)
    if (mins21_mag(z) < Sim_S21_Interp_Mag(z) && Sim_S21_Interp_Mag(z) <
maxs21_mag(z))
        delta_S21_mag(z) = 0;
        new_s21_mag(z) = mins21_mag(z);
    elseif Sim_S21_Interp_Mag(z) > maxs21_mag(z)
        delta_S21_mag(z) = abs(abs(Sim_S21_Interp_Mag(z)) - abs(maxs21_mag(z)));
        new_s21_mag(z) = maxs21_mag(z);
    elseif Sim_S21_Interp_Mag(z) < mins21_mag(z)
        delta_S21_mag(z) = abs(abs(Sim_S21_Interp_Mag(z)) - abs(mins21_mag(z)));
        new_s21_mag(z) = mins21_mag(z);
    else
        delta_S21_mag(z) = 0;
        new_s21_mag(z) = mins21_mag(z);
    end
    z = z + 1;
end

Avg_21Mag_M = mean(delta_S21_mag./(abs(new_s21_mag)).*100)

zet=1;

% Determine peak error

n = 0;

while(zet <= Points)
    if delta_S21_mag(zet) == max(delta_S21_mag)
        n = zet
    end
    zet = zet + 1;
end

Peak_21Mag = (max(delta_S21_mag)/abs(new_s21_mag(n)))*100

%-----S21 Phase-----%

% Interpolate the simulation results to set exp. and sim vectors
% to the same points.

```



```
Sim_S21_Interp_Phase = interp1(fsim, ang21, fexp, 'spline');
```

```
% Test if sim data is within, lower or higher than bounds. Determine
% difference in comparison and setup a new S-parameter with which to
% compare the difference in comparison.
```

```
z = 1;
```

```
while (z <= Points)
```

```
    if (mins21_ang(z) < Sim_S21_Interp_Phase(z) && Sim_S21_Interp_Phase(z) <
maxs21_ang(z))
```

```
        delta_S21_phase(z) = 0;
```

```
        new_s21_phase(z) = mins21_ang(z);
```

```
    elseif Sim_S21_Interp_Phase(z) > maxs21_ang(z)
```

```
        delta_S21_phase(z) = abs(abs(unwrap(Sim_S21_Interp_Phase(z))) -
abs(unwrap(maxs21_ang(z))));
```

```
        new_s21_phase(z) = maxs21_ang(z);
```

```
    elseif Sim_S21_Interp_Phase(z) < mins21_ang(z)
```

```
        delta_S21_phase(z) = abs(abs(unwrap(Sim_S21_Interp_Phase(z))) -
abs(unwrap(mins21_ang(z))));
```

```
        new_s21_phase(z) = mins21_ang(z);
```

```
    else
```

```
        delta_S21_phase(z) = 0;
```

```
        new_s21_phase(z) = mins21_ang(z);
```

```
    end
```

```
    z = z + 1;
```

```
end
```

```
delta_S21_phase;
```

```
new_s21_phase;
```

```
Avg_21Phase_M =
```

```
mean(unwrap(delta_S21_phase)./(abs(unwrap(new_s21_phase))).*100)
```

```
zet = 1;
```

```
% Determine peak error
```

```
n = 0;
```

```
while(zet <= Points)
```

```
    if delta_S21_phase(zet) == max(delta_S21_phase)
```

```
        n = zet
```

```
    end
```

```
    zet = zet + 1;
```

```
end
```

```
Peak_21Phase = (max(delta_S21_phase)/abs(unwrap(new_s21_phase(n))))*100
```

```
%-----THE END-----%
```